ELECTROMAGNETIC MODELING AND MEASUREMENT OF ADAPTIVE METAMATERIAL STRUCTURAL ELEMENTS

THESIS

Matthew E. Jussaume, Captain, USAF
AFIT/GE/ENG/11-20

DEPARTMENT OF THE AIR FORCE
AIR UNIVERSITY

AIR FORCE INSTITUTE OF TECHNOLOGY

Wright-Patterson Air Force Base, Ohio

AFIT/GE/ENG/11-20

ELECTROMAGNETIC MODELING AND MEASUREMENT OF ADAPTIVE METAMATERIAL STRUCTURAL ELEMENTS

THESIS

Presented to the Faculty
Department of Electrical and Computer Engineering
Graduate School of Engineering and Management
Air Force Institute of Technology
Air University
Air Education and Training Command
in Partial Fulfillment of the Requirements for the
Degree of Master of Science in Electrical Engineering

Matthew E. Jussaume, B.S.E.E.
Captain, USAF

March 2011

AFIT/GE/ENG/11-20

ELECTROMAGNETIC MODELING AND MEASUREMENT OF ADAPTIVE METAMATERIAL STRUCTURAL ELEMENTS

Matthew E. Jussaume, B.S.E.E.
Captain, USAF

Approved:

Dr. Peter J. Collins (Chairman)

24 FEB 2011
Date

Ronald A. Coutu
Dr. Ronald A. Coutu, Jr. (Member)

24 Feb 11
Date

Michael Havrilla
Dr. Michael J. Havrilla (Member)

24 Feb 2011
Date

AFIT/GE/ENG/11-20

Abstract

Metamaterials are devices with embedded structures that provide the device with unique properties. Several applications for metamaterials have been proposed including electromagnetic cloaks, lenses with improved resolution over traditional lenses, and improved antennas.

There are two obstacles to practical metamaterial development that this thesis addresses. The first is uncertainty in the characterization of electromagnetic field behavior in the presence of metamaterial structures. The uncertainty lies in the current methods of describing the unique properties of metamaterials. To address this obstacle, a method of prediction aided measurement is developed and exploited to examine the field interactions within metamaterial devices. The fusion of simulation and measurement techniques enhances the understanding of the physical interactions of fields in the presence of metamaterials. Guided-wave measurements of the metamaterial samples performed using a stripline waveguide are the chosen measurement technique because the stripline generates the same TEM excitation as a plane wave at normal incidence which is typical of the anticipated applications. The electromagnetic fields within equivalent models are examined using CST Microwave Studio®, revealing the field behavior inside and outside resonance regions.

The second obstacle to practical metamaterial development that this thesis addresses is the small bandwidth of current metamaterial devices. This thesis characterizes the effectiveness of several metamaterial designs. The basic design incorporates a microelectromechanical systems (MEMS) variable capacitor into a double negative (DNG) metamaterial structure. One set of devices is fabricated with the MEMS capacitor in the gap of the split ring resonator (SRR) of the DNG metamaterial.

Applying voltage to the MEMS device changes the effective capacitance, thereby adjusting the resonant frequency of the device. Stripline measurements of devices show a maximum shift of 1.62 GHz or an 11.34% difference from the original resonance frequency. Simulation results of the devices are compared to the measured results to validate the modeling process. They are found to be in agreement.

Additionally, a similar device with a larger unit cell and four possible capacitor layouts is examined with stripline measurements and computer models. Recommendations for design improvements are provided. The initial capacitor layout with MEMS capacitors in the split ring gaps is recommended for future design iterations with adjusted gap capacitance values.

Acknowledgements

I would not have been able to accomplish this venture without the help of many people. In particular, I would not have travelled this far without my wife, who loved and supported me through this time and graciously agreed to proofread this document several times. Also, I must thank my daughter for reminding me to come home every night in time to tuck her in.

I also received help from many people at AFIT and beyond. I would like to give thanks to my thesis committee: Dr. Havrilla for his intense instruction on electromagnetics and materials; Dr. Coutu for his insight into MEMS devices; and Dr. Collins for his support, guidance, discussions and teachings. I would like to especially thank the RF metamaterials research team for their fabrication skills, measurement help, and encouragement. I would also like to thank the technical support group at Sonnet Software for their help with CST Microwave Studio®. Finally, I would like to thank my classmates for their support, insight, and humor as we travelled down the same arduous road.

Matthew E. Jussaume

Table of Contents

List of Figures

List of Tables

List of Symbols

Symbol		Page
$\boldsymbol{E}$	electric field vector	8
$\boldsymbol{H}$	magnetic field vector	8
$\boldsymbol{D}$	electric flux density	8
$\boldsymbol{B}$	magnetic flux density	8
c	speed of light in free space	8
ϵ	electric permittivity of a medium	8
μ	magnetic permeability of a medium	8
j	imaginary unit ($j = \sqrt{-1}$)	8
ω	angular frequency	8
$\boldsymbol{k}$	wave vector	8
$\boldsymbol{S}$	Poynting vector	9
$\hat{n}$	surface normal unit vector	10
n	index of refraction	10
p	parameter indicating handedness of a material	11
ϵ_0	permittivity of free space	11
μ_0	permeability of free space	11
φ_t	angle of transmission through a material	11
φ_i	angle of incidence on a material	11
a	separation length between wires	12

Symbol		Page
r_w	wire radius	12
ω_p	plasmon angular frequency	12
σ	electric conductivity	12
λ	wavelength	13
r_{SRR}	inner split ring resonator radius	13
w	split ring resonator trace width	13
d	gap between a split ring resonator pair	13
ℓ	separation length between split ring resonator layers	13
R_1	split ring resonator resistance of a unit length for metal sheets	13
ω_0	angular resonant frequency	14
d_m	distance traveled by an wave in a medium	17
k_0	freespace wavenumber	17
$\hat{r}_\pm$	unit vector in direction of radiation from an infinite array	18
s_x	incident plane wave propagation vector x-component	18
s_z	incident plane wave propagation vector z-component	18
m_1	Floquet mode for x-direction	18
m_2	Floquet mode for z-direction	18
D_x	interelement spacing in x-direction	18
D_z	interelement spacing in z-direction	18
G	primary grid for finite integration technique	19
$\tilde{G}$	dual grid for finite integration technique	19

Symbol		Page
$\boldsymbol{e}$	grid electric voltage vector	20
$\boldsymbol{h}$	grid magnetic voltage vector	20
$\boldsymbol{b}$	grid magnetic induction flux	20
$\boldsymbol{j}$	electric charge current	20
$\boldsymbol{d}$	grid electric displacement flux	20
q_{ev}	electric charge density	20
L_i	facet length of the ith cell in G	20
$\tilde{L}_i$	facet length of the ith cell in $\tilde{G}$	20
A_i	facet area of the ith cell in G	20
$\tilde{A}_i$	facet area of the ith cell in $\tilde{G}$	20
$\boldsymbol{J}$	electric current vector	20
$\boldsymbol{C}$	support matrix operator $\oint_{\partial A} \cdot d\boldsymbol{s}$ for G	21
$\boldsymbol{S}$	support matrix operator $\oint_{\partial V} \cdot d\boldsymbol{A}$ for G	21
$\tilde{\boldsymbol{C}}$	support matrix operator $\oint_{\partial \tilde{A}} \cdot d\boldsymbol{s}$ for $\tilde{G}$	21
$\tilde{\boldsymbol{S}}$	support matrix operator $\oint_{\partial \tilde{V}} \cdot d\boldsymbol{A}$ for $\tilde{G}$	21
$\boldsymbol{M}_{\boldsymbol{\epsilon}}$	spatial discretization of ϵ matrix	22
$\boldsymbol{M}_{\boldsymbol{\mu}}$	spatial discretization of μ matrix	22
$\boldsymbol{M}_{\boldsymbol{\sigma}}$	spatial discretization of σ matrix	22
$\boldsymbol{j}_{\boldsymbol{s}}$	grid source electric current	22
d_s	material slab thickness	25
m	branch integer	26
f	frequency	34

Symbol		Page
d_b	distance of beam shift from centerline	37
L	inductance	43
C	capacitance	43
h	split ring resonator thickness	43
l	split ring resonator length	43
δ	split ring resonator gap width	43
μ_r	relative permeability	45
q	volume fraction of frequency dependent magnetic material	45
ϵ_r	relative permittivity	51
ϵ_∞	relative permittivity high-frequency limit	52
ω_p	plasma angular frequency	52
γ	damping constant	52
C_s	capacitance of the switch	52
R_s	resistance of the switch	52
S_{11}	simulated reflection	61
S_{21}	simulated transmission	62
C_1	cantilever capacitance with air gap	62
C_2	cantilever capacitance with dielectric	62
d_1	distance from top of dielectric to bottom of cantilever	62
d_2	thickness of dielectric	62
ϵ_r	permittivity of cantilever dielectric	62
A	area of cantilever capacitor	62

Symbol		Page
V_1^-	impulse voltage response received at port 1	120
V_2^-	impulse voltage response received at port 2	120
V_1^+	impulse voltage response transmitted at port 1	120
S_{11}^{sam}	reflection of the sample	121
S_{21}^{sam}	transmission of the sample	121
S_{11}^{nwa}	reflection received by the network analyzer	121
S_{21}^{nwa}	transmission received by the nework analyzer	121
d_s	length of material sample	121
Z_o	reference impedance	155
Z_{Total}	total impedance	155
C_{Total}	total capacitance	155

List of Abbreviations

Abbreviation		Page
DNG	double negative	1
SRR	split ring resonator	1
PAM	prediction aided measurement	2
AFIT	Air Force Institute of Technology	3
FSS	frequency selective surface	4
MEMS	microelectromechanical systems	4
LHM	left-handed material	9
RHM	right-handed material	9
MWS®	Microwave Studio®	19
FIT	finite integration technique	19
FDTD	finite difference time-domain	19
PEC	perfect electric conductor	24
PMC	perfect magnetic conductor	24
PML	perfectly matched layer	24
FEM	finite element method	28
RCS	radar cross section	38
TLM	Transmission Line Matrix Method	55
LOREnet	low observable radar and electromagnetics network	59
RF	radio frequency	113

Abbreviation		Page
BANTAM	broadband antenna near-field test and measurement	113
GTRI	Georgia Tech Research Institute	113
NWA	network analyzer	119
SOLT	short open load through	155

ELECTROMAGNETIC MODELING AND MEASUREMENT OF ADAPTIVE
METAMATERIAL STRUCTURAL ELEMENTS

I. Introduction

1.1 Problem Description

Metamaterial devices have received much attention over the past two decades. There are many definitions for metamaterials. For this research effort, a metamaterial is defined as "an arrangement of artificial structural elements designed to achieve advantageous and unusual properties" [20]. In spite of the attention garnered by metamaterials, the science behind their apparent unusual properties is not settled.

According to some researchers, metamaterials can be viewed to have a set of macro effective parameters for the medium, much as a molecular lattice interacts with incident electromagnetic fields. These effective constituent parameters produce quantities such as the effective index of refraction and effective impedance. These quantities dictate the behavior of the electromagnetic fields inside a metamaterial and are what gives a metamaterial its unusual properties.

The effective permittivity and permeability are controlled by the geometry of the structural building blocks, the unit cells. When both the permittivity and permeability are negative, the material is referred to as a double negative (DNG) material and takes on a negative index of refraction [7]. Commonly, DNG materials are constructed with wire lattices and a pair of split ring resonator (SRR) particles. An example is shown in Figure 1. Other unit cell structures are possible and are discussed in Chapter II, however the unit cell shown in Figure 1 is the basis for the structures analyzed in this thesis.

Still, other researchers contend that it is impossible for a material to achieve a negative index of refraction. Their arguments are based on causality and the physical meaning behind a negative index of refraction. The theories behind these two dissenting opinions are discussed in Chapter II.

Despite the disagreement on the physics of the phenomena, both groups of researchers can agree that the dispersive region of interest is small. Unfortunately, this narrow bandwidth limits the utility of metamaterials in certain applications. In the interest of practicality, expansion of the resonance bandwidth would be very useful.

In general, directly measuring electromagnetic fields without the measurement setup disturbing the experiment is a difficult task. Specifically with metamaterials, slightly disturbing the fields around the highly resonant devices can change near-field measurements drastically. To overcome this challenge, a prediction aided measurement (PAM) technique is developed and exploited to examine the field interactions within adaptive metamaterial devices. For this technique, models of physical devices are created with far field results reasonably matching measured data. The simulated

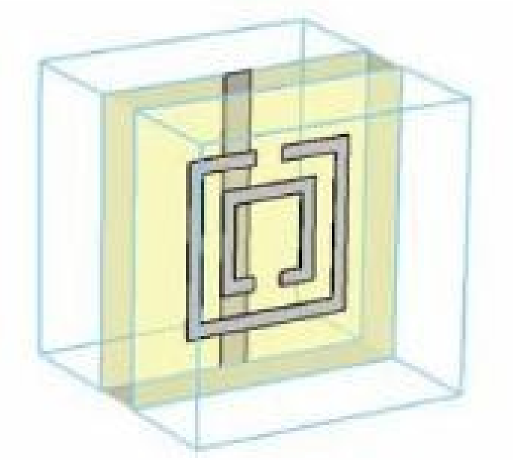

Figure 1. A typical unit cell for a DNG metamaterial structure consists of a concentric SRR pair and wire lattice [16].

field interactions within these models are assumed to reasonably match the field interactions within the measured devices. This assumption does not account for different structures that would create the same far field results, limiting current analysis only to structures designed and manufactured at the Air Force Institute of Technology (AFIT).

1.2 Potential Metamaterial Applications

The ability to steer electromagnetic fields in a medium consisting of conventional materials is restricted by the fact that the electric permittivity and magnetic permeability are positive. While discussed in theory by Veselago in 1968, the idea of materials with negative constituent parameters did not receive much interest until an increase of research into metamaterials took place [46]. Transformation optics uses smooth transitions of the constituent parameters of the guiding media to guide electromagnetic fields in place of traditional guiding structures such as waveguides or fiber optics. Using negative refraction, effective media can theoretically be created to steer electromagnetic fields. Ward and Pendry show that Maxwell's equations are invariant under any type of coordinate transformation with only the permittivity and permeability changing values [48]. A metamaterial's constitutive parameters are defined by the unit cell geometry, allowing the constitutive parameter tensors to be designed to guide electromagnetic waves along a desired path [21].

Based on the promise provided by transformation optics, a 2009 *Popular Mechanics* article listed several common place applications for metamaterials: cellphones with smaller antennas, detectors capable of detecting single molecules for use in finding weapons of mass destruction, microscope lenses capable of focusing beyond the diffraction limit, and fast metamaterial switching devices for photonic equipment [11]. Metamaterials have also been proposed as cloaking devices in [14], [21] and [31].

1.3 Research Goals

The goals of this research fall into two areas: characterization of field behavior in the presence of metamaterial structures and the analysis of adaptive metamaterial structures.

The first objective is to examine field behavior in the presence of metamaterial structures. Included in the characterization of the field behavior are advanced computational electromagnetic models. These models utilize frequency- and time-domain techniques to generate theoretical predictions of the field behavior in metamaterial structures. These models are based solely on Maxwell's equations and are not attached to the two differing theories on metamaterial characterization: effective medium theory or frequency selective surface (FSS) theory. The simulation techniques are described in detail in Section 2.3.

The electric and magnetic fields cannot be easily measured in the near-field without disturbing the fields. Therefore, measurements can only provide far field information about the field interactions in the presence of metamaterials. Computational models are therefore used in concert with measurements to analyze and characterize the field behavior in the presence of metamaterials. Guided-wave measurements of the metamaterial samples performed using a stripline waveguide are the chosen measurement technique because the stripline generates the same TEM excitation as a plane wave at normal incidence which is more typical of the anticipated applications. The stripline measurements also utilize equipment already owned by AFIT.

A novel metamaterial structure that achieves frequency adaptability was proposed in a previous AFIT research effort [34],[19]. The structure is based on a basic DNG unit cell. The proposed structure also incorporates a microelectromechanical systems (MEMS) variable capacitor across the gaps of the SRR particles. Figure 2 shows the proposed design. Varying the capacitance of the SRR particles has been

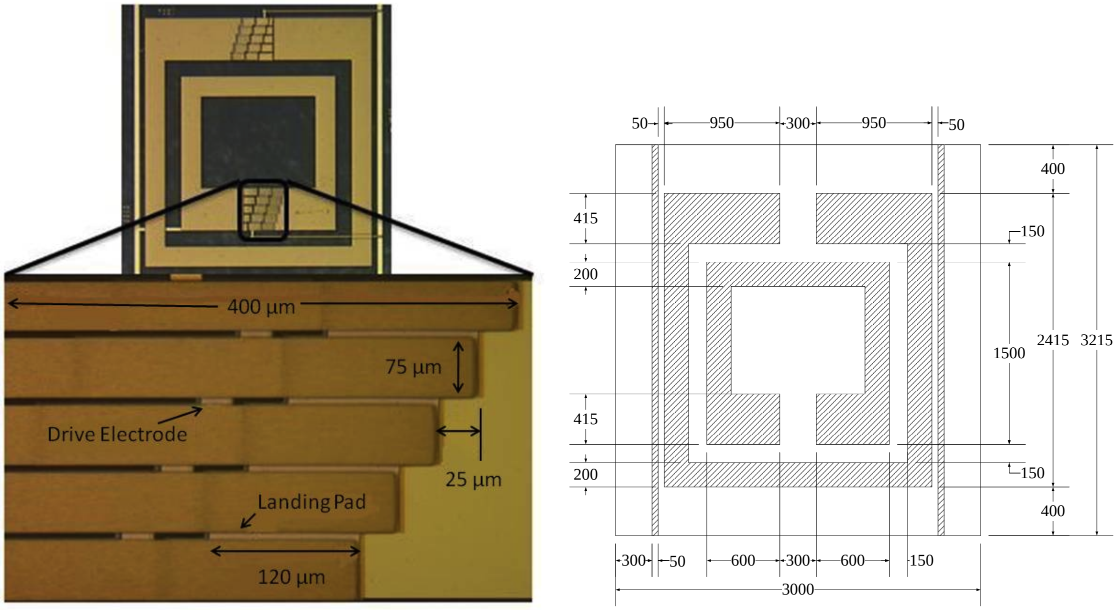

(a) (b)

Figure 2. AFIT-designed adaptive metamaterial structure. (a) A picture from a previous design iteration shows the basic structure and MEMS device [34]. In the latest design, a few of the dimensions are slightly different. (b) The dimensions in μm for the latest design iteration of the basic unit cell.

shown to change the dispersive location of the resonance regions of the device. The device was also examined separately in a previous AFIT research effort without the acquisition of simulation and measurement data from a system that provided usable data within the frequency range of the resonance frequency [23]. Both are acquired in this research effort, fulfilling the second objective of analyzing adaptive metamaterial structures. Additionally, larger sized variants of the proposed structures with different MEMS capacitor layouts are examined using similar computational and measurement techniques. The fusion of the simulation and measurement techniques enhances the understanding of the physical interactions of fields in the presence of the metamaterials.

1.4 Organization of Thesis

This thesis is organized into five chapters. Chapter II provides theoretical background information related to the concepts investigated through this research as well as reviews similar research efforts. Chapter III describes the creation, implementation, and results of computational models used for analysis of both passive and adaptive metamaterial structures. Chapter IV includes descriptions of the procedures, setup, and results from laboratory measurements. Chapter V includes conclusions drawn from this research effort and proposed future research ventures to advance the science.

II. Theory

2.1 Chapter Overview

The purpose of this chapter is to present necessary background information on the electromagnetic theory behind metamaterials and the techniques used to model, test and evaluate their properties, as well as to present current research in the field of passive and adaptive metamaterials.

The basic theory presented in this chapter addresses the research objectives laid out in Chapter I. First, the published methods of characterizing field behavior are described. These methods will be used in later chapters to analyze metamaterial structures. Relevant simulation methods are also described, as this research effort makes use of computational electromagnetics techniques.

In addition to the basic theories, recently published research results from efforts to characterize metamaterials are discussed in this chapter as well as their relevance to the material presented in later chapters.

2.2 Characterization of Metamaterials

There is controversy over the proper explanation of the physical phenomena observed when metamaterials are subjected to electromagnetic waves. Many researchers believe that these embedded structures can display effective material parameters and can be represented as effective media. Other researchers believe that the effective media explanation is not complete and posit that surface wave models are a more physically accurate depiction of the physics associated with the electromagnetic interaction.

The controversy stems from the implications of materials that have negative permittivity and permeability values, an unnatural phenomenon. This section provides background on effective media with negative permittivity and permeability frequency bands and describes the construction of these structures. This section also examines a particular counterclaim to the effective media theory. Proponents of the counterclaim believe the phenomena observed can be explained by surface wave models.

2.2.1 Negative Index of Refraction.

This concept of materials with negative permittivity and permeability was first introduced by Veselago in [46]. In his work, Veselago expounds upon the basic electromagnetic theory behind these materials and introduced left handed propagation. Maxwell's equations and the constitutive relations describe the behavior of electromagnetic fields in a material. Maxwell's curl equations for time harmonic fields in a source-free region along with the constitutive relations are [2]

$$\nabla \times \boldsymbol{E} = -j\omega \boldsymbol{B}, \tag{1a}$$

$$\nabla \times \boldsymbol{H} = j\omega \boldsymbol{D}, \tag{1b}$$

$$\boldsymbol{D} = \epsilon \boldsymbol{E}, \tag{1c}$$

$$\boldsymbol{B} = \mu \boldsymbol{H}, \tag{1d}$$

where $\boldsymbol{E}$ and $\boldsymbol{H}$ are the electric and magnetic field vectors respectively, $\boldsymbol{D}$ and $\boldsymbol{B}$ are the electric and magnetic flux densities respectively, c is the speed of light in free space, ϵ is the electric permittivity of the medium, μ is the magnetic permeability of the medium, and j is the imaginary unit ($j = \sqrt{-1}$). For an electromagnetic field with a single angular frequency ω and wave vector $\boldsymbol{k}$, Equation (1), simplifies for plane waves to [46]

$$
\begin{aligned}
\boldsymbol{k} \times \boldsymbol{E} &= \frac{\omega}{c}\mu \boldsymbol{H}, \qquad (2a)\\
\boldsymbol{k} \times \boldsymbol{H} &= -\frac{\omega}{c}\epsilon \boldsymbol{E}. \qquad (2b)
\end{aligned}
$$

If the values of permittivity and permeability are simultaneously negative in Equation (2), $\boldsymbol{E}$, $\boldsymbol{H}$, and $\boldsymbol{k}$ will be a left-handed set of vectors, leading to the title of left-handed material (LHM)[46]. In contrast, when $\boldsymbol{E}$, $\boldsymbol{H}$, and $\boldsymbol{k}$ form the traditional set of right handed vectors, the material is referred to as right-handed material (RHM). Also, as noted by Veselago in [46], the Poynting vector ($\boldsymbol{S}$), $\boldsymbol{E}$, and $\boldsymbol{H}$ always form a right-handed set of vectors, regardless of the signs of ϵ and μ [46]. From Balanis, the Poynting vector is defined by [2]

$$\boldsymbol{S} = \frac{1}{2}\Re\left[\boldsymbol{E} \times \boldsymbol{H}^{*}\right], \qquad (3)$$

where $\Re$ denotes the real part and the * symbol denotes the complex conjugate. Equation (3) shows that the Poynting vector is independent of ϵ and μ and therefore is independent of material classification. Electromagnetic fields incident on LHM experience negative refraction. This can clearly be seen through examination of the boundary condition of the interface between two media where there are no sources. Figure 3 shows this interface, where the top region is the RHM. The boundary conditions at this interface are [2]

$$\hat{n} \times (\boldsymbol{E_2} - \boldsymbol{E_1}) = 0, \tag{4a}$$

$$\hat{n} \times (\boldsymbol{H_2} - \boldsymbol{H_1}) = 0, \tag{4b}$$

$$\hat{n} \cdot (\epsilon_2 \boldsymbol{E_2} - \epsilon_1 \boldsymbol{E_1}) = 0, \tag{4c}$$

$$\hat{n} \cdot (\mu_2 \boldsymbol{H_2} - \mu_1 \boldsymbol{H_1}) = 0, \tag{4d}$$

where the 1 and 2 subscripts refer to the medium 1 and medium 2 respectively and $\hat{n}$ refers to the boundary normal directed into medium 2. According to Equations (4c) and (4d), the normal components of $\boldsymbol{E}$ and $\boldsymbol{H}$ change sign when the field crosses the boundary between a right handed material and a left handed material.

As seen in Equations (2), the normal component of $\boldsymbol{k}$ also changes direction. These three sign reversals, along with the boundary conditions and the requirement for $\boldsymbol{E}$, $\boldsymbol{H}$, and $\boldsymbol{k}$ to be left-handed mean that the electromagnetic field in the LHM will be on the same side of the z-axis as it is in the RHM [46]. This is not the case for a boundary between two RHM. This field set will only satisfy Snell's law if the index of refraction (n) for a LHM is negative, causing refraction at the boundary of a RHM and a LHM to be called negative refraction [46]. Since the reflected ray is in the same medium as the incident ray, it will be in the same direction regardless of the second medium [46]. Figure 4 shows a comparison between positive and negative refraction.

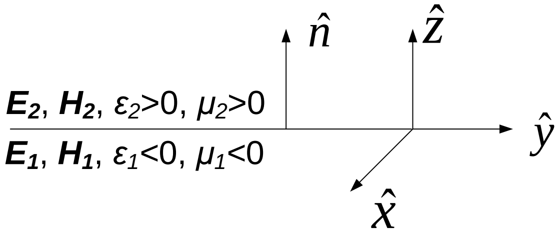

Figure 3. Boundary between RHM and LHM. Medium 2 is the RHM

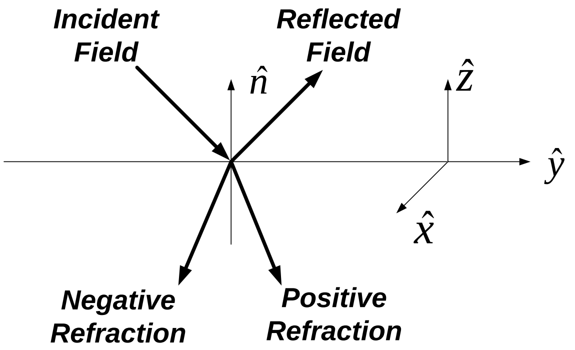

Figure 4. Comparison between negative and positive refraction. When an electromagnetic field crosses the boundary between a LHM and RHM, the refracted field appears in a different plane than an electromagnetic field that undergoes positive refraction. The reflected field is not affected by the classification of the second media.

In order to satisfy Snell's law, the definition of n is modified by the inclusion of the parameter p, defined to be one if the material is RHM and negative one if the material is LHM. Therefore, n can be calculated from ϵ and μ for both material types as [46]

$$n = \frac{p_1}{p_2} \left| \sqrt{\frac{\epsilon\mu}{\epsilon_0\mu_0}} \right| , \tag{5}$$

where the subscripts 1 and 2 denote the materials on either side of the boundary and ϵ_0 and μ_0 are the permittivity and permeability of free space respectively.

Snell's law of refraction can now be rewritten to account for the type of media. Snell's law of refraction to find the angle of transmission (φ_t) through the second material is [7]

$$\varphi_t = \frac{\mathrm{sgn}(n_1)}{\mathrm{sgn}(n_2)} \arcsin\left(\frac{|n_1|}{|n_2|} \sin\varphi_i\right) , \tag{6}$$

where φ_i is the angle of incidence.

2.2.2 Realization of Negative Refractive Index.

When LHM was first discussed by Veselago in the late 1960's, there were no known substances that had both $\epsilon < 0$ and $\mu < 0$, however in the 1990's researchers discovered methods that would supposedly create media with simultaneously negative effective ϵ and μ values. These effective parameters are created by embedding metallic structures in dielectric materials. These effective parameters are only valid for wavelengths longer than the size and separations of the structures, where the material appears homogeneous [47].

2.2.2.1 Negative Permittivity Metamaterials.

Pendry *et al.* show that a material containing a periodic lattice of metallic wires can have an effective permittivity [30]. By confining electrons to thin wires, the mass of the electrons is enhanced, therefore reducing the plasma frequency [30]. For a wire lattice with separation distance a and radius r_w, the plasmon frequency (ω_p) is reduced to [30]

$$\omega_p^2 = \frac{2\pi c_0^2}{a^2 \ln(a/r_w)}. \tag{7}$$

The plasma frequency is the frequency at which the electron density oscillates in a metal. Incident fields at a frequency higher than the plasma frequency penetrate the metal as if it were transparent; whereas fields below the plasma frequency are exponentially decayed [15]. The plasma frequency of Equation (7) produces a dispersive expression for the effective ϵ [30]

$$\epsilon = 1 - \frac{\omega_p^2}{\omega(\omega + \frac{j\epsilon_0 a^2 \omega_p^2}{\pi r_w^2 \sigma})}, \tag{8}$$

where σ is the conductivity of the metal used for the wires. The results of Equation

(8) will have a negative real component when $\omega < \omega_p$ [30].

2.2.2.2 Negative Permeability Metamaterials.

Pendry *et al.* show in [29] that by embedding certain microstructures into a material, a medium can be made to have an effective μ. The structures are arranged in a periodic cubic array with dimension a. Pendry *et al.* claim that if $a \ll \lambda$, where λ is the wavelength of the incident radiation, then the incident waves will be largely unaffected by the microstructures and the medium can be characterized by an effective permeability [29].

One of the structures introduced by Pendry *et al.* in [29] consists of two concentric SRR particles. Figure 5 shows the geometry of this structure. The gap in the SRR particles prevent current from flowing around any one ring, however the capacitance between the two rings allows current to circulate. The effective μ of this structure is [29]

$$\mu = 1 - \frac{\frac{\pi r_{SRR}^2}{a^2}}{1 + j\frac{2\ell R_1}{\omega r_{SRR}\mu_0} - \frac{3dc^2}{\pi\omega^2 \ln\frac{2w}{d} r_{SRR}^3}}, \tag{9}$$

where r_{SRR} is the radius of the inner SRR, w is the width of the SRR traces, d is the difference between the outer radius of the inner SRR and the inner radius of the outer SRR, ℓ is the separation length between the SRR layers, and R_1 is the resistance of a unit length of the metal sheets that make up the SRR particles measured around the circumference.

In deriving Equation (9), constraints are placed on the dimensions of the structure [29]

$$\begin{aligned} r_{SRR} &\gg w, && \text{(10a)} \\ r_{SRR} &\gg d, && \text{(10b)} \\ \ell &< r, && \text{(10c)} \\ \ln\frac{w}{d} &\gg \pi. && \text{(10d)} \end{aligned}$$

The frequency-dependence of Equation (9) has a resonant form, and the resonant angular frequency (ω_0) is of the form [29]

$$\omega_0 = \sqrt{\frac{3dc^2}{\pi^2 r_{SRR}^3}}, \tag{11}$$

where c refers to the speed of light in the substrate containing the SRR particles.

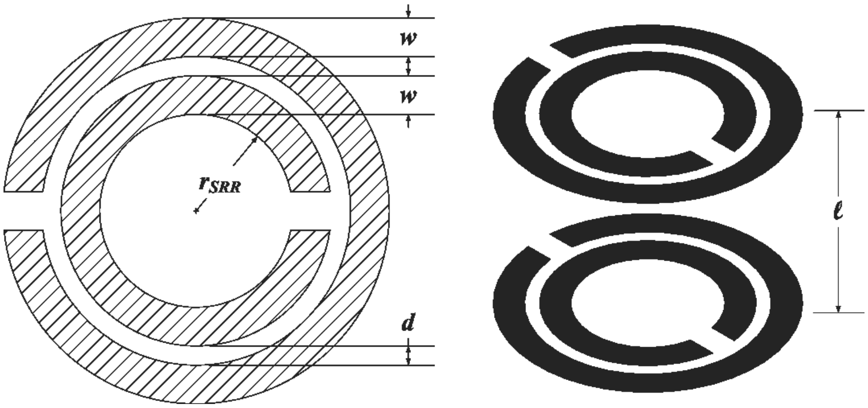

Figure 5. The geometry of the SRR structure proposed in [29].

Pendry *et al.* provide an example calculation using the dimensions of Table 1 and $R_1 = 200.0\ \Omega/m$. It is noted that these values do not satisfy Equation (10), but "the inequalities are only important to the accuracy of [Equation (9)], not to the functioning of the structure" [29]. Figure 6 shows the effective μ given by Equation (9). The effective μ shows a resonant behavior at 13 GHz. Equation (9) also predicts a negative μ band between approximately 13.5 and 14.5 GHz.

Table 1. Dimensions for the SRR example given in [29].

Parameter	Value (mm)
a	10
w	1.0
d	0.10
ℓ	2.0
r_{SRR}	2.0

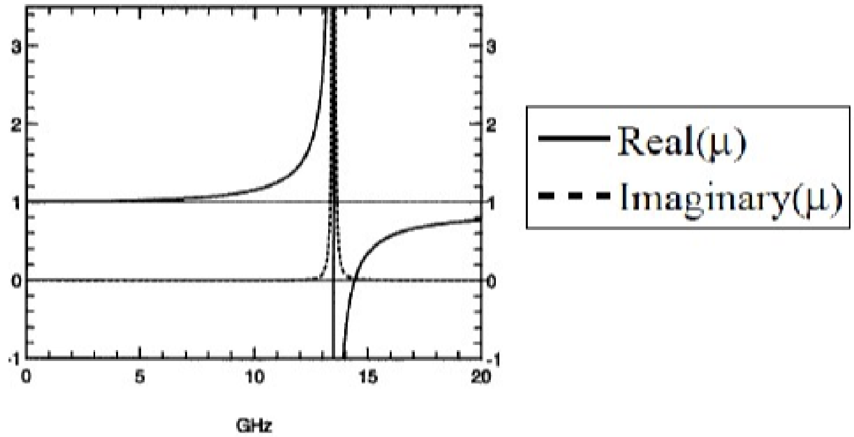

Figure 6. The effective μ for the SRR example structure in [29]. The structure displays a resonant behavior near 13 GHz and μ is negative between approximately 13.5 and 14.5 GHz.

2.2.2.3 Double-Negative Metamaterials.

A medium with simultaneously negative ϵ and μ values is created by including wire lattice and SRR particles in the same structure. Smith *et al.* present this structure and experimentally measure its performance in [42]. Figure 7 shows the experimental comparison between a metamaterial structure consisting of just SRR particles (solid line) and a metamaterial structure consisting of SRR particles and a wire lattice (dashed line). The SRR particles alone create a stop band near the resonance frequency where the effective μ is negative. The combination of the SRR and wire particles create a passband near the resonance frequency.

Smith *et al.* lack analysis of the electric response of the SRR particles in [42], however this is addressed by Simovski *et al.* in [41]. Simovski *et al.* show that

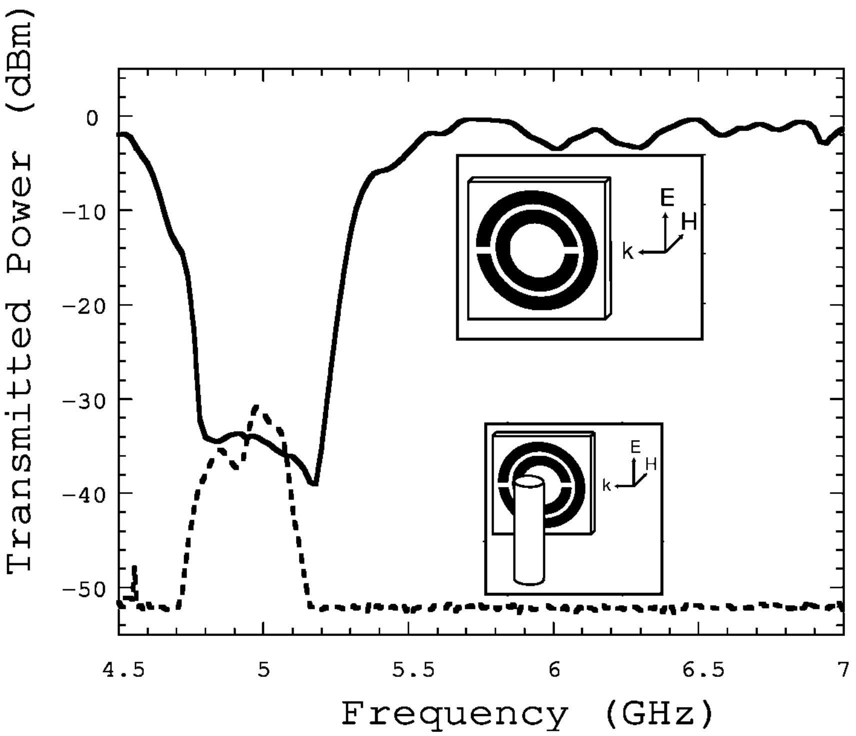

Figure 7. Experimental transmission results for a DNG metamaterial based on an SRR structure and an SRR with a wire array. The insets shows the geometry for each of the structures. The solid line shows that the transmitted power for the SRR metamaterial acts like a stop band. The dashed line indicates that the combination SRR and wire lattice metamaterial acts like a passband in the band where ϵ and μ are negative [42].

the interaction between the SRR particles and wire traces influence the effective permittivity due to the electric response of the SRR particles [41].

This thesis deals only with structures including both SRR particles and wire traces. All numerical simulations in this thesis take into account the electric response of the SRR particles.

2.2.3 Surface Waves in Metamaterials.

Some researchers believe that negative refraction is impossible and that the radiation pattern from an illuminated metamaterial structure can be explained by surface waves. One of those researchers, Ben Munk, published a book describing his objections to the effective medium theory described in the sections above [26].

There are four basic theories inherent to the effective medium theory of metamaterials that Munk disputes: that certain metamaterial structures can have an effective negative index of refraction, that the phase of a signal inside a medium with an effective negative index of refraction advances as it moves away from the source, that evanescent waves grow in amplitude as they propagate away from the source, and that $\boldsymbol{E}$, $\boldsymbol{H}$, and $\boldsymbol{k}$ form a left-handed triplet [26].

Munk notes that the concept of a medium with negative effective values for permittivity and permeability and, thus a negative effective index of refraction leads to the notion of negative time and violates causality. To illustrate his argument, he notes that the distance traveled by a wave in any medium (d_m) is given by [26]

$$d_m = \frac{\omega t}{n k_0}, \tag{12}$$

where k_0 is the wavenumber for freespace. The quantities k_0, d_m, and ω in Equation (12) are taken to be positive. Therefore, n and t must be the same sign. The conclusion is that a medium with $n < 0$ would require negative time [26].

Rather than approaching metamaterials as effective media, Munk argues that the formulation for predicting scattering from an FSS will apply. Using this model, Munk states "the direction of refraction in air is determined solely by the interelement spacings D_x and D_z as well as the direction $\hat{s}$ of the incident field, never by the element type" [26].

According to Munk, for a metamaterial slab to be considered continuous, the interelemental spacing must be less than $\lambda/2$ [26]. This condition on the interelemental spacing also results in the suppression of grating lobes. Assuming the array is infinite, reradiation from the metamaterial slab is only possible in two directions: the forward direction (along same path as incident field) and specular reflection direction. This is because only Floquet currents are present in an infinite array [27]. For an infinite array in the x- and z-directions, the radiated fields will be in the direction of $\hat{r}_\pm$ given by [25]

$$\hat{r}_\pm = \hat{x}\left(s_x + m_1\frac{\lambda}{D_x}\right) \pm \hat{y}r_y + \hat{z}\left(s_z + m_2\frac{\lambda}{D_z}\right), \tag{13a}$$

$$r_y = \sqrt{1 - \left(s_x + m_1\frac{\lambda}{D_x}\right)^2 - \left(s_z + m_2\frac{\lambda}{D_z}\right)^2}, \tag{13b}$$

where s_x and s_z are the x- and z-components respectively of a vector pointing in the direction of propagation of the incident plane wave, m_1 and m_2 are the Floquet modes in the x- and z-directions respectively, and D_x and D_z are the interelemental spacings in the x- and z-directions respectively. Note that the waves radiated from the array are inhomogeneous.

The principle direction is given by the condition $m_1 = m_2 = 0$ [26]. In this case, Equation (13) reduces to $\hat{r}_\pm = \hat{x}s_x \pm \hat{y}r_y + \hat{z}s_z$ and $r_y = \sqrt{1 - s_x^2 - s_z^2} = s_y$. The direction of the reflected field becomes $r_- = \hat{x}s_x - \hat{y}s_y + \hat{z}s_z$ while the direction of the transmitted field becomes $r_+ = \hat{x}s_x + \hat{y}s_y + \hat{z}s_z$. As expected, the reflected field will be in the specular direction. Furthermore, the direction of the transmitted field remains the same as the incident field.

For a finite array, the radiated fields take on a pattern where mainlobes are aligned along the forward and specular reflection directions. This pattern will also contain sidelobes due to the residual currents. The residual currents can be broken down into surface wave and end currents. Radiation from the end currents is typically much less than radiation from the surface waves. Radiation from surface waves is generally at least 14 to 20 dB lower than the main beam and notably lower than can be explained by loses in the material used to make the metamaterial [26]. These levels are similar to those found in many negative refraction experiments [26].

The two dissenting methods for describing field behavior in metamaterials discussed in this chapter are key background elements of this research effort, however, this thrust does not attempt to settle the debate. In later chapters, scattering predictions for metamaterials will be made using a commercial full-wave solver where the details of the metamaterial structure are modeled. Thus the controversy of the two theories presented previously is avoided. The following section discusses the computational techniques of the commercial full-wave electromagnetics solver used in this thesis.

2.3 Computational Techniques

The computational tool used to characterize the metamaterial structures presented in later chapters is CST Microwave Studio® (MWS®). CST MWS® is a commercial full-wave electromagnetics solver that primarily uses the finite integration technique (FIT). CST MWS® can employ the FIT in the time- or frequency-domain. The results from the simulations are often provided in the form of scattering parameters or S-parameters. From S-parameters, effective material parameters can be calculated.

This section describes basic background theory on the FIT, the method used in this research to extract the effective material parameters, and some recently published articles on modeling metamaterials.

2.3.1 Finite Integration Technique.

The computational method used for this study is the FIT. The finite integration technique is similar to the finite difference time-domain (FDTD) technique. The computational domain is divided into two grids, denoted G and $\tilde{G}$. The grids are shown in Figure 8 [1]. The grids are spaced so that the corner of a cell in one grid is collocated with the center of a cell in the other grid [6]. The state variables of the FIT are referred to as the grid electric voltage vector ($\boldsymbol{e}$), magnetic voltage vector ($\boldsymbol{h}$), magnetic induction flux ($\boldsymbol{b}$), electric charge current ($\boldsymbol{j}$), and electric displacement flux ($\boldsymbol{d}$), with vectors denoted with bold letters. The quantities $\boldsymbol{e}$, $\boldsymbol{b}$, and electric charge density (q_{ev}) are defined on G; while $\boldsymbol{d}$, $\boldsymbol{h}$, and $\boldsymbol{j}$ are defined on $\tilde{G}$ [6]. The state variables for the ith grid cell are defined on both the edges and facets of the cells by [49]

$$e_i = \int_{L_i} \boldsymbol{E} \cdot d\boldsymbol{s}, \tag{14a}$$

$$b_i = \int_{A_i} \boldsymbol{B} \cdot d\boldsymbol{A}, \tag{14b}$$

$$d_i = \int_{\tilde{A}_i} \boldsymbol{D} \cdot d\boldsymbol{A}, \tag{14c}$$

$$h_i = \int_{\tilde{L}_i} \boldsymbol{H} \cdot d\boldsymbol{s}, \tag{14d}$$

$$j_i = \int_{\tilde{A}_i} \boldsymbol{J} \cdot d\boldsymbol{A}, \tag{14e}$$

where L_i and $\tilde{L}_i$ are the lengths of the ith cell edges in G and $\tilde{G}$ respectively, A_i and $\tilde{A}_i$ are the areas of the ith cell facets in G and $\tilde{G}$ respectively, and $\boldsymbol{J}$ is the electric current vector.

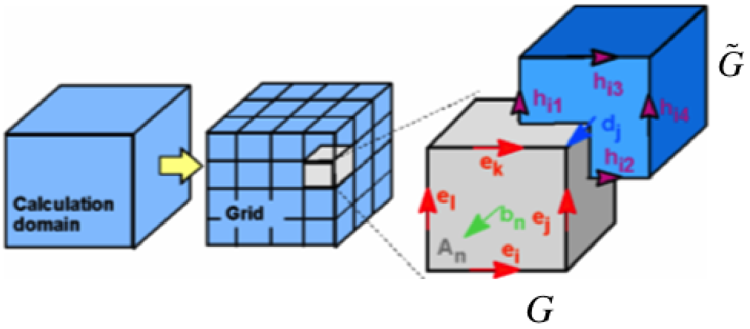

Figure 8. Computational grids for the FIT.[1]

The FIT is based on the integral form of Maxwell's equations. Assuming no magnetic source current, these equations are [49]

$$\oint_{\partial A} \boldsymbol{E} \cdot d\boldsymbol{s} = -\frac{d}{dt}\int_{A} \boldsymbol{B} \cdot d\boldsymbol{A}, \tag{15a}$$

$$\oint_{\partial A} \boldsymbol{H} \cdot d\boldsymbol{s} = \int_{A} \left(\frac{d}{dt}\boldsymbol{D} + \boldsymbol{J}\right) \cdot d\boldsymbol{A}, \tag{15b}$$

$$\oint_{\partial V} \boldsymbol{D} \cdot d\boldsymbol{A} = \int_{V} q_{ev} dV, \tag{15c}$$

$$\oint_{\partial V} \boldsymbol{B} \cdot d\boldsymbol{A} = 0. \tag{15d}$$

Support topological matrix operators ($\boldsymbol{C}= \oint_{\partial A} \cdot d\boldsymbol{s}$, $\boldsymbol{S}= \oint_{\partial V} \cdot d\boldsymbol{A}$) and ($\tilde{\boldsymbol{C}}= \oint_{\partial \tilde{A}} \cdot d\boldsymbol{s}$, $\tilde{\boldsymbol{S}}= \oint_{\partial \tilde{V}} \cdot d\boldsymbol{A}$) are defined for G and $\tilde{G}$ respectively. The elements of $\boldsymbol{C}$, $\boldsymbol{S}$, $\tilde{\boldsymbol{C}}$, and $\tilde{\boldsymbol{S}}$ can only take on values of -1, 1, or 0, representing merely topological information [49]. If evaluated for each facet or cell of the mesh, then Equation (15) can be transform into [49]

$$\boldsymbol{C}\boldsymbol{e} = -\frac{d}{dt}\boldsymbol{b}, \tag{16a}$$

$$\tilde{\boldsymbol{C}}\boldsymbol{h} = \frac{d}{dt}\boldsymbol{d} + \boldsymbol{j}, \tag{16b}$$

$$\tilde{\boldsymbol{S}}\boldsymbol{d} = q_{es}, \tag{16c}$$

$$\boldsymbol{S}\boldsymbol{b} = 0, \tag{16d}$$

using the support operators and the definitions in Equation (14).

Figure 9 can be used illustrate the FIT scheme. Considering Faraday's Law, Equation (15a), the closed integral on the left side of the equation can be written as the sum of four grid voltages. The time derivative of the magnetic flux defined on the enclosed primary cell facet represents the right side of the equation. Repeating this procedure for all available cell facets summarizes the calculation rule in a matrix formulation using $\boldsymbol{C}$ as the discrete curl operator [1] .

The constitutive relation describing the relationship between $\boldsymbol{E}$, $\boldsymbol{J}$, and σ is [2]

$$\boldsymbol{J} = \sigma \boldsymbol{E}. \tag{17}$$

The constitutive parameters ϵ, μ, and σ, are discretized in both G and $\tilde{G}$ and are represented by the matrices $\boldsymbol{M_\epsilon}$, $\boldsymbol{M_\mu}$, and $\boldsymbol{M_\sigma}$ respectively. Thus, the constitutive relations of Equations (1c), (1d), and (17) are converted to the discrete constitutive relations and become [36]

$$\begin{aligned} \boldsymbol{d} &= \boldsymbol{M_\epsilon e}, && (18a) \\ \boldsymbol{b} &= \boldsymbol{M_\mu h}, && (18b) \\ \boldsymbol{j} &= \boldsymbol{M_\sigma e} + \boldsymbol{j_s}, && (18c) \end{aligned}$$

where the source currents ($\boldsymbol{j_s}$) have been included with $\boldsymbol{j}$. Equation (18) is where the first inaccuracies due to spatial discretization are introduced because the material

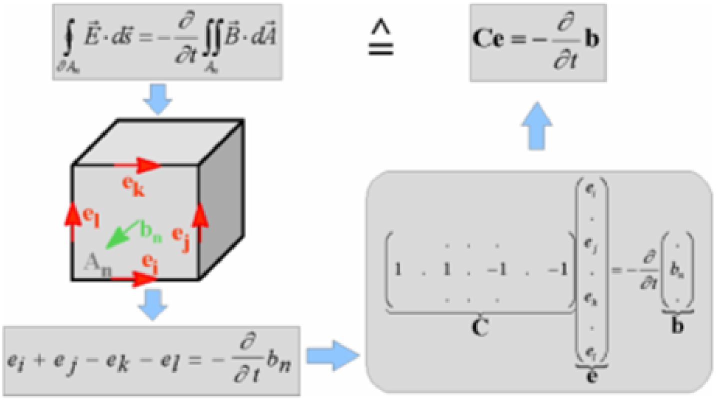

Figure 9. FIT example using Faraday's Law.[1]

parameters are spatially averaged [36].

Equations (16) and (18) form a complete system of equations that can be solved in the time-domain. Time-domain calculations are especially useful for broadband calculations. By defining a specific signal for the frequency range of interest, the corresponding time-domain signal can be found by computing the inverse Fourier transform. The time-domain signal is then used as the excitation signal and the time-domain solution is found using Equations (16) and (18). The solution can be transformed back into the frequency-domain using a Fourier transform [50]. While this procedure does involve transformations to and from the time-domain, it only requires one solution to Maxwell's equations. Generally speaking, solving Maxwell's equations takes considerably longer than Fourier transforms, so this procedure can produce results over a frequency band relatively quickly. A potential drawback is that in the time-domain Equations (16) and (18) have to be repeatedly computed until steady-state criteria are met. For resonant structures, this may become very computationally intensive. Since metamaterial structures are resonant by design, a frequency-domain implementation of Equations (16) and (18) is desirable.

For frequency domain calculations, Equation (16) can be re-written in the frequency-domain (assuming the time harmonic case) by substituting the complex frequency $j\omega$ for d/dt. The frequency-domain version of Equation (16) along with Equation (18) are solved directly at individual frequency points. This implementation does not have the same steady-state requirement, therefore solutions for resonant structures can be found quickly. However, multiple solutions will be required for multiple frequencies. The number of solutions required can be reduced by using interpolation techniques on the results [50].

2.3.2 Boundary Conditions.

The computational domain must be terminated appropriately to obtain accurate solutions from the FIT. CST MWS® can employ several different boundary conditions. The boundary conditions most relevant to this research are perfect electric conductor (PEC), perfect magnetic conductor (PMC), open, and periodic or unit cell.

PEC and PMC boundary conditions are relatively straightforward. A PEC material has an infinite electric conductivity. Thus, $\boldsymbol{E}$ inside a PEC material must be zero. PEC materials are often used to approximate good conductors, like metals. A PMC is the magnetic equivalent to a PEC material. That is, inside a PMC material $\boldsymbol{H}$ must be zero. PEC and PMC boundary conditions are mathematically simple to realize. To create a PEC boundary, use $\boldsymbol{E_1} = 0$ in Equations (4a) and (4c). Likewise, for a PMC boundary, substitute $\boldsymbol{H_1} = 0$ into Equations (4b) and (4d).

An open boundary condition is more difficult to implement mathematically. An open boundary simulates an infinite amount of space in that direction. No energy incident on an open boundary is reflected back into the computational domain. CST MWS® realizes an open boundary with a form of the convolution perfectly matched layer (PML). The convolution PML is a robust and computationally efficient mechanism that has very little numerical reflection and can be implemented with the standard FIT or FDTD formulation [3].

Periodic and unit cell or Floquet boundary conditions mirror the computational domain along one axis or two axes respectively. The result for the periodic boundary condition is a structure that is infinitely long in one dimension. The result for the unit cell boundary condition is a structure that is infinitely long in two dimensions. These infinite arrays are created by assuming a known phase progression along the array, allowing the response from the infinite array to be calculated by using the appropriate phase shifts.

2.3.3 Parameter Extraction.

Extraction of effective metamaterial parameters is a critical issue in the characterization of metamaterials, but it is a complicated process. Traditional methods tend to fail when the S-parameters are small in magnitude. Finding the roots of the impedance can be difficult. Further complicating matters is the behavior of the fields in the resonance band. Whether parameter extraction can be accomplished at all in the resonance band is a current topic of debate.

In light of these complexities, Chen *et al.* propose a more stable method for extracting the effective parameters of metamaterials [5]. While their method does not address the issue of field behavior in the resonance band, it is stable enough to work when the S-parameters are small and does pick the correct root for the impedance. The traditional methods calculate the impedance z and index of refraction n of a slab of thickness d_s with [5]

$$\begin{aligned} z &= \pm\sqrt{\frac{(1+S_{11})^2 - S_{21}^2}{(1-S_{11})^2 - S_{21}^2}}, && \text{(19a)} \\ e^{jnk_0 d_s} &= X \pm j\sqrt{1-X^2}, && \text{(19b)} \\ X &= \frac{1}{2S_{21}(1-S_{11}^2+S_{21}^2)}. && \text{(19c)} \end{aligned}$$

The signs of the roots in Equations (19a) and (19b) are determined by [5]

$$\begin{aligned} \Re\{z\} &\geq 0, && \text{(20a)} \\ \Im\{n\} &\geq 0. && \text{(20b)} \end{aligned}$$

The equations above treat n and z independently. However, n and z are related, and Chen *et al.* exploit that relationship to find the appropriate roots. In the case of finding the roots for the impedance, their procedure uses the fact that the wave can not grow in amplitude. Therefore $|e^{jnk_0d}| \leq 1$; where the left side is found with the relationship [5]

$$e^{jnk_0d_s} = \frac{S_{21}}{1 - S_{11}\frac{z-1}{z+1}}. \tag{21}$$

Chen *et al.* note that when finding the roots of Equation (19a), Equation (21) is only necessary when z is small. When z is large, Equation (20a) can be used.

Calculating index of refraction is more complex than finding the impedance. Solving Equation (19b) for n yields [5]

$$n = \frac{1}{k_0d_s}[\Im\{\ln(e^{jnk_0d_s})\} + 2m\pi - j\Re\{\ln(e^{jnk_0d_s})\}], \tag{22}$$

where m is the branch integer of n. From Equation (22) the imaginary part of n can be found with little trouble since Equation (22) gives a unique solution, but the real part of n will require making the proper branch choice. The proposed method is an iterative process that starts by determining which values of m are valid for the first frequency sample. By using the fact that imaginary parts of the relative permittivity and permeability must be positive, Chen *et al.* show for a branch choice to be valid it must satisfy

$$|\Re\{n\}\Im\{z\}| \leq \Im\{n\}\Re\{z\}. \tag{23}$$

If only one value of m satisfies Equation (23), then that value is the proper branch cut for all frequencies. If more than one value of m satisfies Equation (23) at the first frequency, then those solutions should be tested at the other frequencies. The value of m that satisfies at the other frequency values is the correct branch [5].

Note that there may exist a band of frequencies for which no values of m satisfy Equation (23). This is most likely the resonance band. As mentioned above, the process proposed by Chen *et al.* does not address this band. However, for the purposes of this research, the values of m that satisfy the most frequencies will be used as the correct value of m. Therefore, extracted results in the resonance band will be shown.

The extraction of the material parameters creates an effective medium, but the size of that effective medium has not yet been determined. Chen *et al.* present an algorithmic approach to solve for the location of the first boundary of the effective medium as well as its thickness. Their approach minimizes the difference in impedances between metamaterial structures of different thicknesses. However, after using the approach on different types of structures, they conclude that their algorithm is only necessary for two-dimensional and asymmetric one-dimensional metamaterials. For symmetric one-dimensional structures, like the one pictured in Figure 10, the first unit cell boundary is the first effective boundary, and the thickness of the metamaterial structure is the effective thickness [5]. The structures analyzed in this thesis closely resemble the structure shown in Figure 10. Thus, the first unit cell boundary and structure thickness are used for the effective first boundary and thickness.

2.3.4 Computational Studies of Traditional (Passive) Metamaterial Structures.

Computational studies of metamaterials are currently being conducted in both academia and industry. This section provides a sampling of current efforts.

2.3.4.1 Model of Left-Handed Materials Using Finite Element Method.

Smith *et al.* model the LHM shown in Figure 10 in [43]. The structure consists of two concentric SRR particles with openings on opposite sides and a wire embedded further down in the substrate that runs down the center between the opening of the SRR particles. The FR4 substrate has a relative permittivity of 4.4 and a loss tangent of 0.02. The bianisotropy inherent in SRR particles is avoided in this paper by analyzing only one incident polarization. The authors state that the cross-coupling terms are small for this polarization, so their method provides an adequate characterization for the polarization of interest. A similar argument could be made to address the anisotropy of the FR4 substrate.

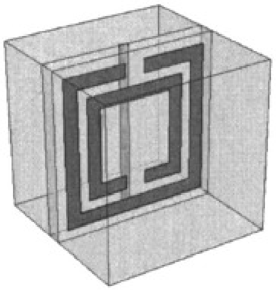

Figure 10. The symmetric structure from [43].

The modeling results published by Smith *et al.* for this structure are shown in Figure 11. To perform the modeling, the authors use Ansoft's HFSS$^{\mathrm{TM}}$. Ansoft HFSS$^{\mathrm{TM}}$ is a commercial full-wave electromagnetics solver that uses the finite element method (FEM). The extraction of the refractive index, impedance, relative permittivity, and relative permeability are performed using a technique similar to the one described in [5]. The results shown in Figure 11 demonstrate an effective negative index band around 10 GHz which has both a negative permittivity and permeability [43].

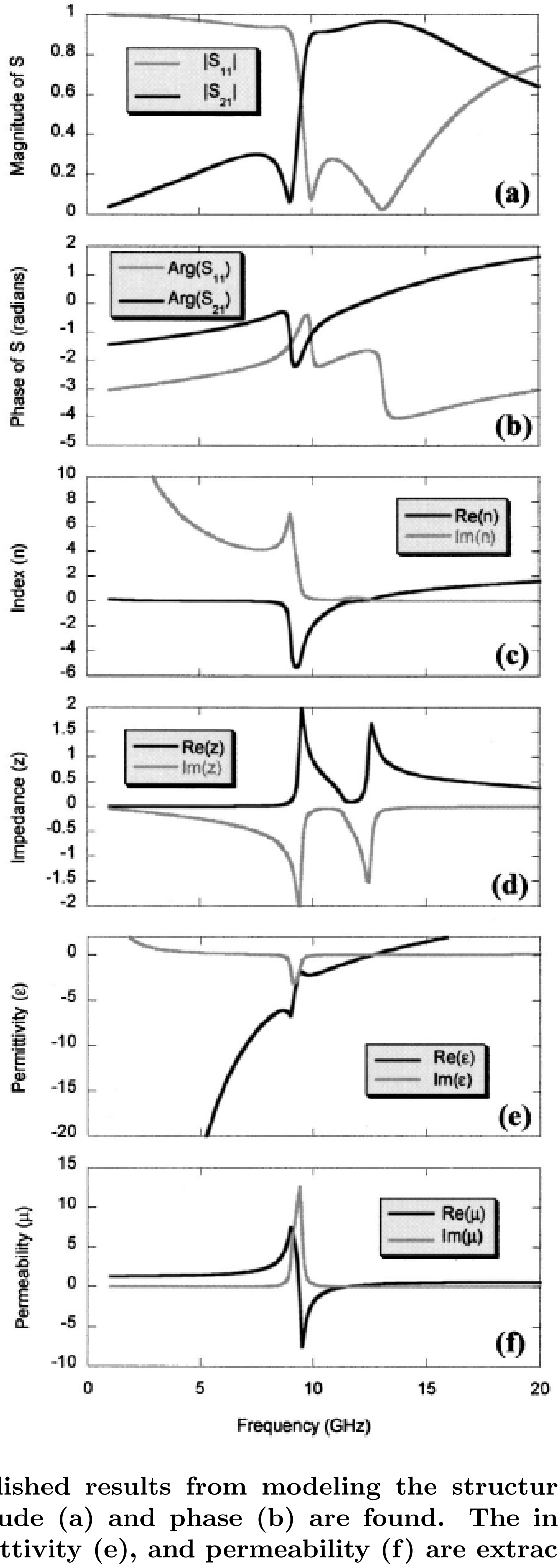

Figure 11. **The published results from modeling the structure of Figure 10. The *S*-Parameters magnitude (a) and phase (b) are found. The index of refraction (c), impedance (d), permittivity (e), and permeability (f) are extracted [43].**

2.3.4.2 Model of Left-Handed Material Using FIT.

Weiland *et al.* [49] present simulation and measurement results of the LHM structure presented in [42]. The structure consists of two concentric, round SRR particles and a single wire. Figure 12(a) shows the structure of the unit cell. CST MWS® is used to simulate the structure. The wire and rings are modeled as a PEC material. A plane wave source is introduced at the left face as shown in Figure 12(a). The boundary conditions at the top and bottom faces are PEC, while the boundary conditions at the forward and rear faces are PMC. A symmetry plane parallel to the top and bottom faces is introduced in the center of the structure to cut the computational domain in half. The time-domain solver is used. The reported solution time was approximately 1/2 hour using an 800 MHz Pentium III processor [49]. The results are shown in Figure 12(b). The data from CST MWS® demonstrate the same passband behavior as the measured results in [42].

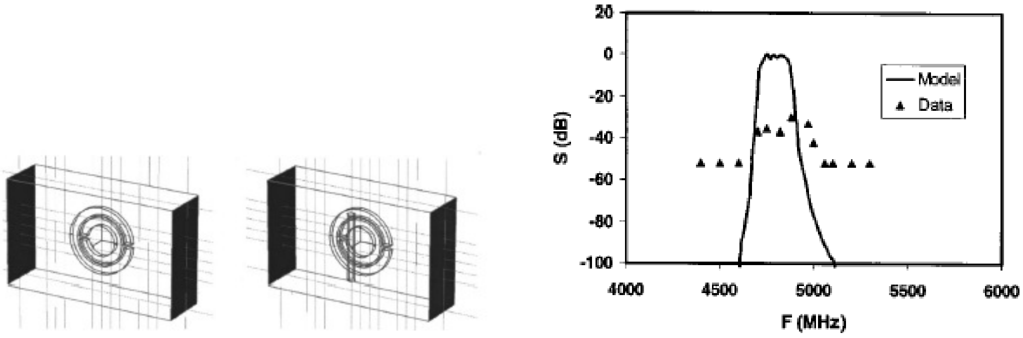

(a) (b)

Figure 12. Simulation model and results of a metamaterial structure analyzed by Weiland *et al.* (a) The unit cell for the computer simulation consists of two concentric SRR particles and a wire. (b) S_{21} for an array of the metamaterial unit cells shows the expected bandpass behavior. The data from the CST Microwave Studio® (solid line) show the same behavior as the measured data (triangles) [49].

Weiland *et al.* also include a parametric study of their model in [49]. They show the dependence of the resonant frequency on the thickness of the SRR particle, radius of the inner SRR, gap width of the SRR particles, gap between the SRR particles in a single unit cell, and the ϵ and μ of the substrate of the structure. The results are shown in Figure 13. The thickness of the SRR particles, SRR radius, and the gap width have only small impacts on the resonant frequency. The largest influence on the resonant frequency comes from varying ϵ and μ of the dielectric substrate [49].

2.3.4.3 Model of Metamaterial Wedge Using FIT.

CST MWS® is used to analyze a metamaterial wedge structure in [16]. The model is shown in Figure 14. The unit cell of the metamaterial structure consists of a square SRR pair and wire trace, similar to the structure analyzed by Smith *et al.* in [43]. A negative refraction band is said to occur between 8.5 and 9 GHz. The unit cells are arranged in a stair-step grid forming a 26.6° wedge. The wedge is illuminated by a waveguide port. The transient-solver in CST MWS® is used to perform the simulation [16].

The electric field magnitudes resulting from the simulation in the negative refraction band are shown in Figure 14(c). The fields are transmitted at an angle of -22°relative to the wedge normal. The transmitted field is on the same side of the wedge normal as the incident field. Using this angle and solving Equation (6), the effective refractive index of the metamaterial wedge in the negative refraction band is $n = -1.17$. Similarly, the electric field magnitudes outside of the negative refraction band are shown in Figure 14(d). The fields are transmitted at an angle of 5°, corresponding to $n = 5.14$ [16].

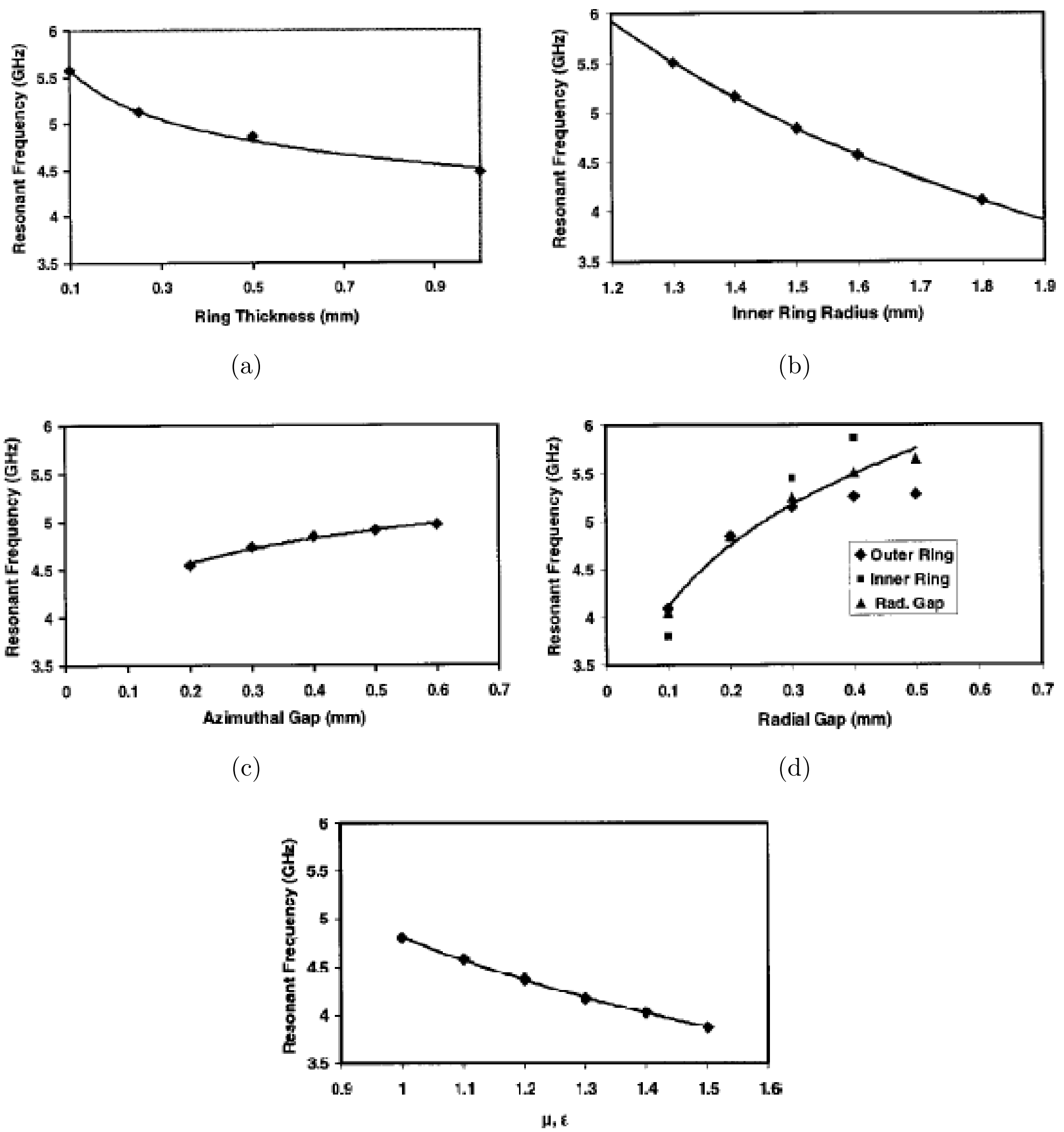

(a) (b)

(c) (d)

(e)

Figure 13. **Results from the parametric study of the DNG structure from [49]. (a) Increasing the thickness of the SRR particles causes a slight decrease in the resonant frequency. (b) Increasing the radius of the SRR particles also decreases the resonant frequency slightly. (c) The width of the gap in the SRR particles has only a slight impact on the resonant frequency. (d) The gap between the SRR particles has a little more influence on the resonant frequency. (e) Only slight changes in the permittivity and permeability of the substrate can impact the resonant frequency [49].**

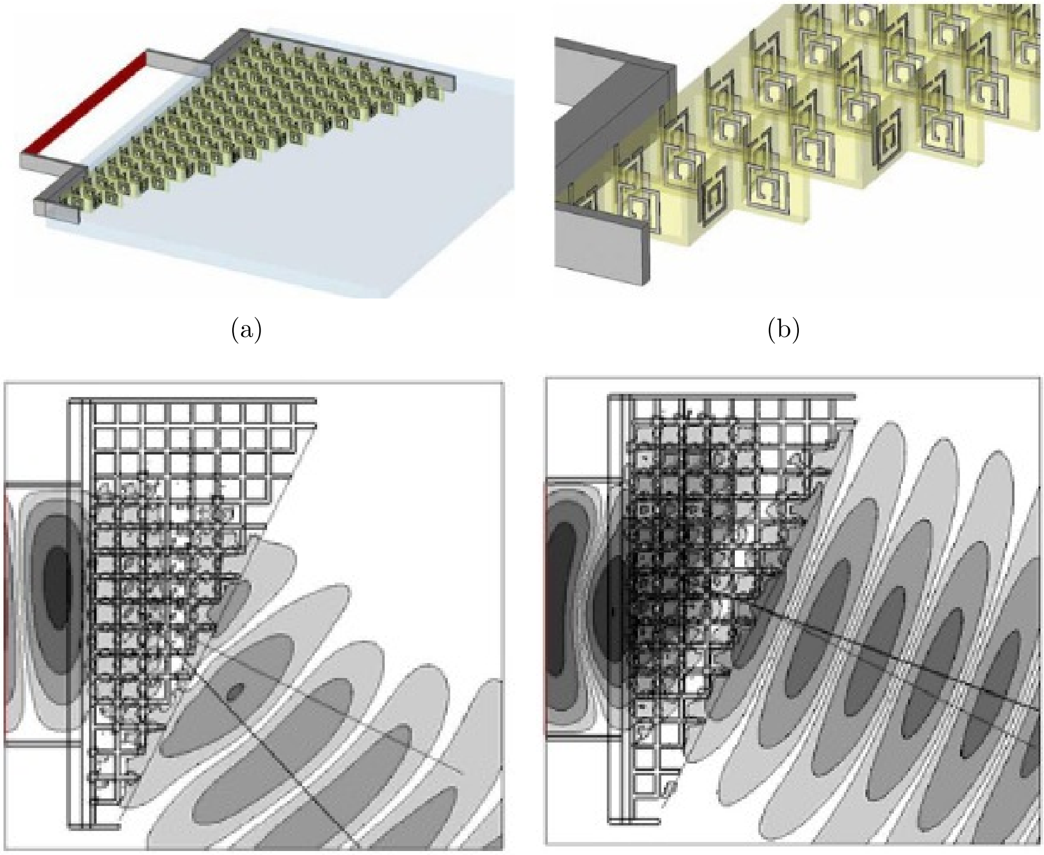

(a) (b)

(c) (d)

Figure 14. **CST MWS® model and results for the metamaterial wedge analyzed in [16]. (a) The model consists of metamaterial unit cells arranged in a stair-step fashion forming a 26.6° wedge. The structure is fed by a waveguide port (the red plane). (b) A close-up view of the model shows that the metamaterial unit cells consist of an SRR pair and a wire trace. (c) Inside the negative refraction frequency band, the diffracted fields are seen emanating at an angle of about 22°. (d) Outside of the negative refraction frequency band, positive refraction occurs [16].**

2.4 Experimental Studies of Traditional (Passive) Metamaterial Structures

Many experiments have been conducted on non-adaptive (passive) metamaterials. This section provides a sampling of experiments relevant to this research thrust.

2.4.1 Experiments with Metamaterial Wedges.

One of the early experiments was carried out by Shelby *et al.* in [40]. In this experiment, a wedge, or prism, containing a lattice of two concentric SRR particles and wires is fabricated and then radiated with microwave energy. The transmission angle through the prism (i.e. the angle where the maximum forward scattering occurs) is measured. The results of the LHM measurements are compared to the results for a material known to be a RHM.

Figure 15 shows the structure, setup, and results of the measurements carried out in [40]. The transmitted power for the LHM and Teflon samples (Figure 15(c)) are normalized "such that the magnitude of the peaks are unity" [40]. The peaks show a discernible difference in the angle of transmission. For the metamaterial prism, the measured angle of transmission is -61°; whereas the Teflon prism shows a transmission angle of 27°. This corresponds to an index of refraction of -2.7 and 1.4 for the LHM and Teflon samples respectively.

The refractive indices of the Teflon and LHM samples as a function of frequency (f) (Figure 15(d)) show that, while the index of refraction for Teflon is constant across the frequency band, the LHM index shows strong dispersion characteristics. The dotted portion of the black line is the region where the wavelength inside the metamaterial sample became too long to use geometrical optics to characterize the scattering (occurs at $f > 10.8$ GHz). The authors also note that anywhere $|n| > 3$, the electromagnetic wave undergoes total internal reflection. Thus, $|n| > 3$ can not be measured using these samples [40]. The solid and dotted red lines show the real and imaginary parts of the LHM's index of refraction calculated using theoretical values for ϵ and μ in Equation (5). A large imaginary component of n (i.e. losses) is shown near the resonance band [40].

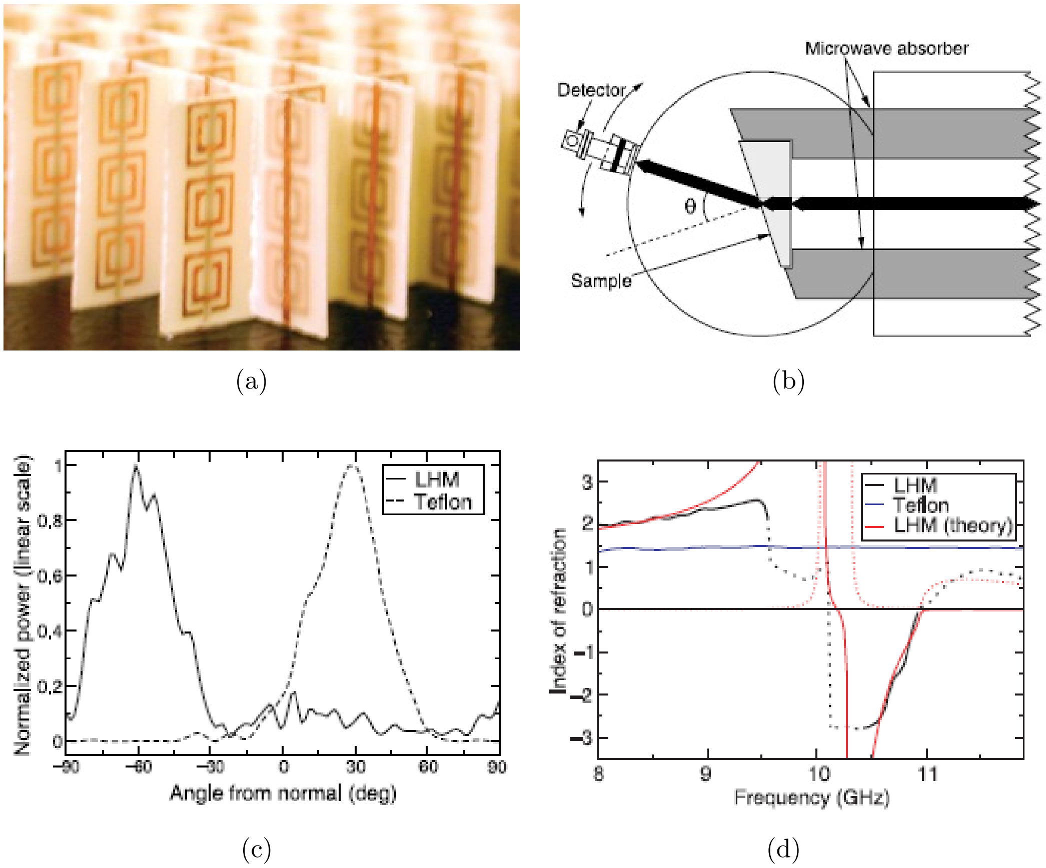

(a) (b)

(c) (d)

Figure 15. Setup and results of an experiment conducted in [40] to determine the index of refraction for a LHM. (a) The LHM is made up of a metamaterial array with two concentric SRR particles and a wire lattice. (b) The right face of the metamaterial prism is subjected to an incident electromagnetic field. The detector is placed on a pivot on the left face of the metamaterial prism and rotated to determine the refraction angle. The thick black line shows what the refraction through the prism would be if the prism index of refraction is positive. (c) At the metamaterial's resonant frequency of 10.5 GHz, the bulk of the power transmitted through the prism appears at an angle of approximately -61°. A Teflon sample with a positive index of refraction shows peak transmission at approximately 27°. Note that the two curves are normalized. (d) The measured index of refraction of the Teflon sample (solid blue line) as compared to the measured index of the LHM (black line). The portions of the black line that are dotted are beyond the researchers' ability to accurately measure. Note that the LHM does show a negative index band near 10.5 GHz [40].

The results of [40] have generated some controversy and other researchers dispute the interpretation of the results. Since the theoretical development of [40] does not account for losses in the material, some claim that the results do not show left-handed behavior [8]. Below 30 GHz, the permittivity of the metamaterial sample is largely imaginary, thus the metamaterial acts more like a metal than a dielectric. This will lead to an inhomogeneous electromagnetic wave that complicates the analysis [8]. The losses due to dispersion are so great at microwave frequencies for this structure that they “swamp any characterization of a net negative real refractive index” [8].

In a later paper [35], these same critical researchers explain that the losses in the structure will cause the transmitted wave to appear to curve towards the thinner end of the wedge as shown in Figure 16. The transmitted field is stronger at the thinner edge of the wedge because it is attenuated less by the losses in the wedge. In effect, the transmitted field is no longer properly aligned with the center of the wedge complicating angle measurements. To show this, the researchers compare the transmission angle of light passing through a wedge of loss-free glass versus lossy gold. The results show that the beam transmitted through the wedge of lossy material bends toward the smaller end of the wedge and appears to show negative refraction despite the fact that the sample is known to have $\Re\{n\} > 0$ [35]. To better show negative refraction experimentally, these researchers argue that a flat sample should be used instead of a wedge so that the losses will be uniform across the sample. They also note that increasing the radius of the wires in the metamaterial sample should reduce the amount of losses present [35].

Another group of researchers also performed the prism experiment, but then also measured a parallelogram-shaped slab [33]. The geometry of the measurement of the parallelogram-shaped metamaterial slab is shown in Figure 17. The advantage of this geometry is that it allows for an even distribution of loss along the wavefront. The

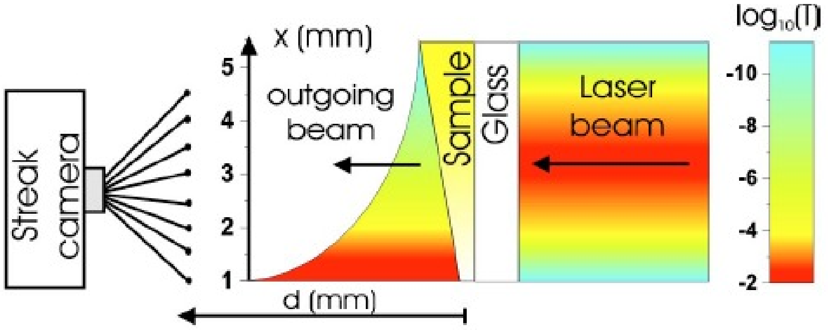

Figure 16. Illustration of light transmission through a wedge made of lossy material. The electromagnetic wave emerging from a wedge-shaped medium with losses will appear to curve towards the smaller end since there will be less losses in that part of the wedge [35].

incident electromagnetic field refracts twice—once at each boundary. This causes the beam to shift away from the centerline. This shift, denoted d_b, is dependent on the index of refraction for the metamaterial slab [33].

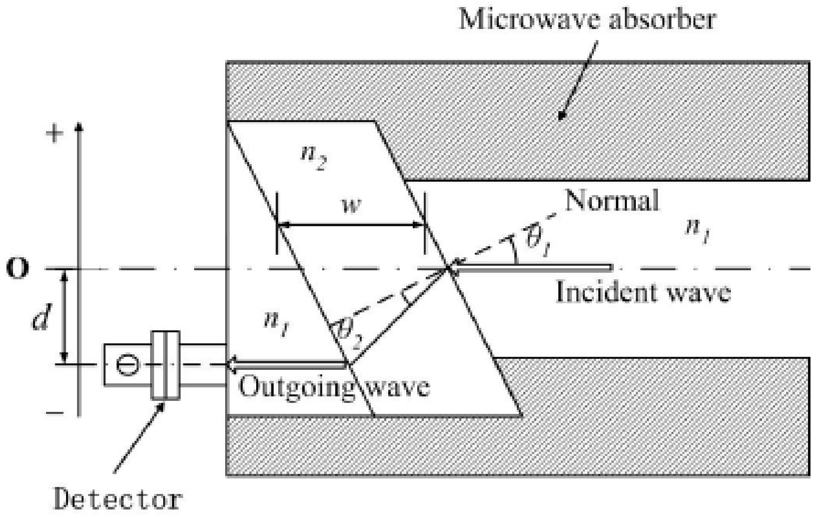

Figure 17. Setup for the measurement of a parallelogram-shaped metamaterial slab. Unlike the wedge-shaped prism, the parallelogram causes an even distribution of loss. The index of refraction for the sample can be determined by the distance the beam is shifted from the centerline [33].

The measurement is conducted on different types of metamaterial structures: a non-concentric SRR and wire structure, two types of omega resonator structures, and an S-shaped resonator structure. The non-concentric SRR and wire structure is similar to structures to be analyzed in this thesis. The metamaterial structure is shown in Figure 18(a). Figure 18(b) shows the results from the measurement. In the resonant frequency band (near approximately 8.7 GHz) the center of the beam shifts to -34 mm. Empty measurements give a reference point O of -13 mm. Thus the beam shifted -21 mm. The direction of the shift indicates that the index of refraction for the wedge is negative in the resonant frequency band [33].

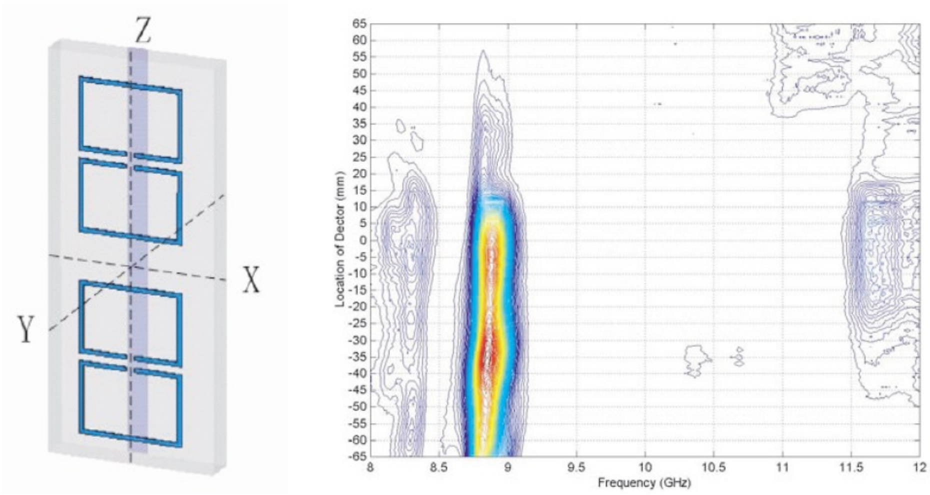

(a) (b)

Figure 18. Basic metamaterial structure and results from the measurement of a parallelogram-shaped slab. (a) The basic unit cell consists of a single wire trace and two non-concentric SRR particles. (b) The results from the measurement show that in the resonant frequency band the beam center shifts to -34 mm (-21 mm from the reference point) [33].

Lundell furthers research of the behavior of electromagnetic fields in the presence of metamaterials by applying bistatic radar cross section (RCS) measurement techniques to a metamaterial wedge in [23]. The wedge cells consist of two concentric split ring resonators and a wire trace. The cells are fabricated into the wedge shown in Figure 19(a) with dimensions as shown in Figure 19(b).

Lundell uses CST MWS® to model a unit cell of the metamaterial and models of varying size in terms of number of cell steps in the wedge. The resonance band is predicted to be between 12.5 GHz and 14.5 GHz. The extracted index of refraction

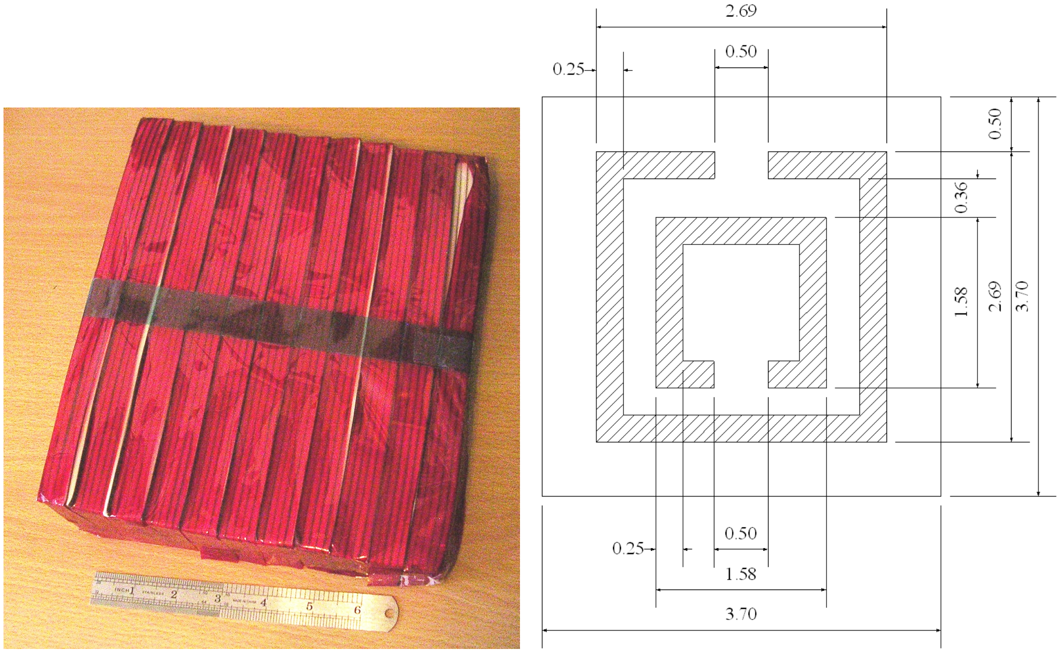

(a) (b)

Figure 19. (a) Wedge metamaterial characterized by Lundell using modeling and free space measurements and (b) the dimensions of the metamaterial wedge's unit cell. All dimensions are in mm. Not shown is the 0.76 mm wide flat wire trace on the backside of the dielectric board containing the SRRs [23].

predicts a negative effective index of refraction in the resonance band with a large imaginary component, resulting in a large amount of attenuation in the wedge at resonance.

Using the effective medium theory and taking into account losses in the wedge, reflection angle results are predicted for the geometry shown in Figure 20(a). The resulting reflection angle prediction is shown in Figure 20(b).

Lundell also makes scattering angle predictions for the wedge using the FSS theory. Table 2 shows the principle forward (transmission into the wedge) and back (reflection from the face of the wedge) return angles. With m_1 and/or m_2 greater than zero in Equation 13, the transmitted/reflected angles become complex at all frequencies, indicating that for Floquet modes $m_1 > 0$ or $m_2 > 0$, the grating lobes are trapped and do not radiate. Additional radiation for these conditions must be

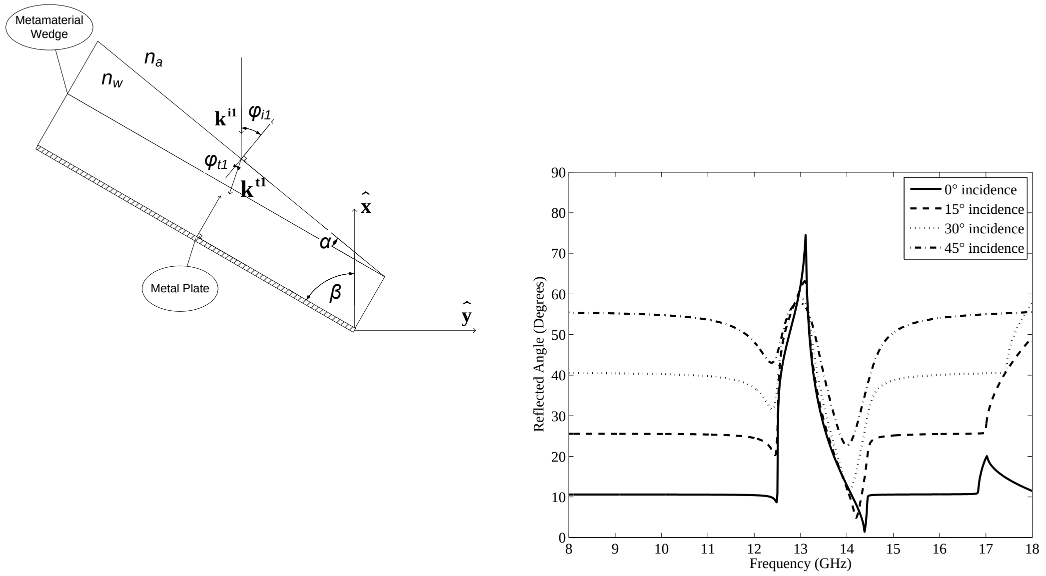

(a) (b)

Figure 20. (a) The geometry for the bistatic RCS measurements of the metamaterial wedge in [23] and the predicted angles transmitted through the metamaterial wedge and reflected off the metal plate taking into account the losses in the metamaterial wedge.

due to residual currents and are not predicted by Lundell [23].

Table 2. Metamaterial wedge principle scattering angles using FSS theory [23].

β (degrees)	Forward Angle (degrees)	Back Angle (degrees)
0	0	21.2
15	30	51.2
30	60	81.2
45	90	111.2

The computational predictions show similar results to the effective medium theory and FSS predictions. The computational results are compared to actual bistatic RCS measurements. The models and measurements show that the dominant scattering mechanism is the specular reflection off of the wedge face. Like the models, the measurements show that the magnitude of the return is reduced in the resonance band, showing penetration into the lossy wedge [23].

A key difference between Lundell's models and measurements is the location of the resonance bands. The approximate resonance bands are shown in Table 3. The resonance bands calculated with the frequency solver better match the measured resonance band. Therefore, for this thesis effort, the frequency solver will be used.

2.4.2 Experiments with Planar Metamaterial Structures.

A group of Chinese researchers conducted free space measurements of a similar double-negative metamaterial structure [44]. The setup and some of the results are shown in Figure 21. For their measurements, alternating circuit boards with square SRRs and wires are arranged vertically (see Figure 21(a)). Horn antennas are used for transmission and reception and are placed on opposite sides of the sample (along the x-axis in Figure 21(a)). The circuit boards are measured at different rotation angles in the xz-plane: 0°, 30°, 60°, and 90°. The circuit boards are also rotated in the xy-plane at the same angles in another set of measurements. At each angle, measurements are made with alternating SRR/wire circuit boards, SRR circuit boards only, wire circuit boards only, and no circuit boards [44].

The results for the 0° rotation angle are shown in Figure 21(b). When only the SRR circuit boards are measured, transmission is reduced by approximately 45 dB in the frequency band between 10.5 and 12.0 GHz. When only the wire circuit boards are present, transmission is reduced throughout the entire frequency band.

Table 3. Metamaterial wedge resonance bands [23]

Data Set	Resonance Band	
	Starting Frequency (GHz)	Ending Frequency (GHz)
Unit cell[1]	12.5	14.5
Mid-size[1]	13	14
Full-size[2]	12	13
Measurement	12.8	14.5

[1] Model uses frequency solver.

[2] Model uses transient solver.

When both the wire and circuit boards are measured, transmission between 12.0 and 13.8 GHz is close to free space transmission, but reduced throughout the remaining frequency band [44]. The researchers interpret these results to mean that the bands that show reduced transmission in the cases of the SRR circuit boards only and wire circuit boards only indicate that either ϵ or μ are negative, but not both. They make this claim by stating that an electromagnetic wave can not propagate when only ϵ or μ are negative. In the case where both circuit boards are present, the band between 12.0 and 13.8 GHz can allow propagation because both ϵ and μ are negative. Outside of that band μ is positive, but ϵ is negative. Thus the wave can not propagate and transmission is reduced [44]. The results from the various angles shows that rotating the circuit boards affects the behavior of the SRR particles more than the behavior of the wire particles [44].

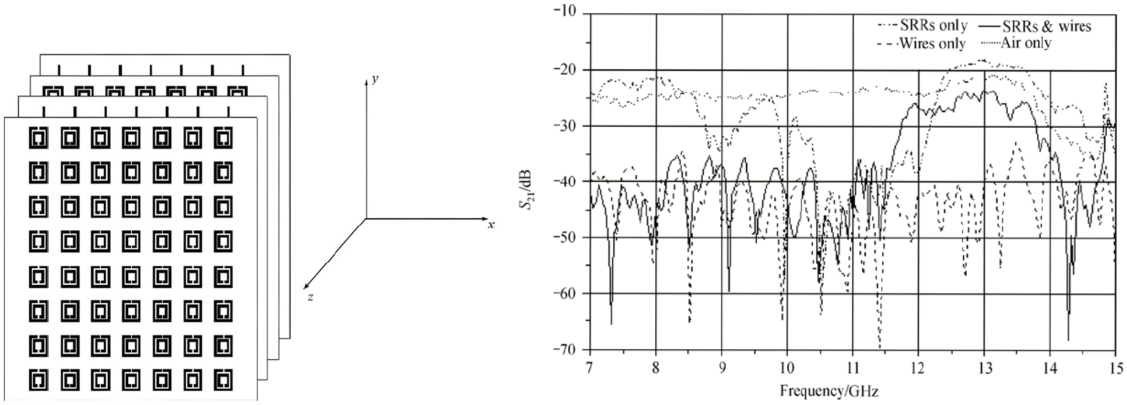

(a) (b)

Figure 21. Setup and transmission measurement results of a DNG metamaterial [44]. (a) The setup consists of separate circuit boards containing SRR particles and wire elements. The incident electric field propagates along the x-axis, and $\boldsymbol{E}$ is aligned along the y-axis. Measurements are made with the alternating SRR and wire circuit boards, SRR circuit boards only, wire circuit boards only, and no circuit boards. The angle of incidence is also varied. (b) The results for 0° incidence show reduced transmission in a frequency band for any of the configurations with one of the metamaterial circuit boards [44].

The research efforts presented in this section have generated many intriguing results, however, they differ from the experiments conducted in this thesis for several reasons. The experiments performed in [40] and [33] are performed in a guided-wave environment. The measurements in [44] include free-space measurements, but their analysis is limited to just beam shifting. All three papers focus on transmission results and do not look at reflection. The stripline measurement approach utilized in this research effort allows both transmission and reflection to measured. These dispersive results can be used to extract constituent parameters of a bulk sample in the waveguide using the procedures discussed in Section 2.3.3.

2.5 Achieving Frequency Adaptability

Many different methods for implementing frequency adaptability in metamaterial structures have been proposed recently, focusing mostly on affecting the resonant frequency of the particle. The particle is usually an SRR with inductance L and capacitance C. The particle's resonant angular frequency is given in the microwave frequency regime by [13]

$$\omega_0 = \frac{1}{\sqrt{LC}}. \tag{24}$$

The capacitance and inductance of an SRR is dependent on the material it is made of as well as its dimension and shape. For an SRR made of a PEC material, L and C can be approximated using [45]

$$\begin{aligned} L &\approx \mu_0 \frac{\ell}{4} \ln\left(\frac{8l}{w+h}\right), && \text{(25a)} \\ C &\approx \epsilon_0 \frac{wh}{\delta}, && \text{(25b)} \end{aligned}$$

where, h is the thickness of the SRR, l is the length of the SRR, and w and δ are shown in Figure 22. Note the use of Equation (25b) assumes the capacitance of the gap can be approximated with the model for a parallel-plate capacitor. While the assumption may not be valid in all scenarios, Equation (25b) can be used for illustrative purposes.

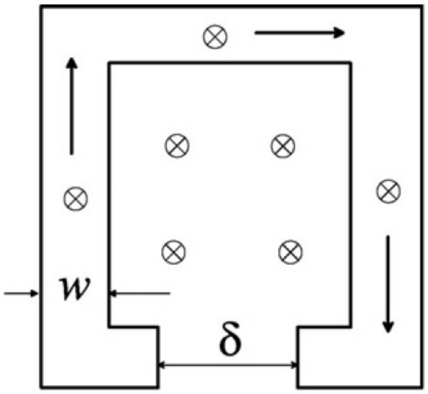

Figure 22. Dimensions of an SRR particle. The thickness of the particle (into the page) is denoted as h; while the length of the SRR is denoted as l [45].

Current attempts to introduce frequency adaptability into SRR structures focus on manipulating the inductance or capacitance of the circuit to change the resonant frequency of the structure. Gollub *et al.* in [10] show that the effective inductance of the structure can be influenced by incorporating a magnetic layer in the material. Conversely, Gil *et al.* in [9] and Shadrivov *et al.* in [39] propose structures that make use of a varactor diode to control the capacitance of the structure. Shadrivov *et al.* in [38] propose similar structures that make use of changes in field intensity to enhance or suppress wave transmission. Huang *et al.* further the analysis of varactor-loaded metamaterials in [17] by examining the second and third order susceptibilities of the structure. Han *et al.* in [12] propose the use of semiconductor materials for the SRR allowing control of the resonant frequency through the application of an external magnetostatic field. A tunable metamaterial structure that utilizes an externally mounted MEMS switch to change the capacitance of the SRR is proposed by Hand and Cummer in [13]. Lunet *et al.* propose a unique FSS that utilized the tunable permittivity of a thin film to adjust the resonance of the material [24]. Nicholson and Ghorbani present a series SRR design with tunable capacitances to adjust resonance in [28]. The following sections will look at these proposals in more detail.

2.5.1 Magnetic Circuits.

The structures proposed by Gollub *et al.* combine the dispersive properties of the metamaterial structure with the dispersive properties of a magnetic layer. The basic structure is shown in Figure 23. The additional magnetic layer introduces an approximately perpendicular magnetic field in the gap at resonance [10].

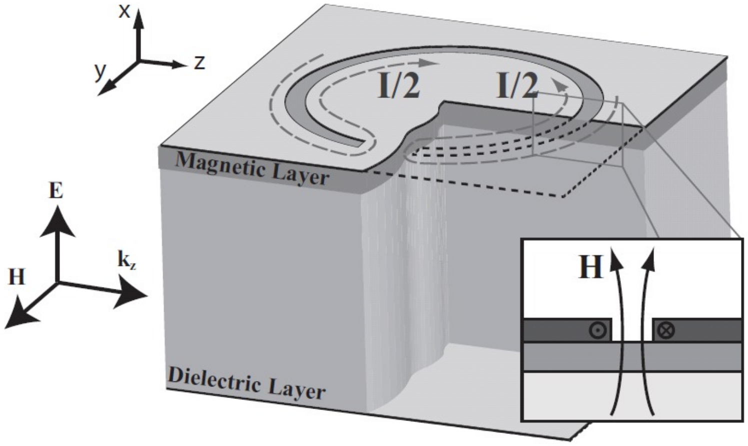

Figure 23. Unit cell structure that utilizes a magnetic layer. Inset: A magnetic field that is approximately perpendicular is produced in the gap of the magnetic material at resonance [10].

The magnetic field changes the equivalent inductance of the structure. The new inductance L is given by [10]

$$L = \mu_0 \left(\frac{\mu_r(\omega)}{\mu_r(\omega)(1-q)+q} \right) g_{geom}, \tag{26}$$

where μ_r is the relative permeability of the magnetic material and q is the volume fraction of the frequency dependent magnetic material. The new resonance frequency

(ω_0') is found by substituting the new expression for inductance from Equation (26) into Equation (24) yielding [10]

$$\omega_0' = \frac{1}{\sqrt{\frac{\mu_r(\omega_0')}{\mu_r(\omega_0')(1-q)+q}}}\omega_0. \tag{27}$$

Gollub *et al.* show that by tuning the biasing field of the magnetic material, the resonance frequency of the metamaterial structure can be adjusted. They validated their findings through simulations using the Ansoft HFSS$^{\mathrm{TM}}$ finite element solver. The results of the analysis for bias values: 0 kilogauss (kG), 1 kG, 2 kG, and 3 kG are shown in Figure 24. The resonance bands are characterized by the drops in transmission. From Figure 24, it is clear that the resonance frequencies are dependent on the bias values.

While there are non-metamaterial structures that make use of magnetic materials to make tunable microwave devices, the proposed structure has a larger range of material properties and can function in a larger resonance band. Furthermore, the combined effects of the metamaterial structure and magnetic layer would require less material than a similar device that did not implement a metamaterial structure [10].

2.5.2 Varactor-Loaded Circuits.

Gil *et al.* propose the use of a varactor-loaded SRR in the design of a tunable notch filter. Their proposed design utilizes a square-shaped geometry to increase the coupling between the line and the ring. Their design incorporates a varactor diode between the inner and outer rings as shown in Figure 25. The structure's overall effective capacitance is dominated by the varactor's capacitance. By using a tunable diode, the resonant frequency of the structure can be changed to block transmission at certain frequencies [9].

By adjusting the bias applied to the structure, the resonance shifts in frequency.

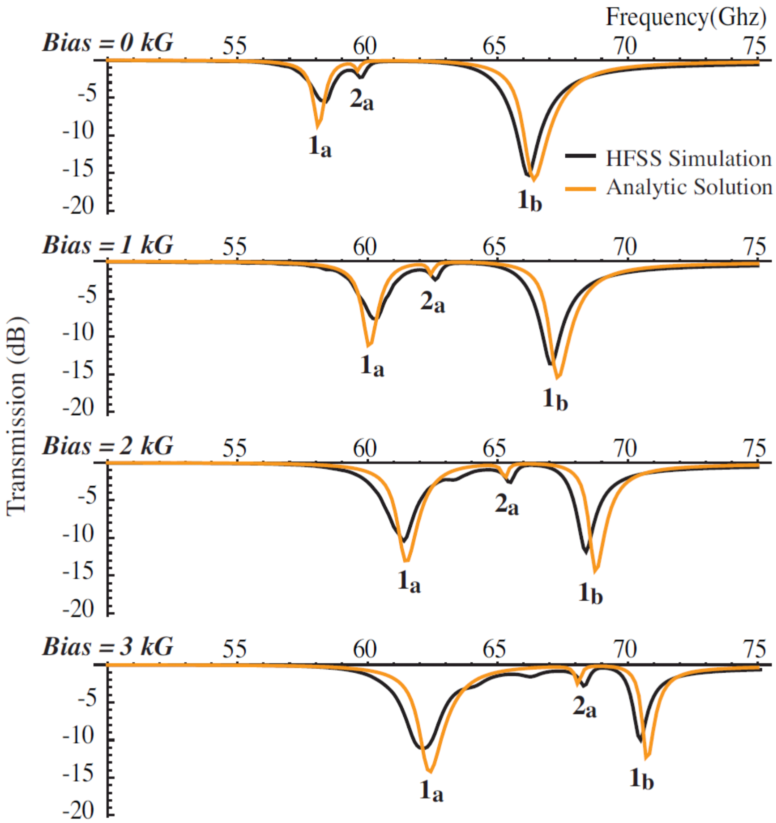

Figure 24. Results from the analysis of the SRR structure with magnetic layer. The transmission results are shown for four different bias values: 0 kilogauss (kG), 1 kG, 2 kG, and 3 kG. The resonant frequencies are the drops in transmission. Note that the location of the resonance frequencies are dependent on the bias values [10].

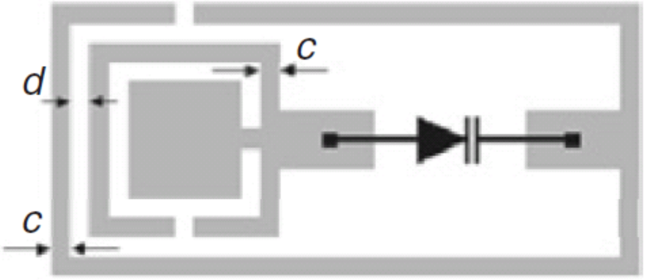

Figure 25. SRR structure proposed by Gil *et al.* A varactor diode is placed between the inner and outer rings [9].

Figure 26 shows the results of measurements of the structure's transmission coefficient under different bias conditions. The physical device consists of a 50 Ω microstrip line with two of the unit cell structures shown in Figure 25 placed on each side of the line. The bias voltage changes the capacitance of the varactor diode circuit. This has a dominant effect on the overall effective capacitance of the circuit. The changes in resonant frequency with respect to changes in bias voltage show the ability to tune the proposed structure to different frequencies [9].

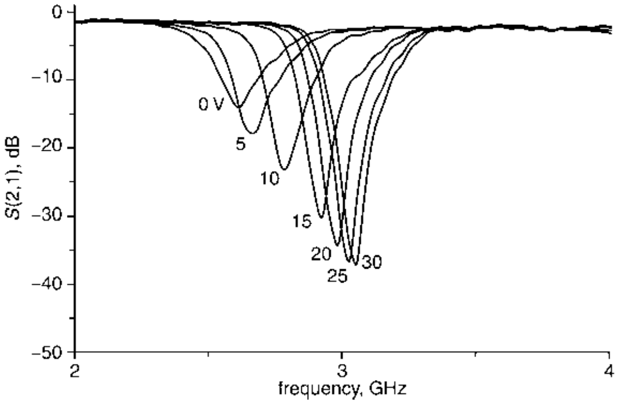

Figure 26. Measured transmission coefficients for the varactor-loaded SRR structure proposed by Gil *et al.* The different curves show the results at the different bias conditions used. Note that the resonant frequency depends on the bias voltage that controls the capacitance of the varactor diode circuit [9].

Shadrivov *et al.* also propose a structure that implements a varactor diode to control the capacitance of the circuit, however their design differs in the placement of the diode. Gil *et al.* placed the varactor between the outer rings, while Shadrivov *et al.* propose placing the varactor diode in series with the distributed capacitance of the outer ring. This is achieved by adding an additional gap in the outer ring and placing the varactor across it. They show that this structure also allows for tunability of the transmission response by changing the bias voltage. For example, they show that with a negative bias voltage of 10 V, the resonant frequency is 2.9 GHz. With a positive bias of 1 V, the resonant frequency is 2.27 GHz [39].

Shadrivov *et al.* also show that the bias of the diode can be controlled by incident electromagnetic field strength [39]. These results demonstrate the structure's ability to respond dynamically to an incident electromagnetic wave. In [38], Shadriivov *et al.* extend the study of this structure with experimental waveguide measurements. Their proposed design is applied to the metamaterial array shown in Figure 27.

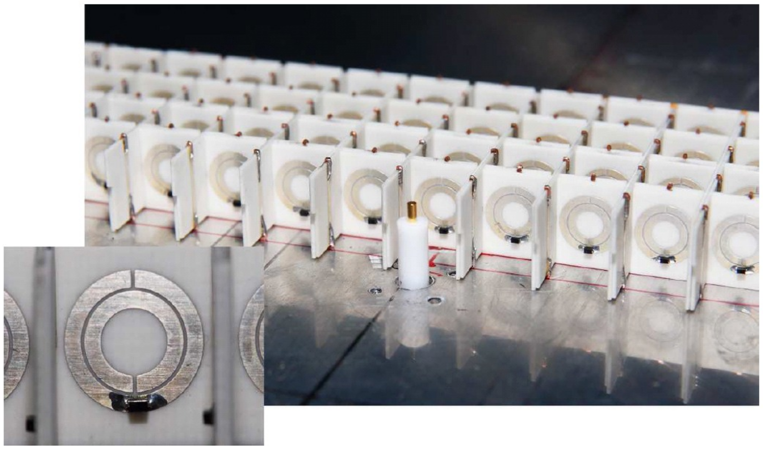

Figure 27. An array of SRR metamaterial structures that contain varactor diodes to allow for frequency adaptability. Inset: A closeup of an individual cell. The varactor diode is the small structure attached at the bottom of the outer ring [38].

The results from waveguide measurements of this varactor loaded structure are shown in Figure 28. The source power influences the bias of the diode, in turn, changing the capacitance of the structure and ultimately, the resonance frequency of the metamaterial. The result is a structure that can adapt based on the power carried by the incident electromagnetic field [38].

Huang *et al.* furthered the analysis of varactor-loaded metamaterials in [17]. They confirmed that over a limited range of power, a varactor-loaded SRR can be described by its second and third order nonlinear susceptibilities. For their work, the design shown in Figure 29 is used.

First, CST MWS® is used to extract parameters used in their analytical models. Next, their theoretical results are generated to be compared to transmission line measurements of the fabricated structure. The results of the analytical model and measurements are shown in Figure 30. The results show a slight downward frequency

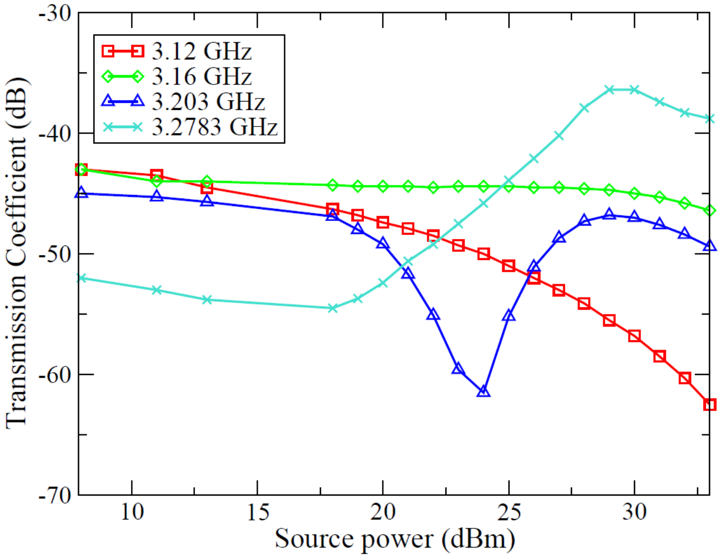

Figure 28. Waveguide measurement results for the design proposed by Shadrivov *et al.* The transmission coefficient as a function of source power is shown for four different frequencies [38].

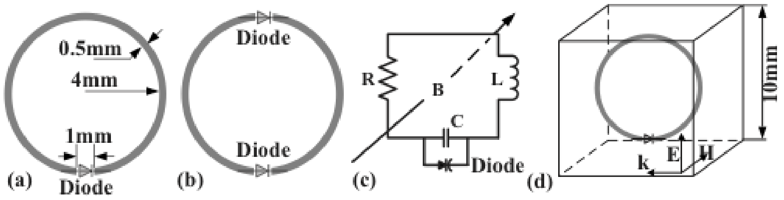

Figure 29. The varactor-loaded SRR structure analyzed by Huang *et al.* in [17]. (a) The single varactor-loaded SRR unit cell. (b) The double varactor-loaded SRR unit cell. (c) The equivalent circuit model for a single-gap unit cell. (d) Orientation of the unit cell.

shift with increasing power. More importantly, "the results point to the feasibility of nonlinear metamaterials formed by integrating inherently nonlinear crystals into the high-field regions of metamaterial elements" [17].

2.5.3 Semiconductor Split Ring Resonators with Magnetostatic Fields.

Han *et al.* also demonstrate frequency adaptability with a proposed design where the SRRs are made of a semiconductor material instead of metal. Their structure varies significantly in geometry from the previous designs. Concentric rings are re-

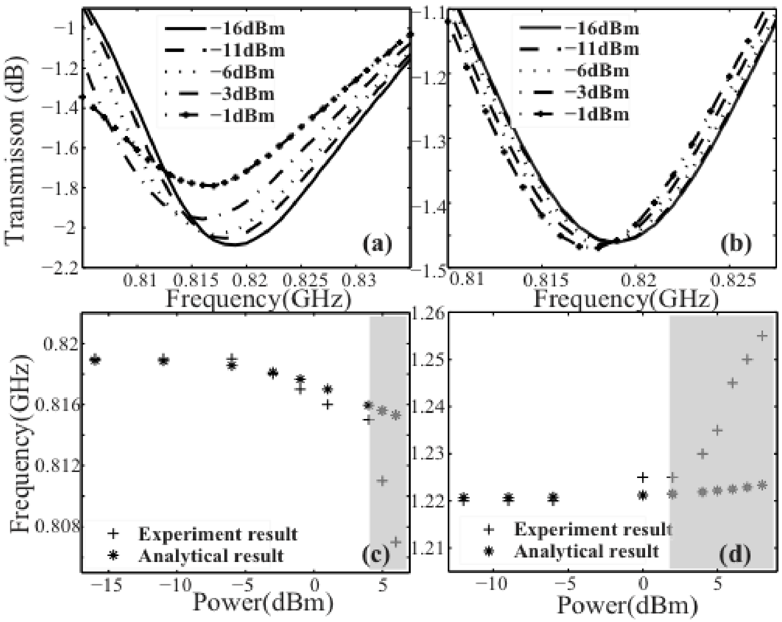

Figure 30. (a) Experimental and (b) theoretical transmission spectrum for a single varactor-loaded SRR. Comparison of analytical and experimental resonant frequency shifts for (c) single- and (d) double-gap unit cell models. The resonant frequency shifts slightly downward as the incident power level is increased.

placed by the structure shown in Figure 31.

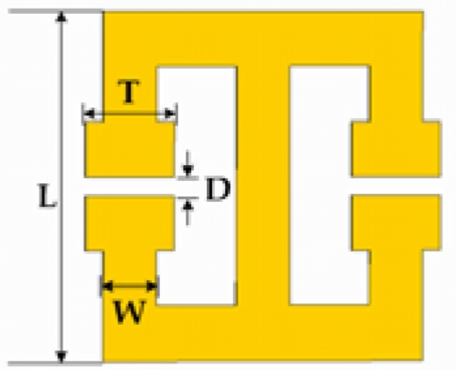

Figure 31. Geometry of a tunable metamaterial structure that contains SRRs made of semiconductor material [12].

The use of semiconductor material in the SRR changes the relative permittivity of the structure. The new relative permittivity (ϵ_r) is given by [12]

$$\epsilon_r(\omega) = \epsilon_\infty - \frac{\omega_p^2}{\omega^2 + j\gamma\omega}, \tag{28}$$

where ϵ_∞ is the high-frequency relative permittivity value, ω_p is the plasma frequency, and γ is the damping constant.

Han *et al.* propose the introduction of an external magnetostatic field to control the response of the structure. They present simulation results for various incident configurations. In the Faraday configuration, the magnetostatic field is aligned parallel to the wave vector of the incident field. In that case, the resonant frequency decreases as the amplitude of the magnetostatic field increases [12]. In the Voigt configuration, the magnetostatic field is aligned perpendicular to the wave vector of the incident wave. Two cases were analyzed in the Voigt configuration:

- when the magnetostatic field is perpendicular to the electric field the resonant frequency decreases with increases to the intensity of the magnetostatic field (similar to the Faraday configuration); and
- when the magnetostatic field is parallel to the electric field, the intensity of the magnetostatic field has no effect on the resonance of the structure [12].

2.5.4 SRRs with MEMS Switches.

Hand and Cummer propose a frequency adaptive metamaterial design with a MEMS switch in either a series or parallel configuration. Equivalent circuits for the series configuration are shown in Figure 32. When the switch is open, there is an additional capacitance (C_s) and resistance (R_s) due to the MEMS switch itself. When the switch is closed, C_s is shorted out. In this configuration, the MEMS switch allows the particle to resonate at two different resonant frequencies [13].

The parallel configuration has the equivalent circuit depicted in Figure 33. There is an additional capacitance (C_s) and resistance (R_s) due to the switch when it is open, but now they are in parallel with the capacitance of the SRR (C). When the

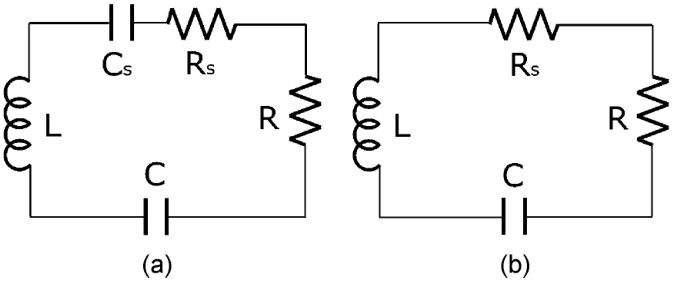

(a) (b)

Figure 32. Equivalent circuits for an SRR element with a MEMS switch in the series configuration. (a) The capacitance (C_s) and resistance (R_s) of the switch are in series with the capacitance of the SRR (C) when the switch is open. (b) When the switch is closed, C_s is removed from the circuit, but R_s remains [13].

switch is closed, C_s again is shorted. In this configuration, the open-state yields resonance at a certain frequency, while the closed-state has no resonance [13].

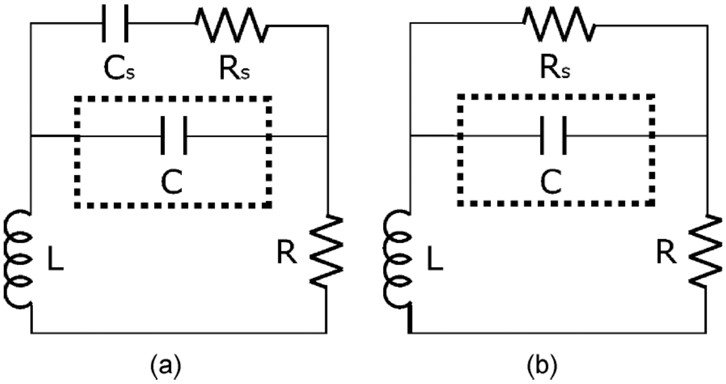

(a) (b)

Figure 33. Equivalent circuits for an SRR element with a MEMS switch in the parallel configuration. (a) The capacitance (C_s) and resistance (R_s) of the switch are in parallel with the capacitance of the SRR (C) when the switch is open. (b) When the switch is closed, C_s is removed from the circuit, but R_s remains [13].

Hand and Cummer measured both configurations in a waveguide. The results of the measurements with the switch in series are shown in Figure 34(c). As expected, the resonant frequency shifts when the MEMS switch changes states. In the closed state, the resonant frequency is approximately 2.04 GHz. The resonant frequency of the open state is over 2.9 GHz [13]. The results of the measurements with the switch in parallel are shown in Figure 34(d). In the open state, the resonant frequency is

2.26 GHz, however in the closed state there is no resonant behavior [13].

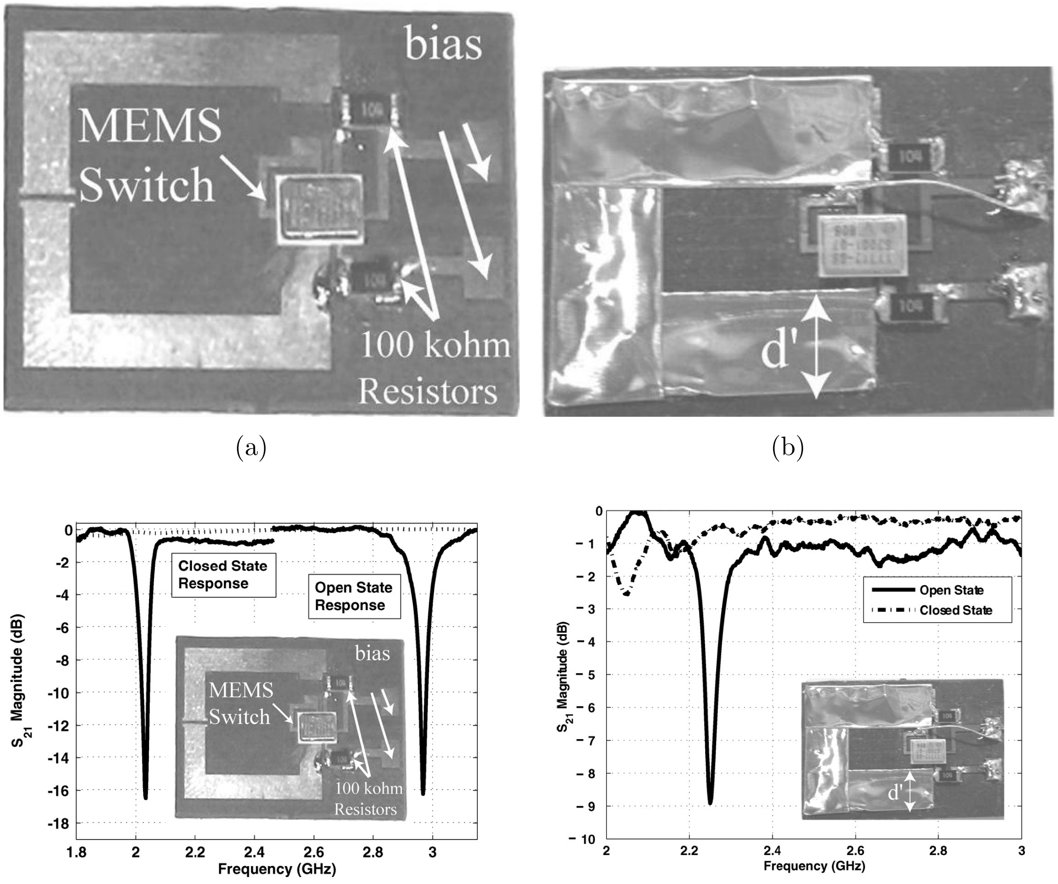

(a) (b)

(c) (d)

Figure 34. Results from measurements of the metamaterial structures implemented by Hand and Cummer. (a) Photograph of the series configuration circuit used. (b) Photograph of the parallel configuration circuit used. (c) For the series configuration, the open state shows the expected resonant behavior at over 2.9 GHz. The closed state lowers the resonant frequency down to approximately 2.04 GHz. (d) For the parallel configuration, the open state (solid line) shows the expected resonant behavior at approximately 2.26 GHz. The closed state (dash-dot line) shows no resonant behavior [13].

The parallel configuration also demonstrates the difficulty of scaling the frequency response outside of a small band. As the size of the ring decreases, the capacitance decreases as well. Below a certain size, the capacitance of the gap approaches the capacitance of the switch. Therefore, to make use of this design at higher frequencies, the switch capacitance must be reduced [13].

2.5.5 FSS with Thin Film for Permittivity Tunability.

Lunet *et al.* propose the unique FSS design shown in Figure 35. This structure differs greatly from the SRR type structures presented previously. When an electric field is applied between the inner and outer particles of the unit cell, via electrodes, the permittivity is shifted, thereby shifting the resonance of the device [24].

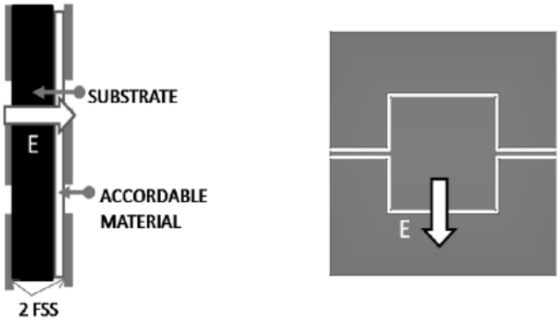

Figure 35. Geometry of a tunable FSS structure that has permittivity tunability based on the thin film "accordable" or tunable material [24].

Lunet *et al.* made simulations of the structure using Ansoft HFSS$^{\text{TM}}$ (FEM) and CST Microstripes (Transmission Line Matrix Method (TLM)). The results of the simulation are shown in Figure 36. As the design is anisotropic, the electric field is simulated parallel to the coplanar lines. When the electric field is perpendicular to the coplanar lines, the incident wave is totally reflected [24]. The simulations show that by varying the permittivity, the resonance frequency will shift. They go on to propose two tunable dielectrics for the "accordable" or tunable layer. It is noted that the permittivity and permeability are not negative on the same frequency band, therefore the structure is not a DNG material [24]. The material is still considered a metamaterial because the material has unusual properties with negative constituent parameters.

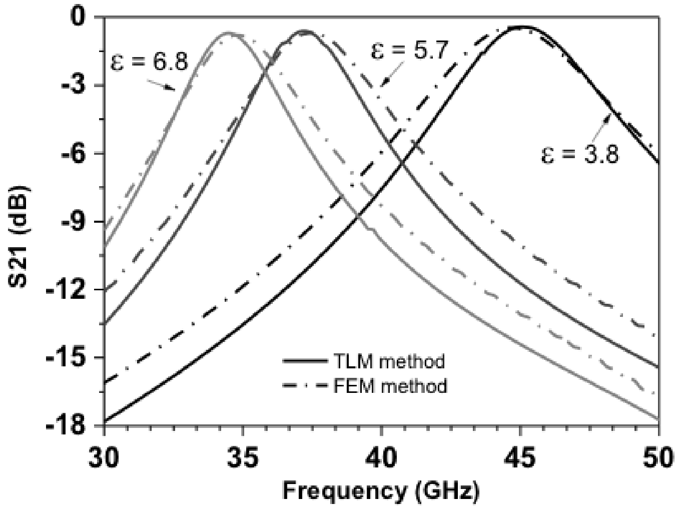

Figure 36. Simulation results show the tunability of the resonance based on the proposed permittivity. [24]

2.5.6 Series SRR Particles.

Nicholson and Ghorbani present a series SRR design with interdigital capacitors patterned on a barium strontium titanate thin film to achieve a tunable negative refractive index band [28]. The permittivity of barium strontium titanate can be varied by exposing the crystal to a static electric field, thereby changing the capacitance of the gap. The unit cell and series structure is shown in Figure 37.

The design is tuned such that magnetic resonance of the SRR is located in the region of negative permittivity of the wires. The design is simulated using Ansoft HFSS^{TM}. The simulation yields a negative refractive index band that is tuned from 8.7 GHz at 0.3 pF gap capacitance to 4.7 GHz at 1.0 pF gap capacitance [28]. The simulation results are shown in Figure 38.

2.5.7 Adaptive Metamaterial Literature Summary.

The research efforts on adaptive metamaterials presented in this chapter show a myriad of different ways to manipulate the resonant frequency of a metamate-

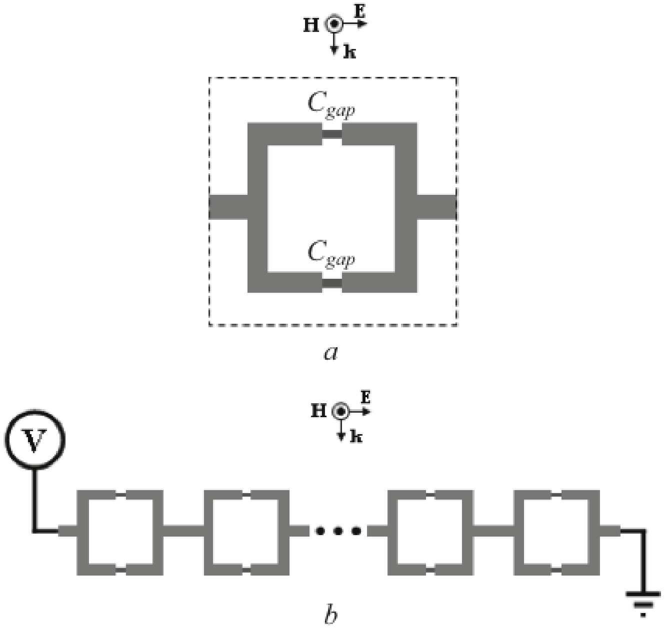

Figure 37. Geometry of the series SRR design, (a) unit cell and (b) static electric field configuration [28].

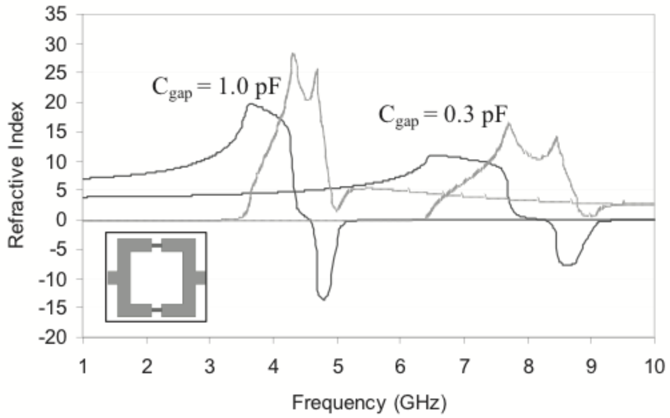

Figure 38. Simulation results for the series SRR design. The negative index of refraction bands are seen at 4.7 GHz for 1.0 pF and 8.7 GHz at 0.3 pF [28].

rial structure, however, these efforts differ from the approach taken in this research thrust. The metamaterial designs in [10] and [24] depend on the inclusion of tunable magnetic and dielectric material respectively to adjust the resonant frequency. In [9], the authors propose a design that employs a varactor diode to adjust the resonant frequency, however the varactor is large, leading to a perturbation of the pure SRR and complicating structure scalability for manufacturing. The authors in [39] and [17] present a similar design with alternate placements of the varactor. This diode is controlled by the incident electric field, automatically adjusting based on the incident power. Similar to the design examined in this thesis, the structures in [13] use a MEMS device to control the resonance of an SRR particle, but their MEMS device is a switch, not a variable capacitor. The authors of [28] present an alternate structure with series capacitors that are controlled with a static electric field, which is similar to the method used to control the capacitance of the metamaterial presented in this thesis, however, their capacitance changes are based on changes to the permittivity of the dielectric present.

The metamaterial design investigated in this thesis uses a MEMS variable capacitor that has six distinct states. It has a small footprint that is fabricated as part of the SRR element and is independent of the incident electromagnetic field.

III. Calculations and Computational Models

3.1 Chapter Overview

The purpose of this chapter is to describe efforts to model metamaterial structures using CST MWS®. As described in Section 2.3.1, CST MWS® employs the FIT. The models presented here are for the purposes of calculating the bandwidth of the AFIT adaptive metamaterial designs and calculating the expected response of the metamaterial structures when stimulated in a waveguide.

The use of the models presented in this chapter should provide insight into the physical phenomena that give metamaterial structures their unique properties. The models of adaptive metamaterial structures are a solid foundation on which to base future designs.

The results of this modeling effort show that introducing an additional variable capacitor in the gaps of the SRR particles is an effective method of changing the resonant frequency of the metamaterial device. The models also accurately predict the measurement results, showing that the computational techniques used in this thesis can greatly aid the systems engineering process by reducing the cost and length of the design cycle.

All simulations are completed on the AFIT low observable radar and electromagnetics network (LOREnet) machines. The computers are Dell Precision 690™ Workstations with one Quad 3.00 GHz Intel Xeon® processor and 32 GB of RAM. All workstations run Microsoft Windows® XP Professional x64.

3.2 AFIT Adaptive Metamaterial Models

AFIT-designed adaptive metamaterial structures are modeled using CST MWS®. Several different models are presented including:

1. a single cell structure with periodic boundary conditions,
2. a single cell structure with non-periodic boundary conditions,
3. a column of 4 unit cells placed in the waveguide used for measurements,
4. a column of 17 unit cells placed in the waveguide used for measurements.

For these models, the MEMS capacitor is modeled using a lumped network element. Modeling the actual MEMS capacitor would be difficult due to how small it is compared to the rest of the structure. The resulting computational mesh would be too large to solve on the computers available at AFIT. However, the lumped network element demonstrates the basic concept of operation and shows the movement of the resonant frequency relative to the change in capacitance. The mesh statistics for all models of the smaller AFIT metamaterial design can be found in Table 14 and solve times for the simulations can be found in Table 13. Both tables are in Appendix A.

3.2.1 One Cell Periodic Model.

The basic metamaterial structure investigated throughout this effort is shown in Figure 39(a). The structure consists of two SRR particles and two wire trace particles. The inner and outer SRRs are aligned such that they are concentric and their gaps are on opposite ends.

The SRR particles provide a negative permeability at resonance while the wire traces provide a negative permittivity at resonance. In the gaps of the SRR particles is a variable capacitor. The variable capacitor is fabricated as a MEMS device and is described in detail in [34]. For CST MWS® simulations the dimensions are altered to make the simulations more robust, simulating infinitely thin PEC surfaces unless otherwise noted.

The substrate is modeled as loss-free Quartz, a dielectric with $\epsilon_r = 3.75$. Original fabrications and modeling of this device used Sapphire as the dielectric, however Quartz is now used as the substrate material to avoid of the anisotropy of Sapphire.

For this simulation, periodic boundary conditions are assumed in the xy-plane. This creates the infinite surface shown in Figure 39(b). This set of boundary conditions is not representative of the waveguide scenario, however this allows bulk samples to be modeled without increasing the simulation domain. The z-boundaries are the Floquet ports or the source ports for problems with periodic boundary conditions. This is the source location and the measurement area for the S-parameter analysis. The z-plane to the left of the model corresponds to port 1, while the z-plane to the right of the model corresponds to port 2. The reference planes of the ports are adjusted to be flush with the face of the model closest to the respective port. The simulation is solved using the frequency domain solver for the frequency range 1 to 25 GHz.

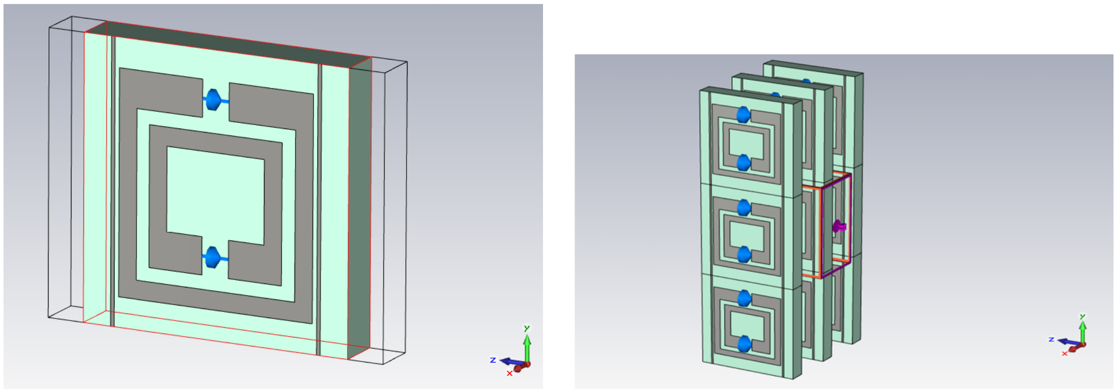

(a) (b)

Figure 39. CST MWS® model of a single cell variable capacitance SRR metamaterial structure with periodic boundary conditions. The blue objects are the lumped element capacitors. (a) The basic structure consists of two concentric SRR particles with variable capacitors over their gaps. There are also two wire traces that run along the sides of the outer SRR. (b) Periodic boundary conditions are used in the xy-plane.

The results of the S-parameter analysis for the model with the variable capacitors removed are shown in Figure 40. The magnitudes of simulated reflection (S_{11}) and transmission (S_{21}) cross near 11 GHz, 20 GHz and 23 GHz. These are the resonant frequencies.

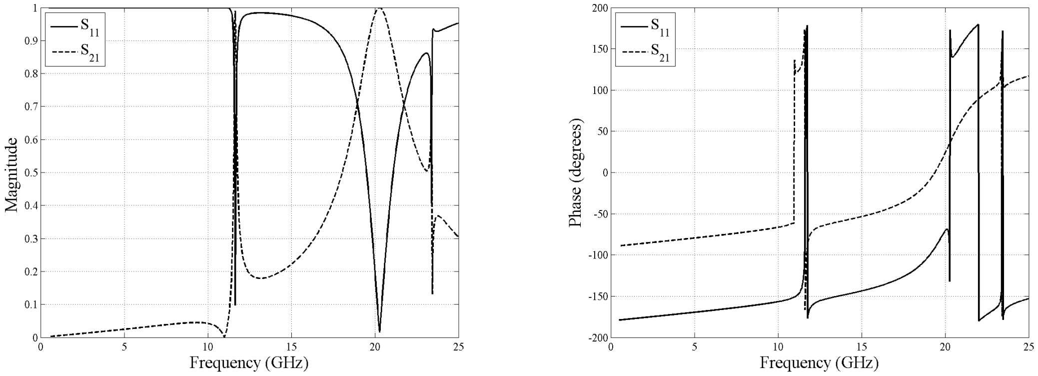

(a)

(b)

Figure 40. S-parameter results from the single cell periodic model with fixed gap capacitance. (a) The magnitudes of S_{11} and S_{21} show resonance points near 11, 20 and 23 GHz. (b) The phases of S_{11} and S_{21} show the largest changes around the resonance point.s

The presence of the cantilever beams on the SRR creates a new source of capacitance which modifies the resonance of the structure. With all the beams raised the cantilevers can be modeled as two capacitors in series, one with an air gap (C_1) and the other with a dielectric gap (C_2). The first capacitor will have a separation distance (d_1) equal to 2 μm, the ideal raised height of the cantilever beams. The second capacitor will have a separation distance (d_2) equal to the thickness of the dielectric layer, ideally 0.3 μm. The capacitance of the un-actuated beams is calculated by [22]

$$C_{total} = \frac{1}{\frac{1}{C_1} + \frac{1}{C_2}} = \frac{\epsilon_o \epsilon_r A}{\epsilon_r d_1 + d_2}, \tag{29}$$

where ϵ_r is the permittivity of the dielectric, silicon nitride, and A is the area of the capacitor. As the beams pull down they no longer behave as two capacitors in series but rather one capacitor with a separation equal to the thickness of the dielectric. The additional capacitances provided by the six different beam configurations are summarized in Table 4.

Table 4. Calculated additional capacitance values for MEMS cantilevers

State	Activated Beams	Capacitance (pF)
C0	None	0.195456
C1	300 μm	2.2282
C2	300 and 325 μm	4.26095
C3	300, 325, and 350 μm	6.29369
C4	300, 325, 350 and 375 μm	8.32644
C5	300, 325, 350, 375 and 400 μm	10.3592

With lumped element capacitors inserted in the SRR gaps, the structure is simulated with capacitance values shown in Table 4. The S-parameter analysis results are shown in Figure 41. The results show a deep resonance at 20 GHz that does not shift with increased capacitance. The results also show a thinner area of shifting resonance that begins around 5 GHz for capacitance equal to C0 and shifts to below 0.5 GHz for capacitance equal to C5. As the capacitance increases, the height of the resonance in the transmission data decreases. For capacitance values above C0, the resonance is barely perceptible in the reflection data. The strength of the resonance can be increased by increasing the depth of the simulation, i.e. the number of unit cells in the z direction, which is only one unit cell deep for these models.

Due to a fabrication issue, cuts needed to be made in the samples to enable the cantilever beams to actuate. Two types of cuts are made. One type cuts across the outer split ring, leaving the sets of cantilevers in the outer SRR gaps in the up position, while allowing the inner gap cantilevers to actuate. The other incision type cuts the inner cantilever control trace, leaving the sets of cantilevers in the inner SRR gaps in the up position, while allowing the outer gap cantilevers to actuate. For each model, both the structure with cuts across the outer split ring and the structure with cuts across the inner cantilever control trace are modeled.

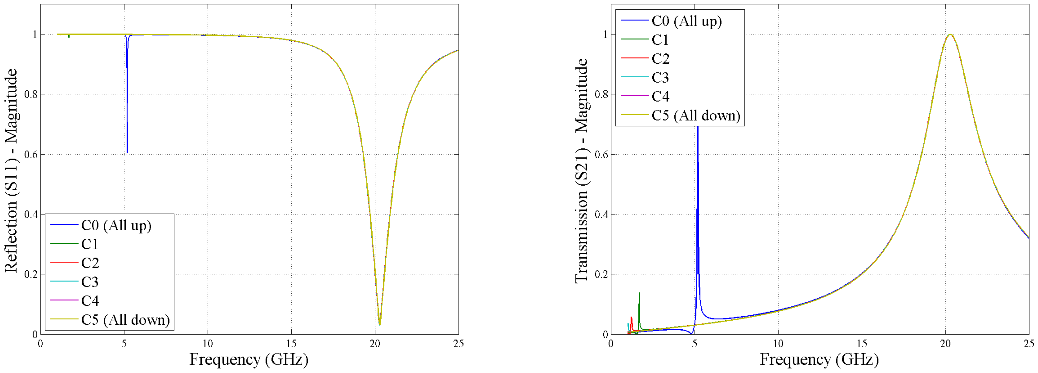

(a) (b)

Figure 41. ***S*-parameter results from the single cell periodic model with lumped element capacitors in the place of the MEMS capacitors in the SRR gaps. (a) Reflection and (b) transmission results show resonance shifting from 5 GHz for C0 to below 0.5 GHz for C5.**

3.2.1.1 Structure with Cuts Across Control Trace.

The structure with cuts across the inner cantilever control trace is modeled without any additional cuts as the thinner cantilever control traces are not included in the basic model. The inner capacitor is held constant at the C0 value shown in Table 4 while the outer capacitor is varied over the range of C0 to C5.

The results of the *S*-parameter analysis are shown in Figure 42. The results show a stationary resonance at 20 GHz and a deep but narrow resonance around 5 GHz for C0 that shifts to 7.5 GHz for C1 though C5. A smaller resonance is seen around 2 GHz for C1, 1.3 GHz for C2 and 1 GHz for C3. The resonance shifts below 0.5 for C4 and C5.

3.2.1.2 Structure with Cuts Across Outer SRR.

The structure with cuts across the outer SRR is modeled with two 5 μm gaps in the outer SRR as shown in Figure 43. In the fabricated structure, the cuts allow the cantilevers in the inner SRR gap to actuate, while leaving the cantilevers in the outer

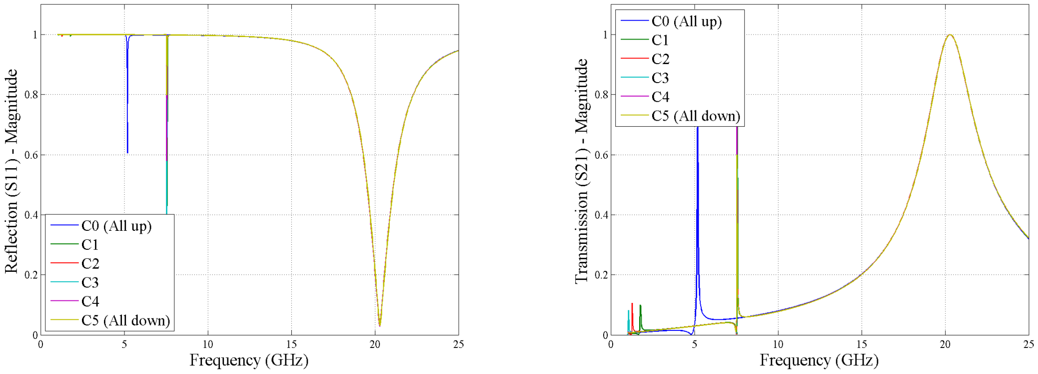

(a) (b)

Figure 42. ***S*-parameter results from the single cell periodic model with lumped element capacitors varying only the outer capacitor to simulated the structures with cuts across the inner cantilever control trace. (a) Reflection and (b) transmission results show a stationary resonance at 20 GHz and a deep but narrow resonance around 5 GHz for C0 that shifts to 7.5 GHz for C1 though C5. A smaller resonance is seen around 2 GHz for C1, 1.3 GHz for C2 and 1 GHz for C3. The resonance shifts below 0.5 for C4 and C5.**

SRR gap in the up position. For the models, the outer capacitor is held constant at the C0 value shown in Table 4 while the inner capacitor is varied over the range of C0 to C5.

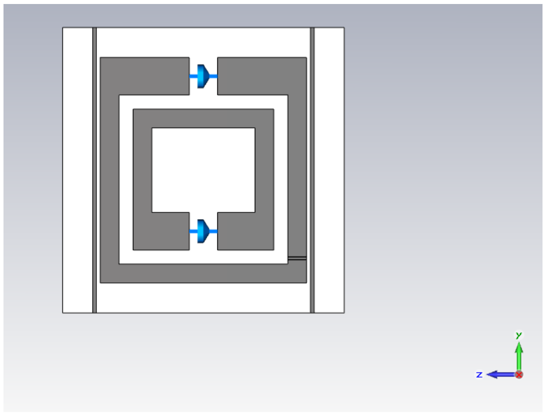

Figure 43. CST MWS® model of a single cell variable capacitance SRR metamaterial structure with cuts across the outer SRR with periodic boundary conditions.

The results of the *S*-parameter analysis are shown in Figure 44. The results show two stationary resonances around 13 and 22 GHz. There are also smaller resonances below 5 GHz. The variance at the 13 and 22 GHz resonances is due to mesh issues stemming from the size of the cuts in the outer SRR compared to the size of the other edges in the unit cell.

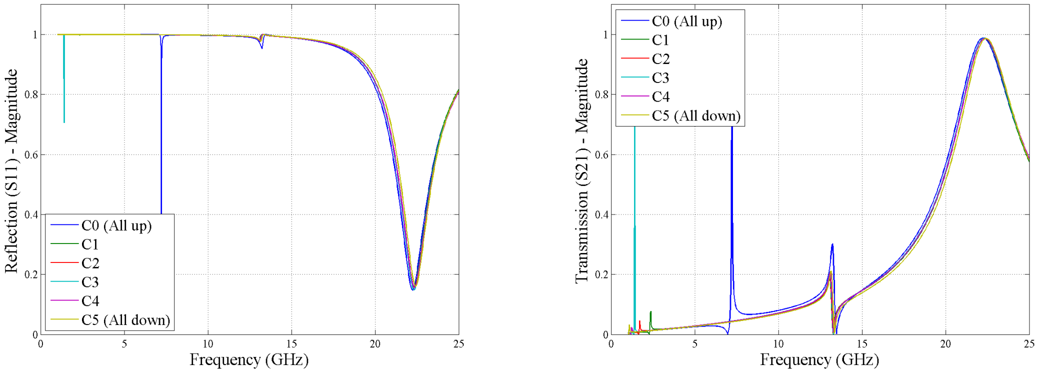

(a) (b)

Figure 44. S-parameter results from the single cell periodic model with cuts across outer SRR and lumped element capacitors varying only the inner capacitor. (a) Reflection and (b) transmission results show stationary resonances at 13 and 22 GHz and a shifting resonance below 5 GHz.

3.2.2 Single Cell Structure with Non-Periodic Boundary Conditions.

The next step in modeling the AFIT structure is the removal of the periodic boundary conditions, removing coupling between the adjacent SRR cells in the x-direction. Otherwise, the structures presented in this section are the same as previously described. For these models the boundary conditions in the x-direction are set to open while the boundary conditions in the y-direction are set to PEC. In this and the following models, the Floquet ports are replaced with waveguide ports. As in the previous models, the reference planes of the ports are set even with the faces of the structure. The additional space between the faces of the cell and the x-direction boundaries must be adjusted such that the ports capture all the energy at the resonance points and only a single mode is excited. It is determined that the results are obtained in the least amount of time when the width of the computational domain is about the width of the large SRR. The boundary conditions and spacing are summarized in Table 5.

Table 5. Non-periodic single cell adaptive AFIT metamaterial model boundary conditions and spacing.

Boundary Normal	Condition	Spacing from Edge (μm)
$\pm x$	Open	1000
$\pm y$	PEC	0
$\pm z$	Open (waveguide ports)	4000

As with all simulations of the metamaterial structures presented here, the problem is solved with the frequency domain solver. The first mode for this structure is TEM with $\boldsymbol{E}$ polarized in the y-direction. This field orientation is required to have the electric field interact with the vertical wire traces. First, the single cell structure is simulated with simultaneously varying inner and outer capacitor values. The S-parameter results are shown in Figure 45. The transmission results show a single resonance region shifting from 5 GHz at C0 to below 0.5 at C4. Similar resonance areas are seen in the reflection data. When compared to S-parameter data from the model with periodic boundary conditions (Figure 41), differences are noted. The transmission results remain low for entire frequency range for the single cell model, while the periodic model shows increased transmission peaking around 20 GHz. The reflection data for the single cell model shows a decrease with increased frequency, while periodic model shows high reflection data for the majority of the frequency range except around 20 GHz where the is a large null. The following two sections present the S-parameter analysis results for single cell non-periodic models of the metamaterial structures with cuts across the inner cantilever control traces and cuts across the outer split ring.

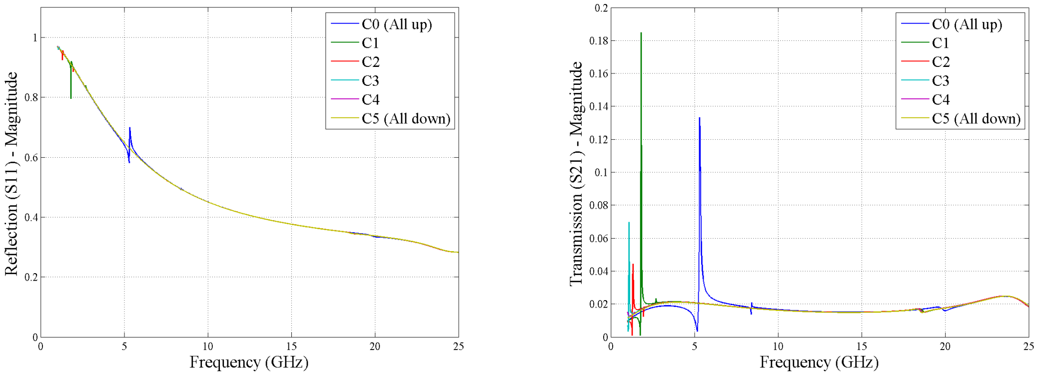

(a) (b)

Figure 45. S-parameter results from the single cell non-periodic model with lumped element capacitors in the place of the MEMS capacitors in the SRR gaps. Both the inner and outer capacitors are varied. (a) Reflection and (b) transmission results show resonance shifting from 5 GHz to 0.5 GHz.

3.2.2.1 Structure with Cuts Across Control Trace.

The simulation results of the metamaterial structure with cuts across the cantilever control trace are presented next. As previously modeled, no additional cuts are added to the basic model, as the cantilever control traces are not included in the model. The inner SRR capacitor is held constant at C0 to simulate the cantilevers all up, and the outer capacitor is varied from C0 through C5.

The S-parameter results are shown in Figure 46. The transmission shows a shifting resonance from 5 GHz at C0 to below 0.5 GHz at C5. There is also a resonance point at 8 GHz for C1 though C5 that is not evident at C0.

3.2.2.2 Structure with Cuts Across Outer SRR.

Next, the simulation results of the single cell non-periodic metamaterial structure with cuts across the outer SRR are presented. As with previous models, the cuts are modeled as 5 μm gaps in the outer SRR. The outer SRR capacitor is held constant at C0 to simulate all the cantilevers up, and the inner capacitor is varied from C0

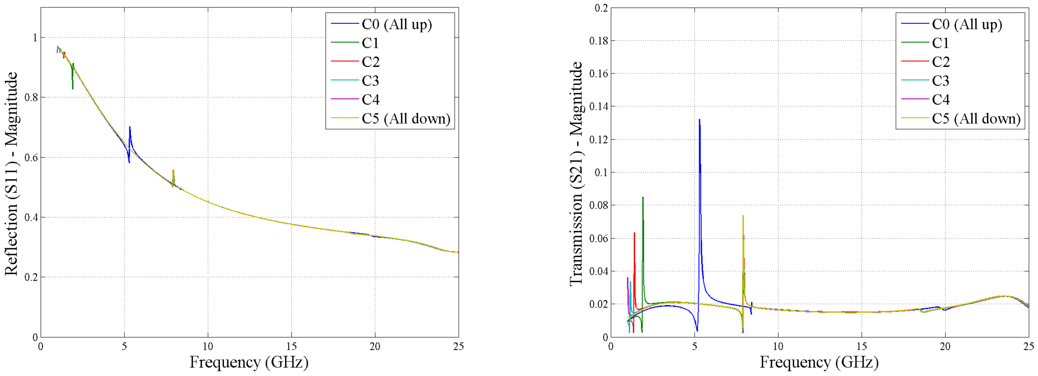

(a) (b)

Figure 46. ***S*-parameter results from the single cell non-periodic model with lumped element capacitors in the place of the MEMS capacitors in the SRR gaps. Only the outer capacitor is varied. (a) Reflection and (b) transmission results show resonance shifting from 5 GHz to 0.5 GHz.**

through C5.

The *S*-parameter analysis results are shown in Figure 47. The transmission shows resonance at 7.3 GHz for C0 that shifts to 0.5 GHz at C5. The reflection shows similar dispersive results. There also appears to be some resonant behavior around 13 and 20 GHz that is seen in the transmission but not in the reflection data.

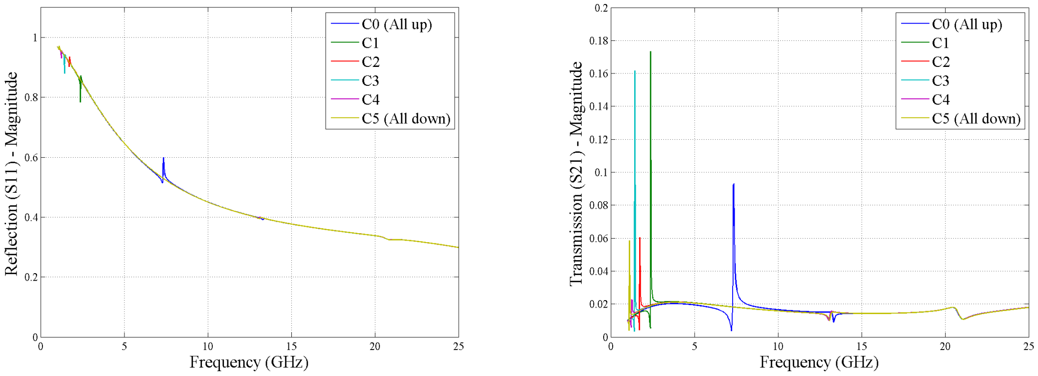

(a) (b)

Figure 47. ***S*-parameter results from the single cell non-periodic model with lumped element capacitors in the place of the MEMS capacitors in the SRR gaps and cuts across the outer SRR. Only the inner capacitor is varied (a) Reflection and (b) transmission results show resonance shifting from 7 GHz to 0.5 GHz.**

When compared to the S-parameter results from the models with cuts across the cantilever control trace several items are evident. The static resonance that is present at 8 GHz in the results from the model with cuts across the cantilever trace is not present for the model with cuts across the outer SRR. The two resonances at 13 and 20 GHz present in the model with cuts across the outer SRR are not present in the model with cuts across the cantilever control trace.

3.2.3 4-Cell Column in Waveguide.

After modeling the structures as an infinite plane of single cell entities and as a single cell, the models are refined to be more like the measurements performed for this thesis. For these devices, stripline measurements are determined to be the best approach. The stripline provides electric and magnetic field structures that interact with the devices to provide the desired unique properties. Specifically, the electric field must be oriented along the wire traces on either side of the concentric SRRs. The TEM mode created in the stripline provides the needed field structure as opposed to measurements utilizing rectangular waveguides where a TE mode is dominate.

3.2.3.1 18 GHz Stripline.

The AFIT adaptive metamaterial structures presented in previous sections are designed to be tested using a stripline waveguide designed for operation up to 18 GHz. To verify the operation of the stripline and to gain some insight into its frequency modes, a cross-sectional model of the stripline is constructed using CST MWS®. The model is shown in Figure 48. The physical dimensions of the model match the actual dimensions of the waveguide. All metal pieces are modeled as PEC, and all boundaries are set to open. The length of the stripline model is greater than three times the length of the longest sample to be measured in the physical stripline.

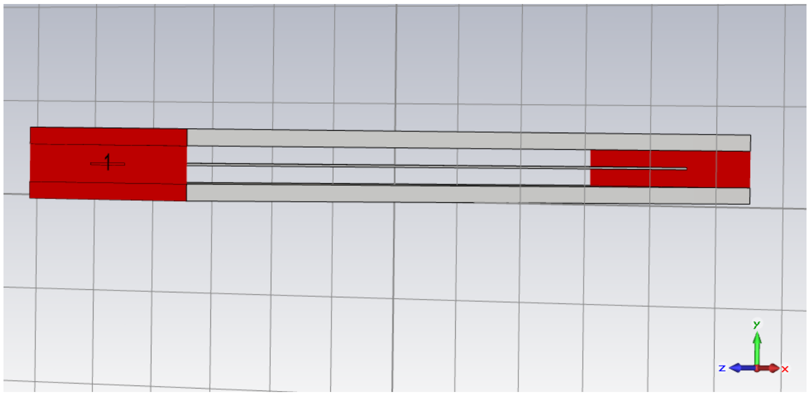

Figure 48. Model of the empty 18 GHz stripline. The cross sectional dimensions of the stripline structure match the physical dimensions of the actual stripline.

The results of the simulation are shown in Figure 49. Figures 49(a) and 49(b) show $\boldsymbol{E}$ and $\boldsymbol{H}$ at the longitudinal center of the waveguide respectively. As expected, $\boldsymbol{E}$ radiates in and out of the center conductor of the stripline while $\boldsymbol{H}$ circles around the center conductor. The magnitudes of the reflection and transmission from the simulation are shown in Figure 49(c). Ideally, S_{11} would be close to zero and S_{21} should be close to one for frequencies below the cutoff of the second propagating mode. The simulation results match the expected behavior.

Additionally, the simulation provides insight into the second mode of the stripline. The cutoff frequency of the second mode is about 18.5 GHz. This confirms that results above 18 GHz should be disregarded for both simulation and measurement. Next, 4-cell columns of the metamaterial structures are examined.

3.2.3.2 Structure with Cuts Across Control Trace.

In an effort to incrementally improve simulation and measurement results compatibility, single columns of the metamaterial structures are simulated inside the stripline, as the measurement would occur. To limit cell to cell interactions, a column of 4 cells is modeled in place of the 17-cell column to be measured. Despite the stripline field structure having the desired orientation, a design flaw in the sam-

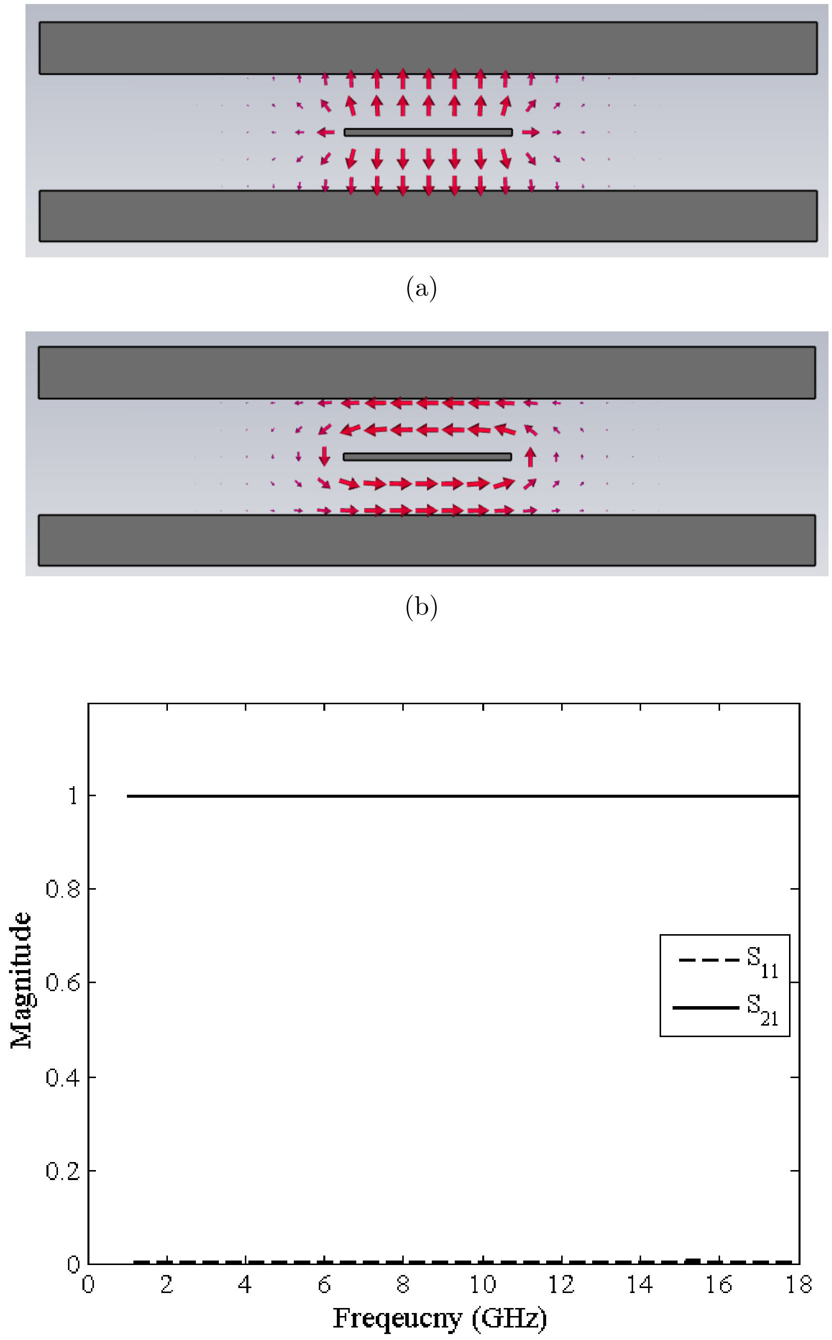

(a)

(b)

(c)

Figure 49. Results from the empty 18 GHz stripline simulation. (a) *E* at the center of the stripline radiates in and out of the center conductor as expected. (b) *H* at the center of the stripline circulates around the center conductor as expected. (c) Simulated transmission and reflection are one and zero respectively, as expected from an ideal empty waveguide.

ples required the cantilever control traces to run along the axis of propagation in the waveguide. To account for this difference, the unit cells are rotated such that the orientation in the simulated waveguide matches the orientation in the physical waveguide.

For the model, all boundaries are set to open, exactly as the empty stripline model. Also, the length of the stripline along the axis of propagation is set to three times the length of the metamaterial structure. This value is chosen to place the ports far enough away from the structure such that the near-field perturbations caused by the sample have enough distance to die out and not be detected as in the real measurements. For this model, no additional cuts are made as the cantilever control traces are not modeled. The number of port modes simulated is set to two for all simulations of the smaller AFIT adaptive metamaterial structures in the simulated waveguide. It is assumed that the physics of the structures is captured within these two modes and that higher order modes will have decayed before reaching the waveguide ports. The limited number of modes simulated also decreases simulation time drastically. The model is shown in Figure 50. The spacing of the structure simulated is not exactly as the measured samples are placed, with some tilt being observed in measurements. To simulate the un-actuated cantilevers, the inner capacitor is held constant and the outer capacitor is varied. The capacitance values simulated for this structure are calculated using Equation (29) and are summarized in Table 4.

The *S*-parameter analysis results for the structure are shown in Figure 51. At C0, resonance regions are seen around 5, 7, 8 and 14 GHz, with the strongest regions at 5 and 14 GHz. With the outer capacitor value increase to C1 through C5, the resonance area around 5 GHz is no longer seen. The resonance regions around 7 and 8 GHz shift down an equal amount while the resonance at 14 GHz shifts down slightly less. All of the resonance areas are dispersively the same for C1 through C5

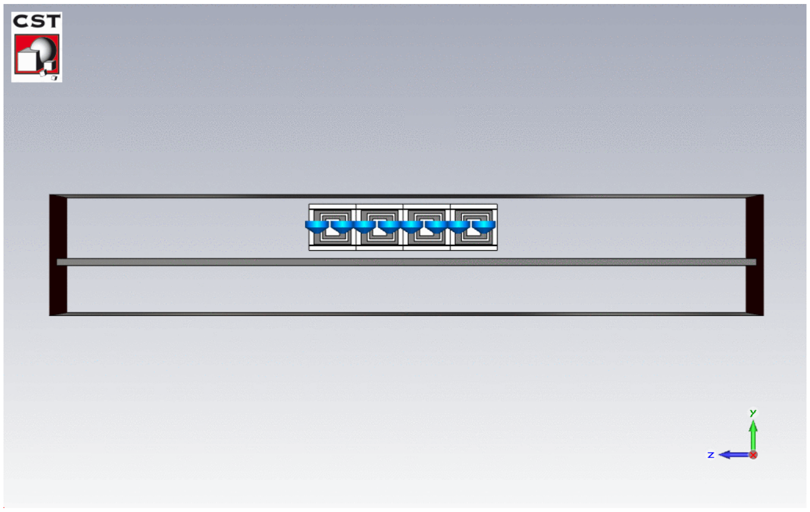

Figure 50. Model of a 4-Cell column of the AFIT metamaterial in the waveguide without additional cuts. To simulate the un-actuated inner cantilevers, the capacitor is set to C0 while the outer capacitor is varied.

values of capacitance.

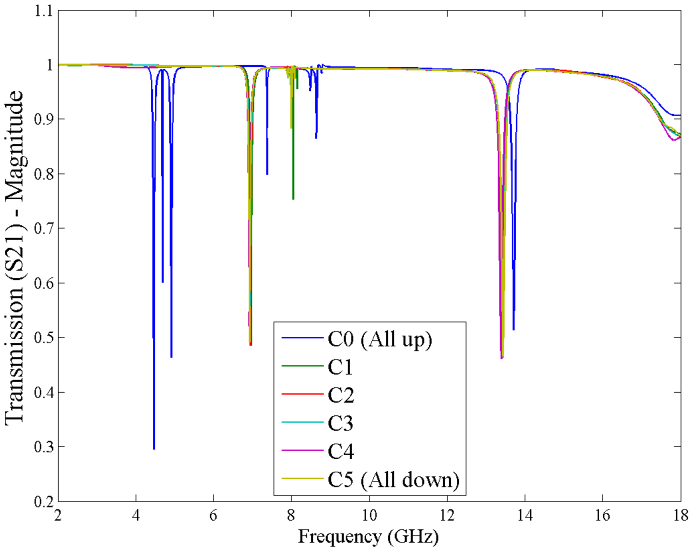

Figure 51. *S*-parameter analysis of a 4-cell column of the AFIT metamaterial modeled in waveguide changing only outer capacitor. Resonance areas are seen at 5, 7, 8 and 14 GHz for C0, however only resonances are seen at 7, 8 and 14 GHz for C1 through C5. The 7, 8 and 14 GHz shift down for C1 though C5.

The multiple resonance areas evident in the *S*-parameter results lead to an investigation of the fields in those regions. In particular, the dominant component of the electric field, the vertical component, is examined. For the investigation, only one capacitance value is needed to examine the fields. For the simulation, the inner capacitor is set to C0 and the outer capacitor is set to C5. The two deepest resonances are located at 6.9 and 13.5 GHz for this simulation. The fields are examined at five frequencies. The frequencies and their significance are summarized in Table 6.

Table 6. Frequencies examined for 4-Cell in waveguide model without additional cuts.

Frequency (GHz)	**Significance**
5.376	Below first resonance
6.944	First resonance
10.000	Between resonances
13.408	Second resonance
14.800	Above resonances

The vertical component of the electric field outside the resonance regions is shown in Figure 52 and the electric field within the resonance regions are shown in Figure 53, with the images on the left of the page being the fields tangent to a vertical plane in the center of the waveguide, bisecting the waveguide ports, and the images on the right of the page being the fields normal to a horizontal plane located half way between the bottom of the metamaterial structure and the top of the center conductor of the waveguide. The color scales of the images are on the same linear scale, with a minimum of -10000 V/m and a maximum of 10000 V/m. Field values below the minimum or above the maximum are displayed as the color of the minimum or maximum respectively.

As seen in Figures 52(a) and 52(b), the fields maintain their strength and are transmitted through the metamaterial structure for frequencies below the resonances. Figures 52(c) and 52(d) also show the fields at a frequency outside of the resonance bands, however this frequency is between the resonance areas. Again, most of the energy is transmitted though the structure, with just the beginnings of additional scattering. Figures 52(e) and 52(f) show the fields at a frequency above both res-

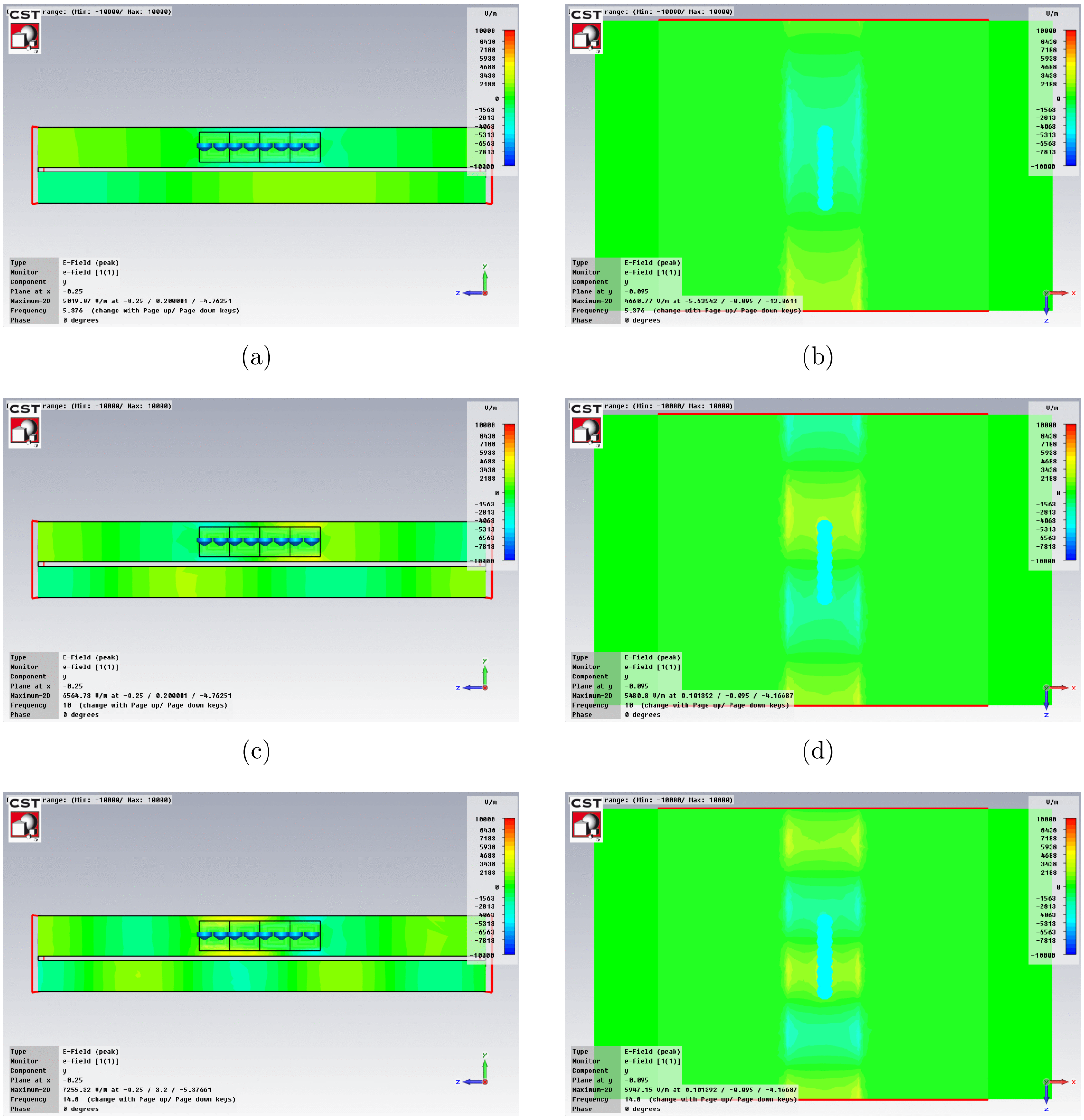

Type E-Field (peak)
Monitor e-field [1(1)]
Component y
Plane at x -0.25
Maximum-2D 5019.07 V/m at -0.25 / 0.200001 / -4.76251
Frequency 5.376 (change with Page up/ Page down keys)
Phase 0 degrees

(a)

Type E-Field (peak)
Monitor e-field [1(1)]
Component y
Plane at y -0.095
Maximum-2D 4660.77 V/m at -5.63542 / -0.095 / -13.0611
Frequency 5.376 (change with Page up/ Page down keys)
Phase 0 degrees

(b)

Type E-Field (peak)
Monitor e-field [1(1)]
Component y
Plane at x -0.25
Maximum-2D 6564.73 V/m at -0.25 / 0.200001 / -4.76251
Frequency 10 (change with Page up/ Page down keys)
Phase 0 degrees

(c)

Type E-Field (peak)
Monitor e-field [1(1)]
Component y
Plane at y -0.095
Maximum-2D 5480.8 V/m at 0.101392 / -0.095 / -4.16687
Frequency 10 (change with Page up/ Page down keys)
Phase 0 degrees

(d)

Type E-Field (peak)
Monitor e-field [1(1)]
Component y
Plane at x -0.25
Maximum-2D 7255.32 V/m at -0.25 / 3.2 / -5.37661
Frequency 14.8 (change with Page up/ Page down keys)
Phase 0 degrees

(e)

Type E-Field (peak)
Monitor e-field [1(1)]
Component y
Plane at y -0.095
Maximum-2D 5947.15 V/m at 0.101392 / -0.095 / -4.16687
Frequency 14.8 (change with Page up/ Page down keys)
Phase 0 degrees

(f)

Figure 52. Simulated field results outside of the resonance regions from the 4-cell AFIT metamaterial in waveguide without additional cuts. Fields tangent to a vertical plane in the center of the waveguide, bisecting the waveguide ports, are shown on the left with the images on the right of the page being the fields normal to a horizontal plane located half way between the bottom of the metamaterial structure and the top of the center conductor.

onance regions. While most of the energy is still transmitted though the sample, additional energy is scattered away from the waveguide ports, reducing the transmission only slightly.

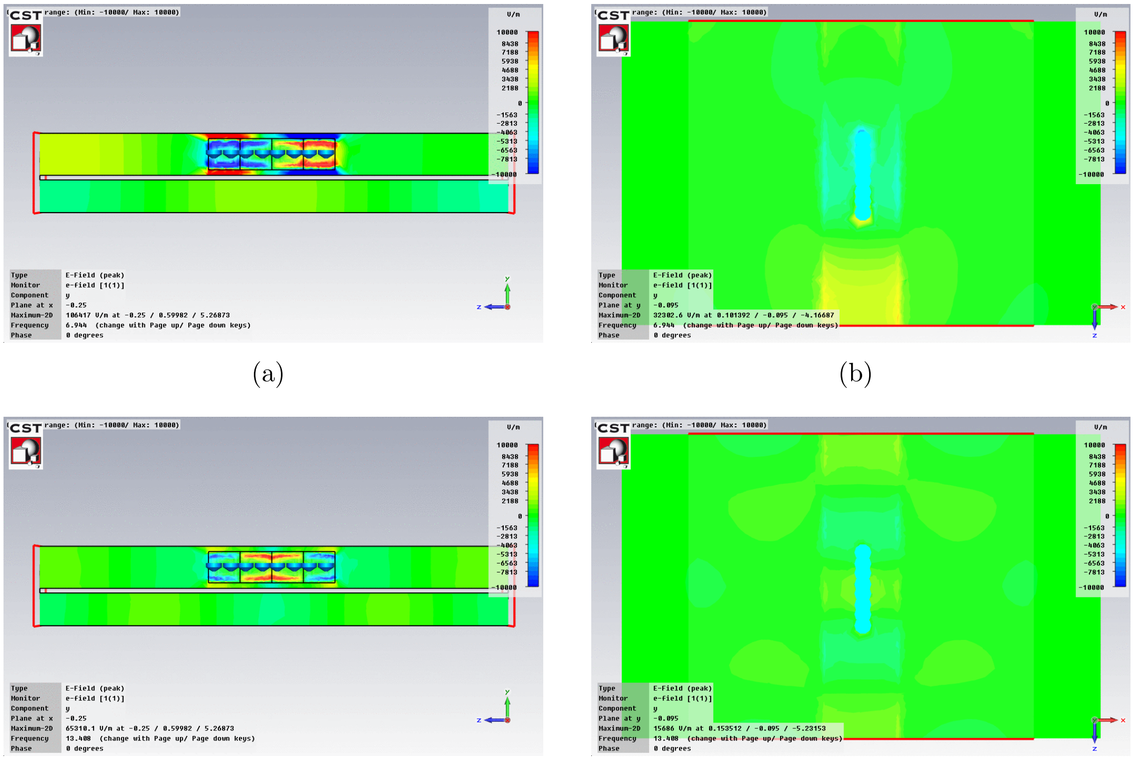

Type	E-Field (peak)
Monitor	e-field [1(1)]
Component	y
Plane at x	-0.25
Maximum-2D	106417 V/m at -0.25 / 0.59982 / 5.26873
Frequency	6.944 (change with Page up/ Page down keys)
Phase	0 degrees

(a)

Type	E-Field (peak)
Monitor	e-field [1(1)]
Component	y
Plane at y	-0.095
Maximum-2D	32302.6 V/m at 0.101392 / -0.095 / -4.16687
Frequency	6.944 (change with Page up/ Page down keys)
Phase	0 degrees

(b)

Type	E-Field (peak)
Monitor	e-field [1(1)]
Component	y
Plane at x	-0.25
Maximum-2D	65310.1 V/m at -0.25 / 0.59982 / 5.26873
Frequency	13.408 (change with Page up/ Page down keys)
Phase	0 degrees

(c)

Type	E-Field (peak)
Monitor	e-field [1(1)]
Component	y
Plane at y	-0.095
Maximum-2D	15686 V/m at 0.153512 / -0.095 / -5.23153
Frequency	13.408 (change with Page up/ Page down keys)
Phase	0 degrees

(d)

Figure 53. Simulated field results inside resonance regions from the 4-cell AFIT metamaterial in waveguide without additional cuts. Fields tangent to a vertical plane in the center of the waveguide, bisecting the waveguide ports, are shown on the left with the images on the right of the page being the fields normal to a horizontal plane located half way between the bottom of the metamaterial structure and the top of the center conductor.

Figures 53(a) and 53(b) show the vertical component of the electric field in the first resonance band. For the phase angle depicted, the field inside the cells is strong negatively for the first two cells and strong positively for the second half of the cells. The fields are very small in the remainder of the waveguide. The structure is scattering the field away from the waveguide ports at the resonance frequency, leading to a loss in transmission. The fields that are scattered are minimal compared to the fields that are transmitted through the sample outside of the resonance regions. Figures 53(c) and 53(d) show the fields at the second resonance frequency. The field structure at this frequency is similar to the first resonance frequency, however for the phase angle depicted, the fields inside the cells is strong negatively for the first and last cells in the structure and strong positively for the middle two cells in the structure. The horizontal cut particularly shows the creation of a different mode in the waveguide that is not collected by the waveguide ports because only two modes are recovered in the simulations. In measurements, the local field modes around the metamaterial structure would evanesce away before reaching the end of the waveguide because at this frequency region, only the principle TEM mode propagates. Also, the physical waveguide is much longer along the axis of propagation than the simulated waveguide. In summary, the coupling between cells in the structure at the resonance frequencies scatter the incident energy in a different mode than the propagating TEM mode, while outside of the resonance regions, the cells do not couple, allowing the waves to travel along the waveguide unimpeded. Both of these effects lead to high transmission outside of the resonance areas and lower transmission within the resonance regions.

3.2.3.3 Structure with Cuts Across Outer SRR.

A 4-cell column of the metamaterial structure with cuts across the outer SRR is also modeled. The cuts are modeled as 5 μm gaps in the outer split ring, the width of the physical cuts. Again, a design flaw in the sample required the cantilever control traces to run along the axis of propagation in the waveguide. To account for this difference, the unit cells are rotated such that the orientation in the simulated waveguide matches the orientation in the physical waveguide.

For the model, all boundaries are set to open, exactly as the empty stripline model and the model of the column in the waveguide without additional cuts. The model is shown on the left of Figure 54. A magnified view of the cuts across the outer SRR are shown on the right of Figure 54. To simulate the disabled cantilevers, the outer capacitor is held constant and the inner capacitor is varied. The capacitance values simulated for this structure are again calculated using Equation (29) and are summarized in Table 4.

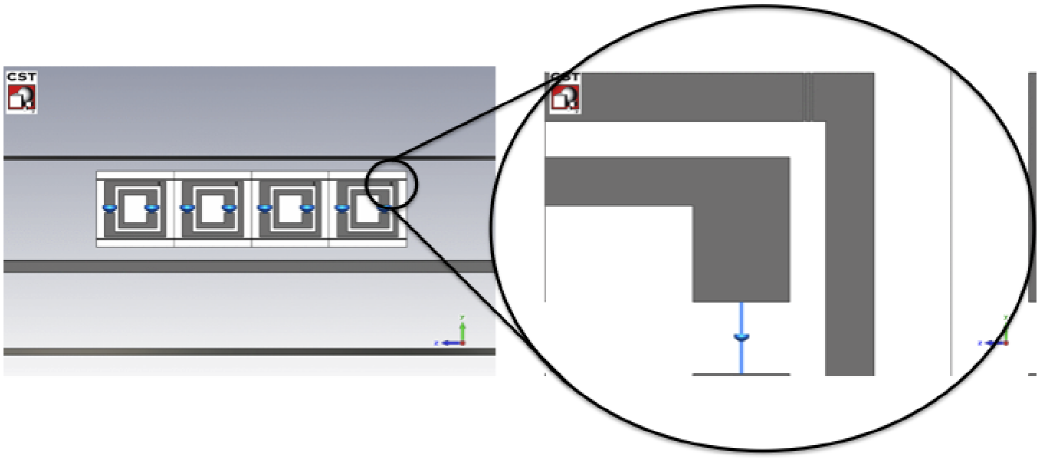

Figure 54. Model of a 4-Cell column of the AFIT metamaterial in the waveguide with cuts across the outer SRR. The 4-cell structure in the waveguide is shown on the left. The blue objects are the lumped element capacitors. On the right, the structure is magnified to show the cuts across the outer SRR in detail.

The S-parameter analysis results for the structure are shown in Figure 55. Multiple transmission nulls are observed at 6, 11, 13, 14, 16, and 17 GHz. The inclusion of the cuts across the outer SRR gives rise to additional resonance regions compared to the model without cuts. The resonance around 7 GHz begins as two nulls at C0, however for capacitance values of C1 through C5, only a single null is seen. The resonance around 11 GHz shifts down from the C0 location and remains constant for C1 though C5. The resonance region around 13 and 14 GHz follows the same behavior. The resonances around 16 and 17 GHz do not show consistent trending with increasing capacitance.

The multiple resonance regions observed in the S-parameter results lead to an investigation of the field in those regions. In particular, the dominant component of the electric field is again examined. For the investigation, only one capacitance value is needed to examine the fields as the resonance behavior is common across the

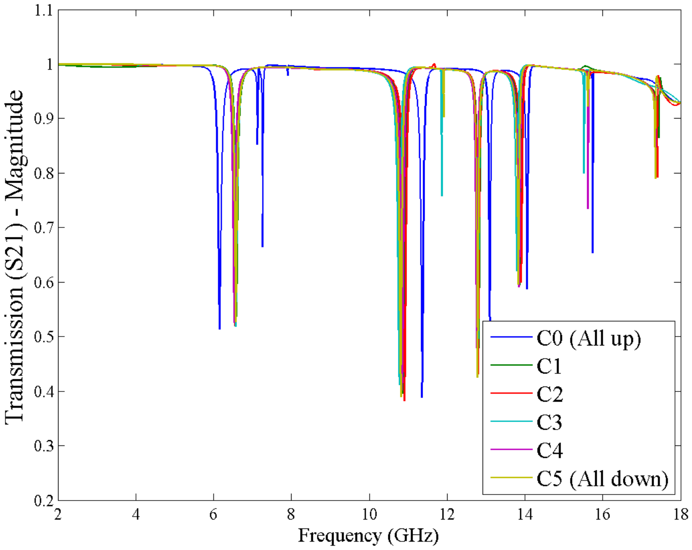

Figure 55. *S*-parameter analysis of a 4-cell column of the AFIT metamaterial modeled in waveguide including cuts across the outer split ring changing only inner capacitor. Multiple transmission nulls are observed at 6, 11, 13, 14, 16, and 17 GHz.

capacitor values simulated. For the simulation, the outer capacitor is set to C0 and the inner capacitor is set to C5. The fields are examined at eight frequencies. The frequencies and their significance are summarized in Table 7.

Table 7. Frequencies examined for 4-Cell in waveguide model with additional cuts.

Frequency (GHz)	**Significance**
4.349	Below first resonance
6.627	First resonance
9.296	Between resonances 1 and 2
10.792	Second resonance
12.407	Between resonances 2 and 3
12.781	Third resonance
15.603	Fourth resonance
17.354	Fifth resonance

The vertical component of the electric field for the frequencies selected outside resonance regions are shown in Figure 56, with the images on the left of the page being the fields tangent to a vertical plane in the center of the waveguide, bisecting the waveguide ports, and the images on the right of the page being the fields normal to a horizontal plane located half way between the bottom of the metamaterial structure and the top of the center conductor of the waveguide. The color scales of the images are on the same linear scale, with a minimum of -10000 V/m and a maximum of 10000 V/m. Field values below the minimum or above the maximum are displayed as the color of the minimum or maximum respectively. The vertical component of the electric field for the first three resonance frequencies is shown in Figure 57, while the vertical component of the electric field for the remaining two resonance frequencies is shown in Figure 58 .

As seen in Figures 56(a) and 56(b), below the resonance frequencies, the fields are transmitted through the sample to the waveguide port with very little scattering. Figures 56(c) and 56(d) show the fields between the first two resonance regions. The fields again maintain their strength through the sample, however more scattering is observed. Figures 56(e) and 56(f) show the fields between the second and third resonances. As seen for the fields between the first two resonances regions, the field maintains strength through the sample, scattering minimally.

Figures 57(a) and 57(b) show the vertical component of the electric field at the lowest resonance frequency. For the phase angle depicted, the field is strong negatively for the first two cells and strong positively for the second half of the cells, similar to the field structures in the first resonance of the model without additional cuts. The fields are very small in the remainder of the waveguide. At the resonance frequency the fields are interacting strongly with the metal particles in the cells. The fields show a decrease in strength as the wave moves away from the source port of the stripline.

Figures 57(c) and 57(d) depict the simulated fields within the second resonance area. For the phase angle depicted, the field structure is similar to previous resonant modes with the fields strongly negative in the first and last cells of the structure and

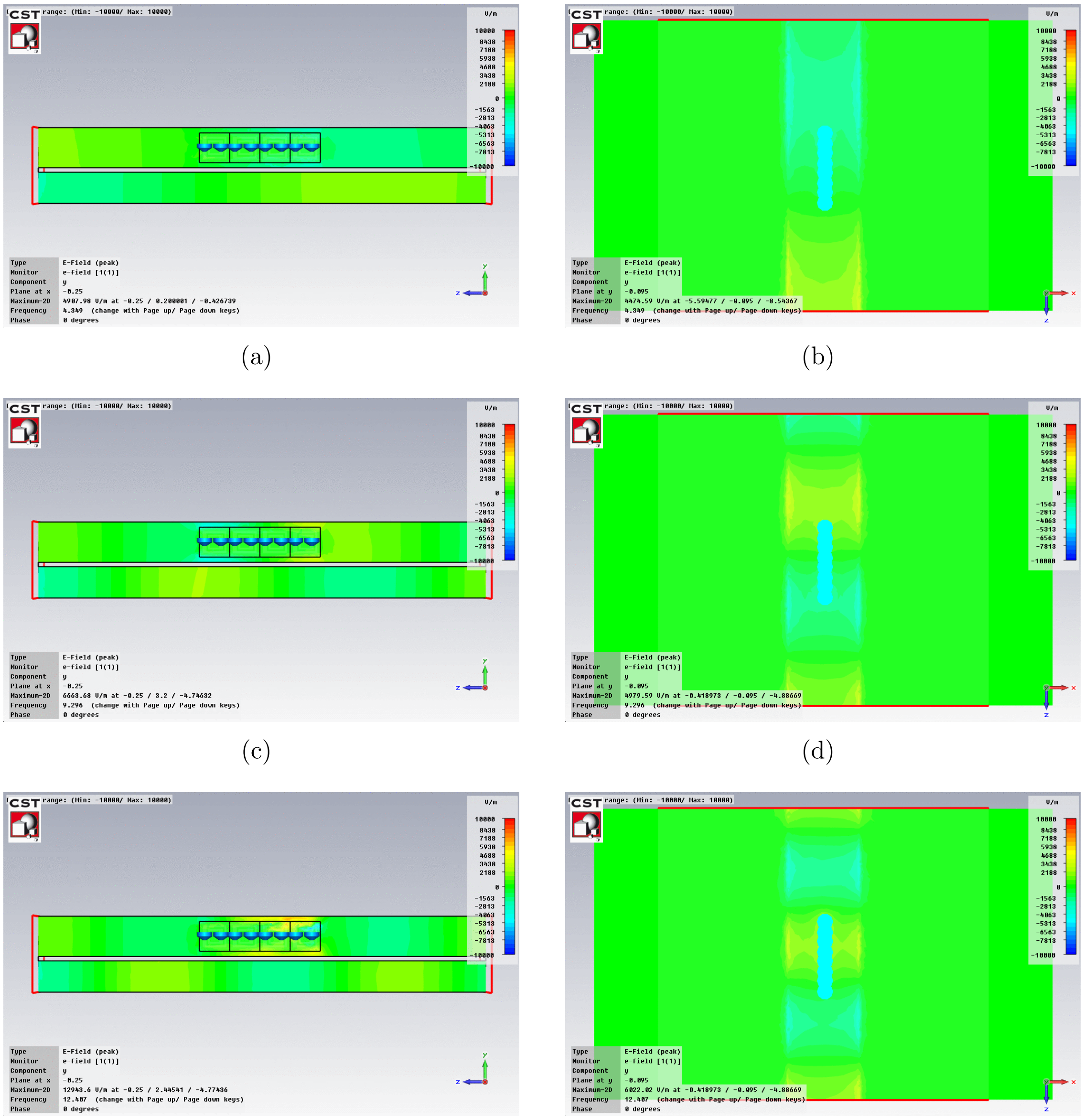

(a) (b)

(c) (d)

(e) (f)

Figure 56. Simulated field results outside the resonance regions from the 4-cell AFIT metamaterial in waveguide with additional cuts. Fields tangent to a vertical plane in the center of the waveguide, bisecting the waveguide ports, are shown on the left with the images on the right of the page being the fields normal to a horizontal plane located half way between the bottom of the metamaterial structure and the top of the center conductor.

strongly positive for the center two cells. There is also a decrease in field strength as the wave moves away from the source port of the waveguide. A higher order mode is created by field interactions with the sample. For this frequency regime, the higher

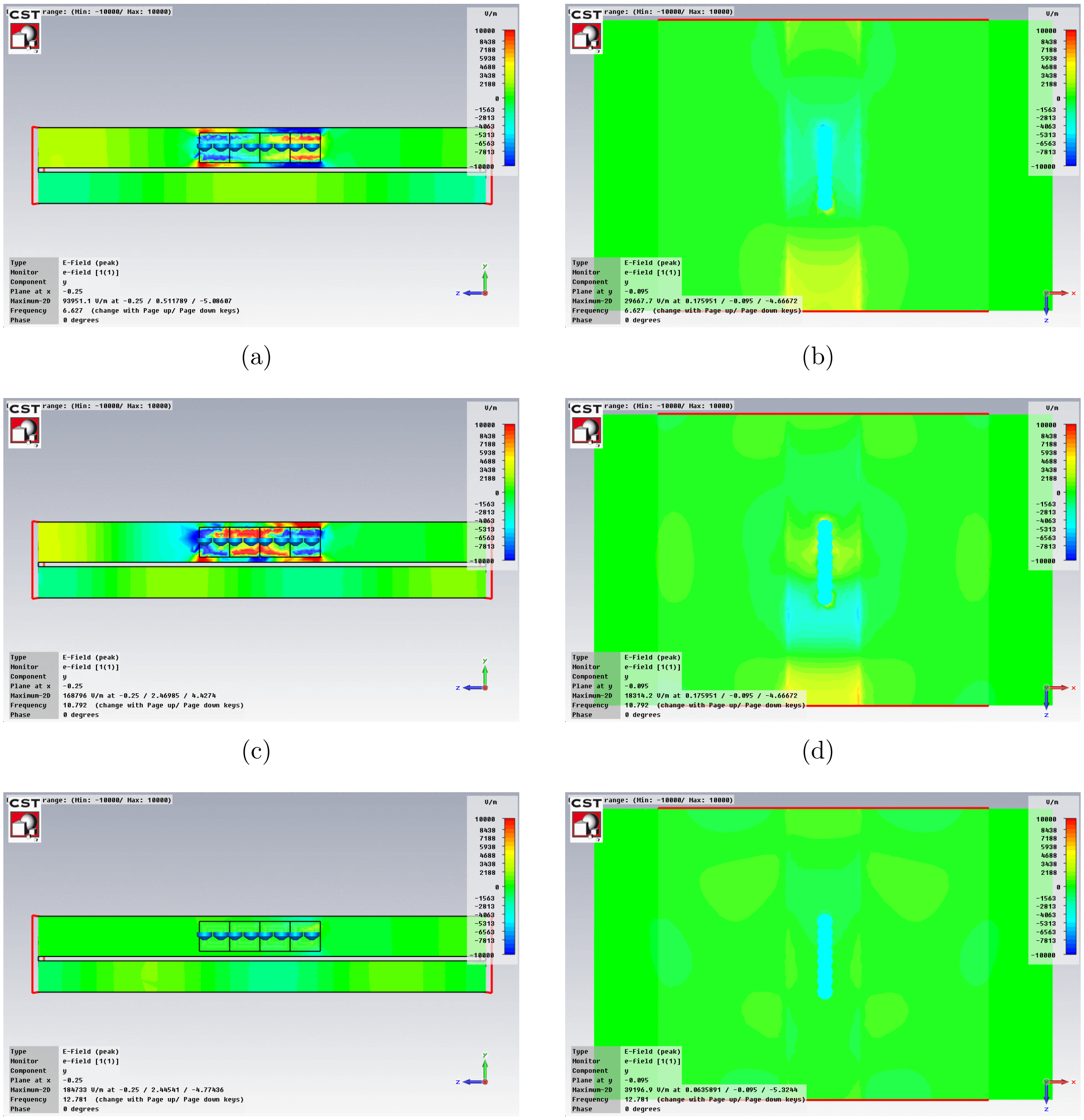

Type	E-Field (peak)
Monitor	e-field [1(1)]
Component	y
Plane at x	-0.25
Maximum-2D	93951.1 V/m at -0.25 / 0.511789 / -5.08607
Frequency	6.627 (change with Page up/ Page down keys)
Phase	0 degrees

(a)

Type	E-Field (peak)
Monitor	e-field [1(1)]
Component	y
Plane at y	-0.095
Maximum-2D	29667.7 V/m at 0.175951 / -0.095 / -4.66672
Frequency	6.627 (change with Page up/ Page down keys)
Phase	0 degrees

(b)

Type	E-Field (peak)
Monitor	e-field [1(1)]
Component	y
Plane at x	-0.25
Maximum-2D	168796 V/m at -0.25 / 2.46985 / 4.4274
Frequency	10.792 (change with Page up/ Page down keys)
Phase	0 degrees

(c)

Type	E-Field (peak)
Monitor	e-field [1(1)]
Component	y
Plane at y	-0.095
Maximum-2D	18314.2 V/m at 0.175951 / -0.095 / -4.66672
Frequency	10.792 (change with Page up/ Page down keys)
Phase	0 degrees

(d)

Type	E-Field (peak)
Monitor	e-field [1(1)]
Component	y
Plane at x	-0.25
Maximum-2D	184733 V/m at -0.25 / 2.44541 / -4.77436
Frequency	12.781 (change with Page up/ Page down keys)
Phase	0 degrees

(e)

Type	E-Field (peak)
Monitor	e-field [1(1)]
Component	y
Plane at y	-0.095
Maximum-2D	39196.9 V/m at 0.0635891 / -0.095 / -5.3244
Frequency	12.781 (change with Page up/ Page down keys)
Phase	0 degrees

(f)

Figure 57. Simulated field results from the 4-cell AFIT metamaterial in waveguide with additional cuts in the first second and third resonance regions. Fields tangent to a vertical plane in the center of the waveguide, bisecting the waveguide ports, are shown on the left with the images on the right of the page being the fields normal to a horizontal plane located half way between the bottom of the metamaterial structure and the top of the center conductor.

order mode does not propagate down the waveguide.

Figure 57(e) and 57(f) show the fields within the third resonance. For this phase angle depicted, the fields are near zero within the entire stripline, however a phase progression reveals strong fields across the outer SRR of the last cell in the column. This interaction excites multiple modes which are not captured by the waveguide ports, leading to a low transmission.

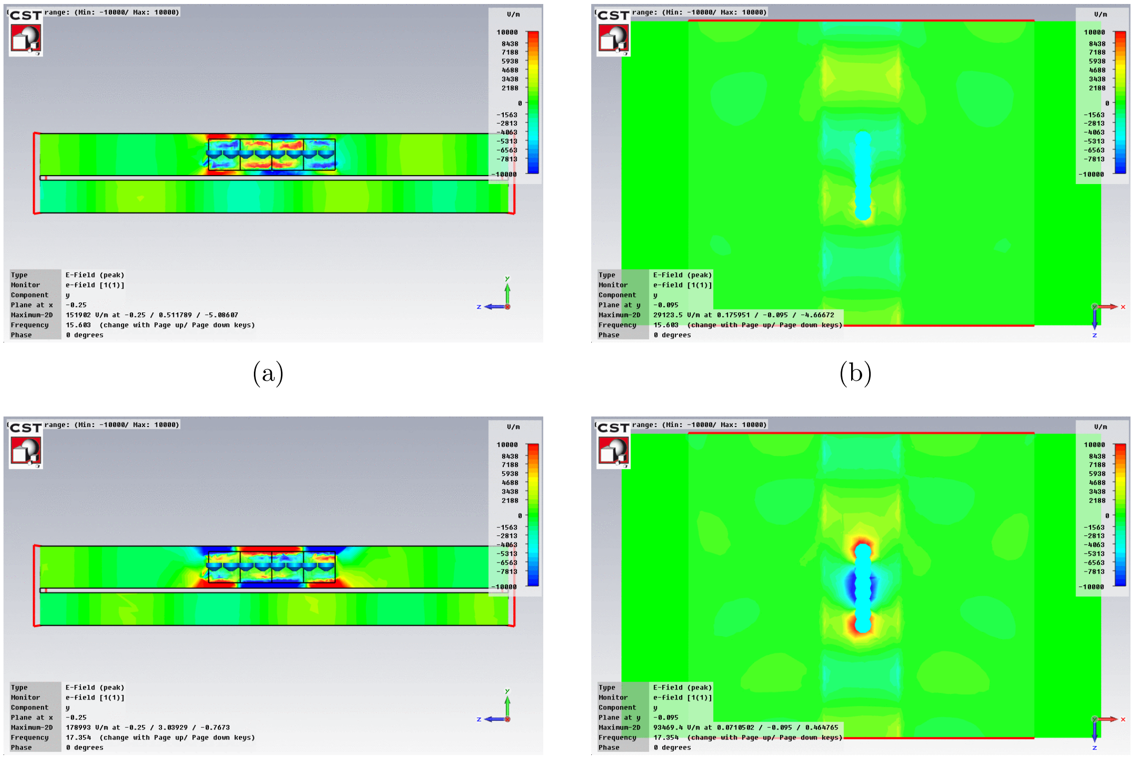

Type E-Field (peak)
Monitor e-field [1(1)]
Component y
Plane at x -0.25
Maximum-2D 151902 V/m at -0.25 / 0.511789 / -5.08607
Frequency 15.603 (change with Page up/ Page down keys)
Phase 0 degrees

(a)

Type E-Field (peak)
Monitor e-field [1(1)]
Component y
Plane at y -0.095
Maximum-2D 29123.5 V/m at 0.175951 / -0.095 / -4.66672
Frequency 15.603 (change with Page up/ Page down keys)
Phase 0 degrees

(b)

Type E-Field (peak)
Monitor e-field [1(1)]
Component y
Plane at x -0.25
Maximum-2D 178993 V/m at -0.25 / 3.03929 / -0.7673
Frequency 17.354 (change with Page up/ Page down keys)
Phase 0 degrees

(c)

Type E-Field (peak)
Monitor e-field [1(1)]
Component y
Plane at y -0.095
Maximum-2D 93469.4 V/m at 0.0710502 / -0.095 / 0.464765
Frequency 17.354 (change with Page up/ Page down keys)
Phase 0 degrees

(d)

Figure 58. Simulated field results from the 4-cell AFIT metamaterial in waveguide with additional cuts in the forth and fifth resonance regions. Fields tangent to a vertical plane in the center of the waveguide, bisecting the waveguide ports, are shown on the left with the images on the right of the page being the fields normal to a horizontal plane located half way between the bottom of the metamaterial structure and the top of the center conductor.

Figures 58(a) and 58(b) depict the simulated fields within the fourth resonance area. The field structure at this frequency is similar to the first and second resonance frequencies, however for the phase angle shown, the field is strongly negative for the first and last cells of the column and strongly positive for the middle two cells in the structure. The horizontal cut shows the creation of a different mode in the waveguide that is not collected by the waveguide ports.

Figures 58(c) and 58(d) show the simulated fields within the fifth resonance. The vertical cut highlights large interactions between the sample and the conductors of the stripline. Additionally, there are large field interactions with the leading and trailing edges of the structure. The fields outside of the sample regions are orders of magnitude smaller than the interactions within the sample region. The localized fields do not propagate to the waveguide port.

In summary, for samples with and without additional cuts, fields within the resonance regions interact with the sample in such a way to create modes other than the principle TEM mode. The lack of propagation appears as nulls in the S-parameter data. These modes evanesce and do not propagate down the waveguide. Outside of the resonance regions the fields do not interact strongly with the structure, allowing the fields to propagate down the waveguide freely.

3.2.4 17-Cell Column in Waveguide - As Fabricated.

After modeling a shorter length column, the model is further refined to include a full length column. The columns are again modeled in the 18 GHz stripline described in Section 3.2.3.1. The stripline method for testing was chosen for these samples as the stripline provides the correct field orientation to achieve metamaterial properties, however a flaw in the sample design orients the wire traces along the propagating axis. The simulated samples are oriented as measured in the physical waveguide. An additional fabrication issue requires additional cuts be made in the material to allow the cantilevers to actuate. Both types of cuts are again examined.

3.2.4.1 Structure with Cuts Across Control Trace.

For the model, all boundaries are set to open, exactly as the empty stripline model. Also, the length of the stripline along the axis of propagation is set to greater than three times the length of the metamaterial structure. For this model, no additional cuts are made as the cantilever control traces are not modeled. To simulate the un-actuated cantilevers, the inner capacitors are held constant and the outer capacitors are varied. The capacitance values simulated for this structure are calculated using Equation (29) and are summarized in Table 4.

The S-parameter analysis results for the inner capacitor set to C0 and the outer capacitor set to C5 for the structure are shown in Figure 59. The inclusion of the 17-cell column leads to 10 areas of sharp resonance. In comparison, there are three areas of resonance seen in simulations of 4-cell columns. The ratio of resonance regions to number of cells in the simulated column is 0.59 and 0.75 for the 17-cell and 4-cell columns respectively.

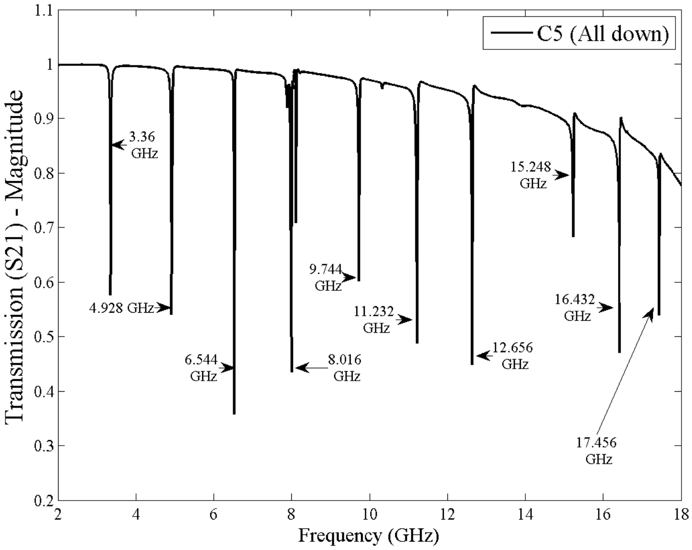

Figure 59. S-parameter analysis of a 17-cell column of the AFIT metamaterial modeled in waveguide with capacitance values of C0 and C5 for the outer and inner respectively. A multitude of resonance areas are seen.

As seen in Section 4.3, the measured results do not show the multitude of resonance regions that the simulation results provide. In an effort to include more of the physics of the actual structure in the model, the cantilever control traces are added.

The control trace for the outer split ring cantilevers is modeled as a thin metal trace connected to the metal trace running along the axis of propagation of the stripline. The new control trace runs vertically from the bottom trace to the center of the split ring gap. The control trace for the inner split ring cantilevers is modeled as a thin metal trace running vertically from the top part of the outer split ring to the center of the split ring gap. There is a 5 μm gap between the outer split ring and cantilever control trace to model the cuts of the trace in the physical samples. The addition of the cantilever control traces is shown in Figure 60.

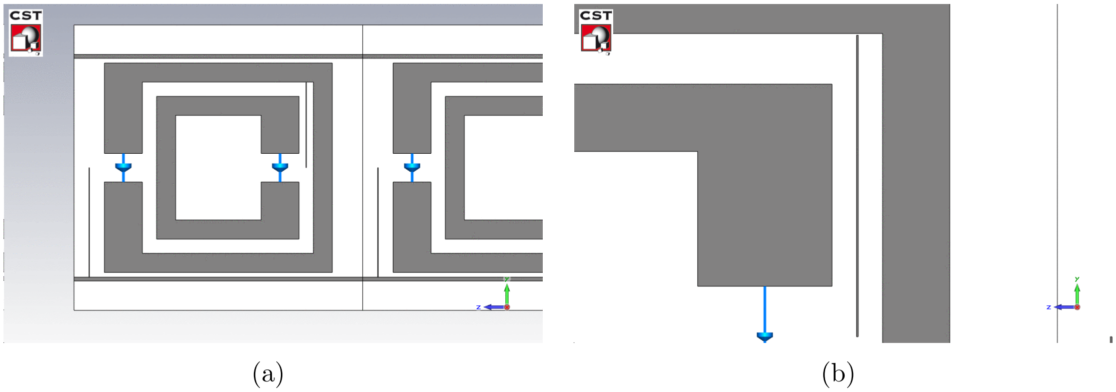

(a) (b)

Figure 60. AFIT metamaterial modeled with control traces. (a) Outer cantilever control trace running from bottom trace to the vertical center of the outer split ring gap. (b) Inner cantilever control trace running from 5 μm away from the inside of the outer split ring to the vertical center of the inner split ring gap.

The S-parameter results of the simulation holding the inner capacitance at C0 and varying the outer capacitance from C0 through C5 are shown in Figure 61(a). The results are still clouded by the multitude of transmission nulls. When compared to measured transmission data, Figure 61(b), the widest simulated transmission nulls are collocated with the measured transmission nulls for the 0 volts applied measurement and the C0 simulation.

With the simulation results still producing a multitude of deep resonance areas that are not evident in the measurements, the model is further refined to incorporate the metal particles as gold, a lossy metal, in the place of the previously modeled PEC.

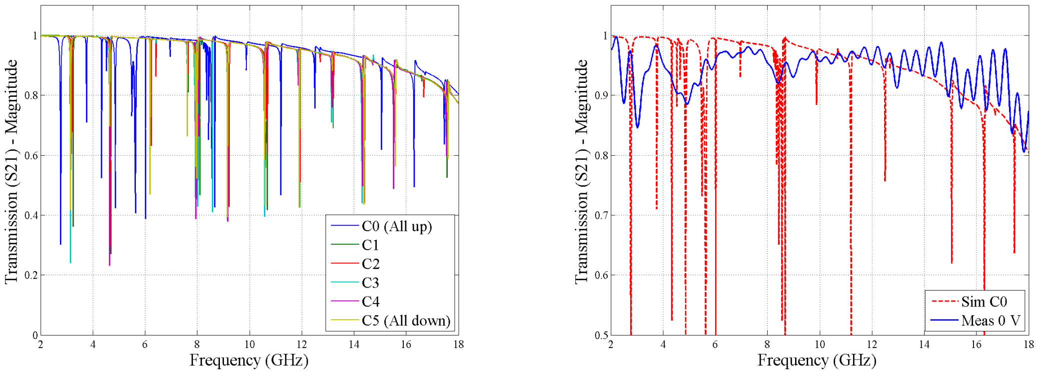

(a)

(b)

Figure 61. (a) Simulated transmission data from a 17-cell column of the AFIT metamaterial without additional cuts and including the control traces. The resonances shift with increased capacitance. (b) Measured transmission data compared to simulated transmission data at 0 volts applied and C0 respectively. The widest simulated transmission nulls are collocated with the measured transmission nulls.

The S-parameter analysis of the structure with metal particles modeled as gold is shown in Figure 62(a). The transmission nulls above 9 GHz seen in the results from the structure modeled as PEC are greatly reduced in depth.

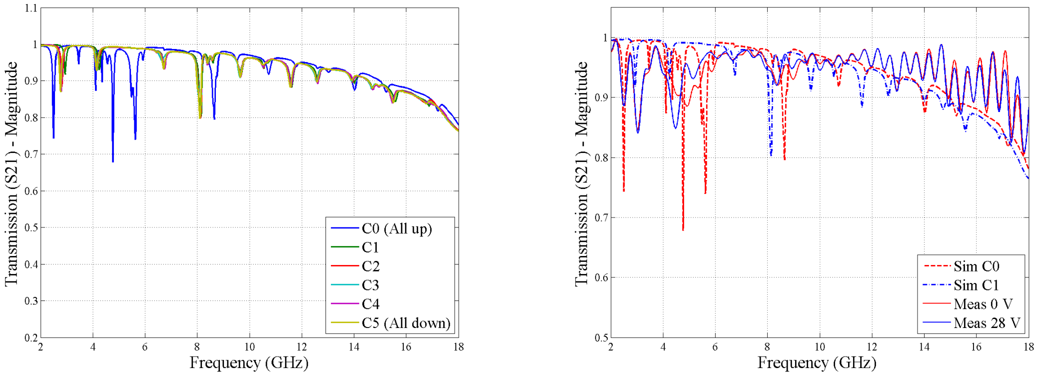

(a)

(b)

Figure 62. (a) Simulated transmission data of 17-Cell column modeled as gold including control traces and cuts across inner control traces compared to measured data. The resonances shifts with increased capacitance. (b) Measured transmission data compared to simulated transmission data at 0 and 28 volts applied and C0 and C1 respectively. The widest simulated transmission nulls are close to the measured nulls, however optimization needs to be completed to determine more accurate capacitance values.

When compared to measurements, shown in Figure 62(b), the simulations for calculated capacitances are close to the measurement results, however an optimization of the simulated capacitance values needs to be carried out to empirically determine the actual capacitor values in the measured structure. The results of the optimization are shown in Section 4.3.4.2.

An examination of the vertical component of the electric field normal to a horizontal plane located half way between the bottom of the metamaterial structure and the top of the center conductor is carried out to determine the field behavior in regions inside and outside of the resonance region. The vertical component of the simulated electric field is shown in Figure 63, with the images on the left of the page being the fields tangent to a vertical plane in the center of the waveguide, bisecting the waveguide ports, and the images on the right of the page being the fields normal to a horizontal plane located half way between the bottom of the metamaterial structure and the top of the center conductor of the waveguide. The color scales of the images are on the same logarithmic scale, with a minimum of -2500 V/m and a maximum of 2500 V/m. Field values below the minimum or above the maximum are displayed as the color of the minimum or maximum respectively. An examination of the fields in the structure shows very little scattering from the structure below the 8 GHz resonance frequency, as seen in Figures 63(a) and 63(b). More scattering from the structure is observed at higher frequencies, leading to a decrease in transmission in that region. There is also a different mode structure at the higher frequencies as seen in Figures 63(e) and 63(f). The presence of the metamaterial structures causes more modes to be excited at lower frequencies than will propagate in the waveguide. The fields inside the resonance area are shown in Figures 63(c) and 63(d). Inside the resonance region, equal amounts of scattering are seen in the forward and reverse directions of the stripline which is different from the higher frequency fields, where scattering in the forward direction dominates.

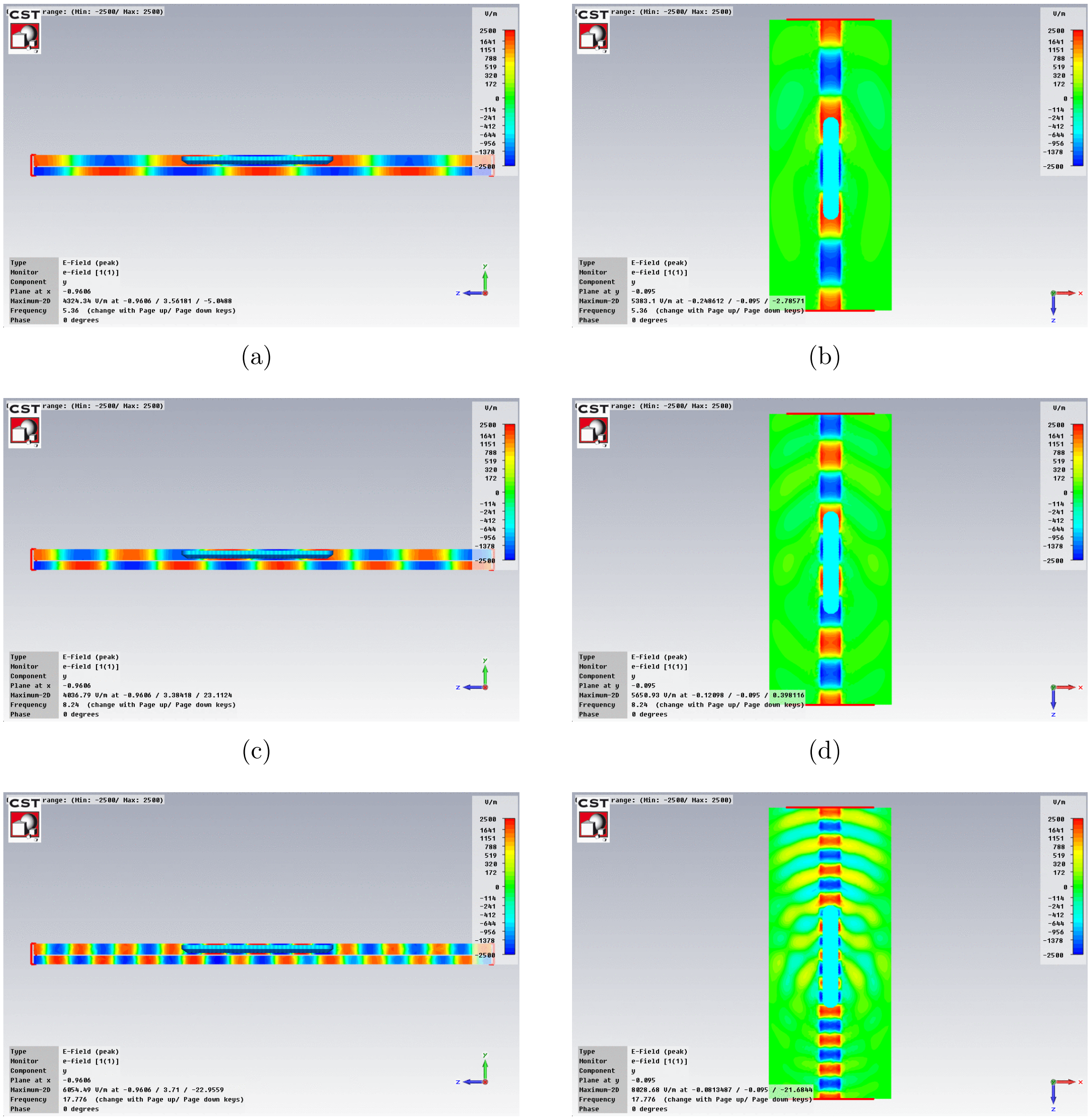

(a) (b)

(c) (d)

(e) (f)

Figure 63. Simulated field results from the 17-Cell AFIT metamaterial in waveguide including cantilever control traces, cuts across inner cantilever control traces, and metal modeled as gold. Fields tangent to a vertical plane in the center of the waveguide, bisecting the waveguide ports, are shown on the left with the images on the right of the page being the fields normal to a horizontal plane located half way between the bottom of the metamaterial structure and the top of the center conductor.

To summarize, below the resonance region, the fields are generally unaffected by the structure, while at and above the resonance region more scattering is seen, leading to high transmission below the resonance region, lower transmission at the resonance frequency and initially high but decreasing transmission as the incident frequency increases from just greater than the resonance frequency. Additionally, as modeled and measured, the interactions within a single column of the structure do not create enough scattering to produce the desired metamaterial effects. Enhanced effects would be seen if multiple columns are used as samples. Due to fabrication difficulties, only single columns of the devices were available for testing. The structure with cuts across the outer split ring is examined next.

3.2.4.2 Structure with Cuts Across Outer SRR.

A similar model refinement progression is completed for the structure with cuts across the outer split ring. For the models, all boundaries are set to open, exactly as previous models including the stripline. Also, the length of the stripline along the axis of propagation is set to greater than three times the length of the metamaterial structure. For this model, 5 μm gaps are included in the outer split ring to simulate the cuts. To simulate the un-actuated cantilevers, the inner capacitor is held constant and the outer capacitor is varied. The capacitance values simulated for this structure are calculated using Equation (29) and are summarized in Table 4.

The results for the model without the control traces is omitted, as the data again yields transmission results clouded by multiple resonances not seen in measurements. The model is refined by the addition of the cantilever control traces. The control trace for the outer split ring cantilevers is modeled as a thin metal trace connected to the bottom metal trace running along the axis of propagation of the stripline. The new control trace runs vertically from the bottom trace to the center of the split ring gap. The control trace for the inner split ring cantilevers is modeled as a thin metal trace running vertically from the top part of the outer split ring to the center of the inner split ring gap. For this structure, the cuts across the outer split ring are included and the new control trace is connected to the outer split ring. The model with the new cantilever control traces is shown in Figure 64.

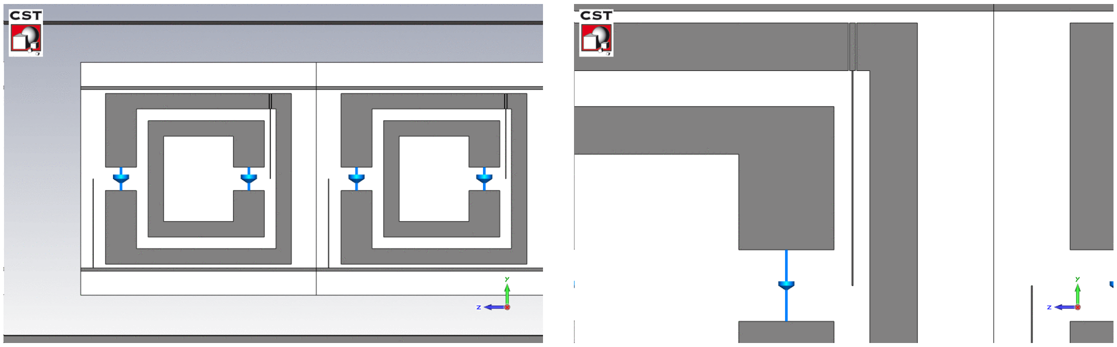

(a) (b)

Figure 64. AFIT metamaterial with cuts across the outer split ring modeled with control traces. (a) Outer trace running from the bottom trace to the vertical center of the outer split ring gap. (b) Inner trace running from the inside of the outer split ring to the vertical center of the inner split ring gap.

The S-parameter results of the simulation holding the outer capacitance constant at C0 and varying the outer capacitance from C0 through C5 are shown in Figure 65(a). The results are still complicated by multiple transmission nulls. There is a large null around 14 GHz and a smaller null around 8 GHz. When compared to measured transmission data, Figure 65(b), the widest simulated transmission nulls are collocated with the measured transmission nulls for the 0 volts applied measurement compared to the C0 simulation.

With the simulation results still producing resonance regions not seen in measurements, the model is further refined. The material of the metal structures is changed to gold, a lossy metal used for the measured samples. The S-parameter analysis of the structure with metal particles modeled as gold is shown in Figure 66(a). The depth of the transmission nulls between the deep resonance areas at 8 and 13 GHz are greatly reduced.

When compared to measurements, shown in Figure 66(b), the simulations for

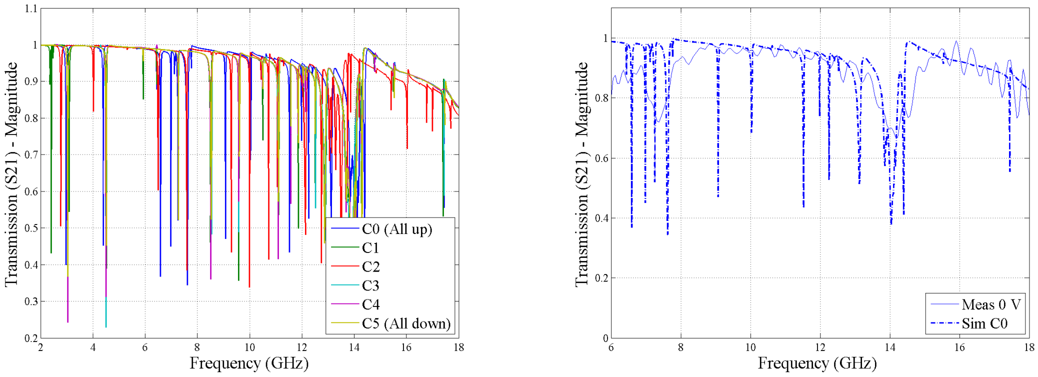

(a) (b)

Figure 65. (a) Simulated transmission data from a 17-cell column of the AFIT metamaterial with additional cuts across the outer split ring and including the control traces. The resonances shift with increased capacitance. (b) Measured transmission data compared to simulated transmission data at 0 volts applied and C0 respectively. The widest simulated transmission nulls are collocated with the measured transmission nulls.

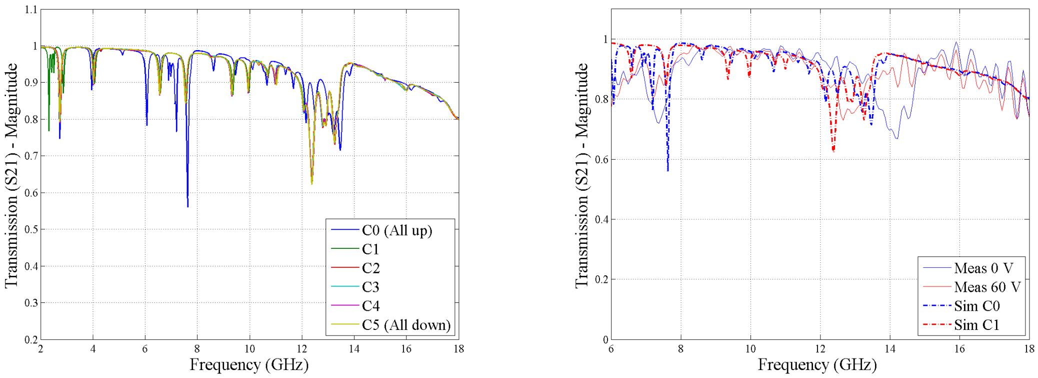

(a) (b)

Figure 66. (a) Simulated transmission data from a 17-cell column of the AFIT metamaterial modeled as gold with additional cuts across outer split ring and including the control traces. The resonances shift with increased capacitance. (b) Measured transmission data compared to simulated transmission data at 0 and 60 volts applied and C0 and C1 respectively. The widest simulated transmission nulls are close to the measured nulls, however optimization needs to be completed to achieve more accurate capacitance values.

calculated capacitances are close to the measurement results, however an optimization of the simulated capacitance values needs to be carried out to empirically determine the capacitor values in the measured structure. The results of the optimization are shown in Section 4.3.3.2.

To determine the field behavior in regions inside and outside the resonance bands, the vertical component of the electric field normal to a horizontal plane located half way between the bottom metamaterial structure and the top of the center conductor is carried out. The frequencies selected and their significance are summarized in Table 8.

Table 8. Frequencies examined for 17-Cell in waveguide model with additional cuts.

Frequency (GHz)	Significance
3.380	Below first resonance
7.953	First resonance
8.871	Between resonances 1 and 2
13.529	Second resonance
15.161	Above resonances

The vertical component of the electric field for the frequencies selected outside resonance regions are shown in Figure 67. The images show the fields normal to a horizontal plane located half way between the bottom of the metamaterial structure and the top of the center conductor. The color scales of the images are on the same logarithmic scale, with a minimum of -2500 V/m and a maximum of 2500 V/m. Field values below the minimum or above the maximum are displayed as the color of the minimum or maximum respectively.

Below the resonances, very little fields are scattered by the structure, as seen in Figures 67(a) and 67(b), leading to high transmission. Between the resonances the field is still only slightly scattered, shown in Figures 67(c) and 67(d). Above the resonances, the fields are scattered by the structure, however mostly in the forward direction of the waveguide, leading to higher transmission than in the resonance regions. The fields above the resonance regions are depicted in Figures 67(e) and 67(f).

The vertical component of the electric field for two resonance frequencies are

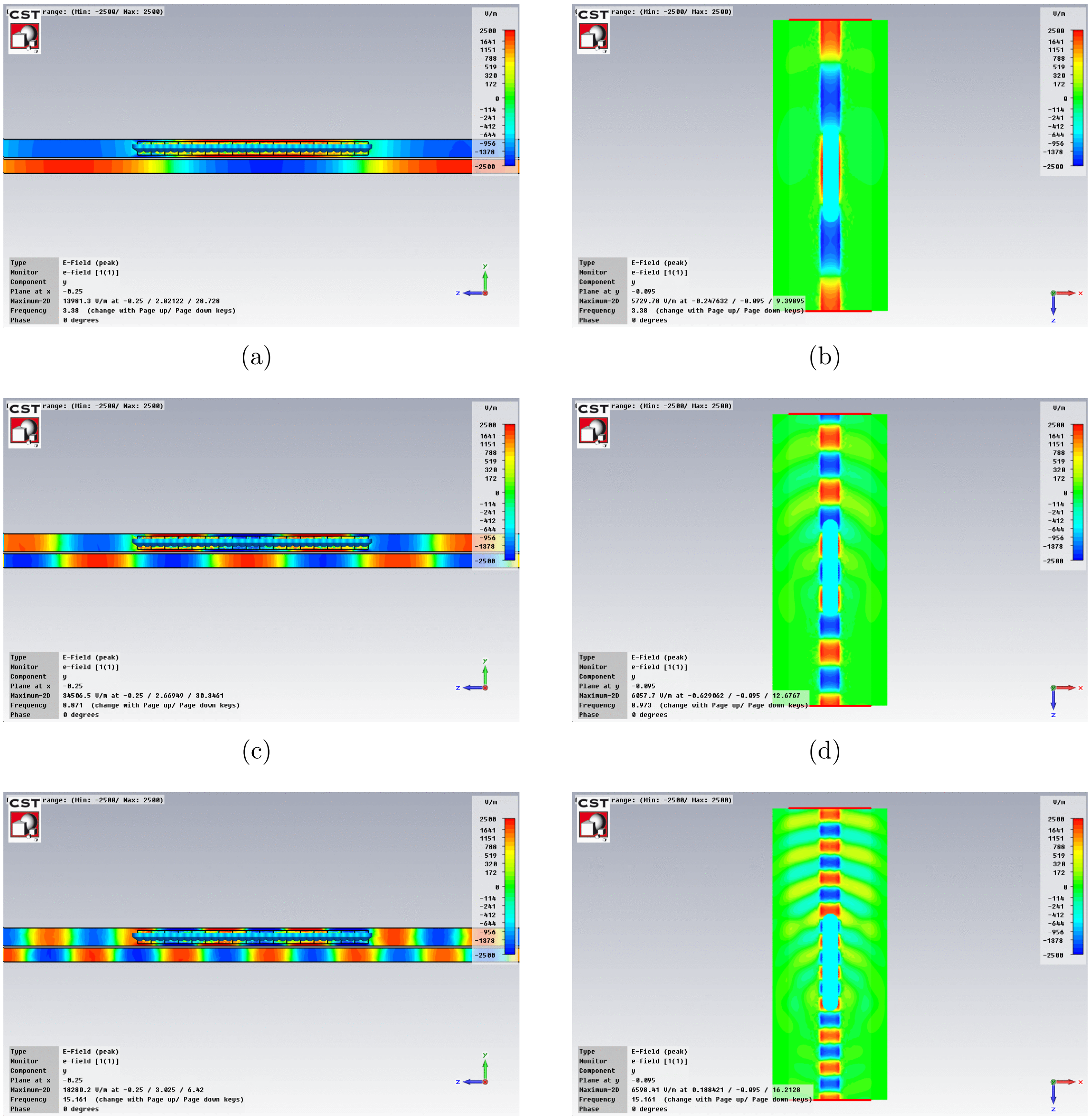

(a) (b)

(c) (d)

(e) (f)

Figure 67. Simulated field results outside of the resonance regions from the 17-Cell AFIT metamaterial in waveguide with additional cuts across the outer split ring and metal modeled as gold. Fields tangent to a vertical plane in the center of the waveguide, bisecting the waveguide ports, are shown on the left with the images on the right of the page being the fields normal to a horizontal plane located half way between the bottom of the metamaterial structure and the top of the center conductor.

shown in Figure 68. At the first resonance frequency, shown in Figures 68(a) and 68(b), the fields do not maintain their strength upon transmission through the sample. The fields are reduced in strength and scatter mostly in the forward direction. Figures

68(c) and 68(d) shows the fields at the second resonance. There are sub-wavelength sized interactions observed along the top and bottom edges of the column. The fields are scattered from the structure in all directions, leading to greatly reduced fields traveling to the second waveguide port. In light of these field results, the transmission data behaves as expected. The transmission is high below the resonance frequencies and lower within the resonance regions. Above the resonance areas, the transmission decreases as expected from the increased scattering observed in the field results.

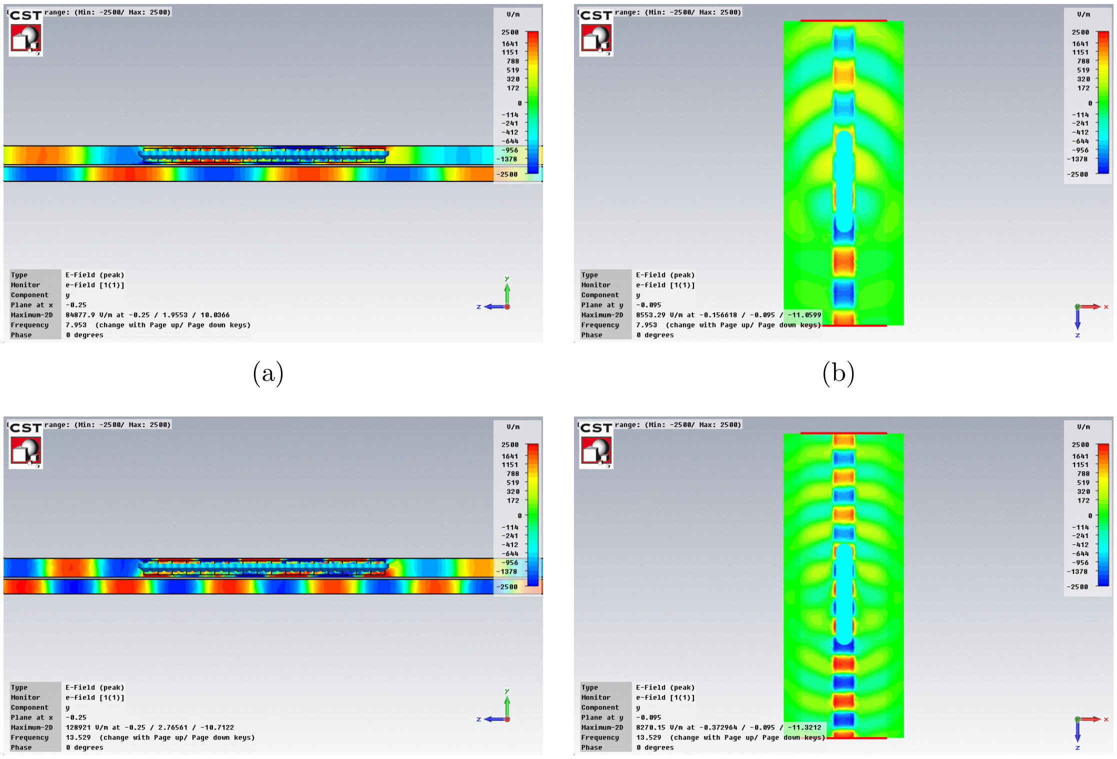

Type	E-Field (peak)
Monitor	e-field [1(1)]
Component	y
Plane at x	-0.25
Maximum-2D	84877.9 V/m at -0.25 / 1.9553 / 10.0366
Frequency	7.953 (change with Page up/ Page down keys)
Phase	0 degrees

(a)

Type	E-Field (peak)
Monitor	e-field [1(1)]
Component	y
Plane at y	-0.095
Maximum-2D	8553.29 V/m at -0.156618 / -0.095 / -11.0599
Frequency	7.953 (change with Page up/ Page down keys)
Phase	0 degrees

(b)

Type	E-Field (peak)
Monitor	e-field [1(1)]
Component	y
Plane at x	-0.25
Maximum-2D	128921 V/m at -0.25 / 2.76561 / -10.7122
Frequency	13.529 (change with Page up/ Page down keys)
Phase	0 degrees

(c)

Type	E-Field (peak)
Monitor	e-field [1(1)]
Component	y
Plane at y	-0.095
Maximum-2D	8270.15 V/m at -0.372964 / -0.095 / -11.3212
Frequency	13.529 (change with Page up/ Page down keys)
Phase	0 degrees

(d)

Figure 68. Simulated field results in the resonance regions from the 17-Cell AFIT metamaterial in waveguide with additional cuts across the outer split ring and metal modeled as gold. Fields tangent to a vertical plane in the center of the waveguide, bisecting the waveguide ports, are shown on the left with the images on the right of the page being the fields normal to a horizontal plane located half way between the bottom of the metamaterial structure and the top of the center conductor.

3.2.5 Smaller Scale AFIT Adaptive Metamaterial Model Conclusions.

The basic single cell models of the structures provide a starting point to examine the basic regions of resonance. The stripline models provide a powerful tool to explore electromagnetic field behavior in metamaterials. The empty stripline model accurately predicts the propagating modes, including the cutoff frequencies. The S-parameters from the empty stripline model show that the operation of the stripline between 0 and 18 GHz is very close to ideal. The model also confirms that results from the stripline above 18 GHz should be disregarded.

The models are refined from a single unit cell to the full length, 17-cell column in the physical waveguide, simulating the samples as measured. The model refinement procedure leads to models that match the general operation of the samples, while balancing computation requirements. With the cantilever structures modeled as lumped element capacitors, the models effectively simulated the measurements, as seen in Sections 4.3.3.2 and 4.3.4.2. The simulation results with optimized capacitor values effectively match measured transmission results. The simulations provided immense insight into the field behavior both inside and outside of the resonance regions of the samples. Field investigations into 4-cell structures show different resonance modes at different resonance regions. The inclusion of the cantilever control traces and lossy metal in the model lead to decreased resonance behavior in the transmission null regions. The resonance modes seen in the 4-cell PEC models are not seen strongly in the models that take most of the physics of the samples into account. The transmission loss appears to come from scattering from the sample within the resonance regions. Additionally, there is a distinct roll off of the transmission at higher frequencies caused by more scattering as the wavelength decreases. Despite the size of the metallic inclusions and separation distances compared to the wavelength of incident energy meeting size requirements discussed in Chapter II, there is still non-negligible scattering, and therefore transmission loss at the higher frequencies.

The smaller AFIT metamaterial design is next adjusted to account for the lessons learned from fabrication and increased in size to be measured in the larger AFIT stripline. The larger model is oriented appropriately in the waveguide and no additional cuts are required. The model refinement process is applied to these larger samples with expected resonance regions around 3 GHz.

3.3 Larger AFIT Models

A variation of the previous AFIT adaptive metamaterial structure is examined next. This structure is based on a scaled version of the previously examined structure. The unit cell is four times the size of the structure designed to resonate at 10 GHz. The new structure is designed to resonate around 3 GHz as to use AFIT's larger stripline to make measurements of the samples. The design of the 3 GHz structures is improved from the 10 GHz samples. No additional cuts are required for the cantilevers to actuate, allowing both the inner and outer ring capacitors to change at the same time. The cantilever sets are designed to achieve that same capacitances as calculated for the smaller samples. The capacitances are calculated using Equation (29) and are listed in Table 4. The samples are also fabricated such that the thicker traces are aligned with the dominant electric field component in the stripline, attempting to achieve negative permittivity as discussed in Section 2.2.2.1.

There are five different capacitor layouts examined for the larger SRR samples. The five different layouts are shown in Figure 69. The first layout (layout A) has the cantilevers arranged as the previous design, with one cantilever set in each of the split ring gaps. The second layout (layout B) has one set of cantilevers on each side of the structure between the inner and outer split rings. Based on the work of Lundell in [23], the intra-ring capacitance is expected to have a greater impact than the gap capacitance with the larger structures. Layout C is similar to layout B, however there are two sets of intra-ring cantilevers on each side of the cell. Layout D is a combination between layouts B and C, with sets of cantilevers in each of the split ring gaps as well as two sets of intra-ring cantilevers per side of the unit cell, six sets of cantilevers in total. Layout E is similar to layouts B and C, having three sets of intra-ring cantilevers on each side of the cell. For all models discussed here, the structures do not include the thinner metal traces found to have a large impact with

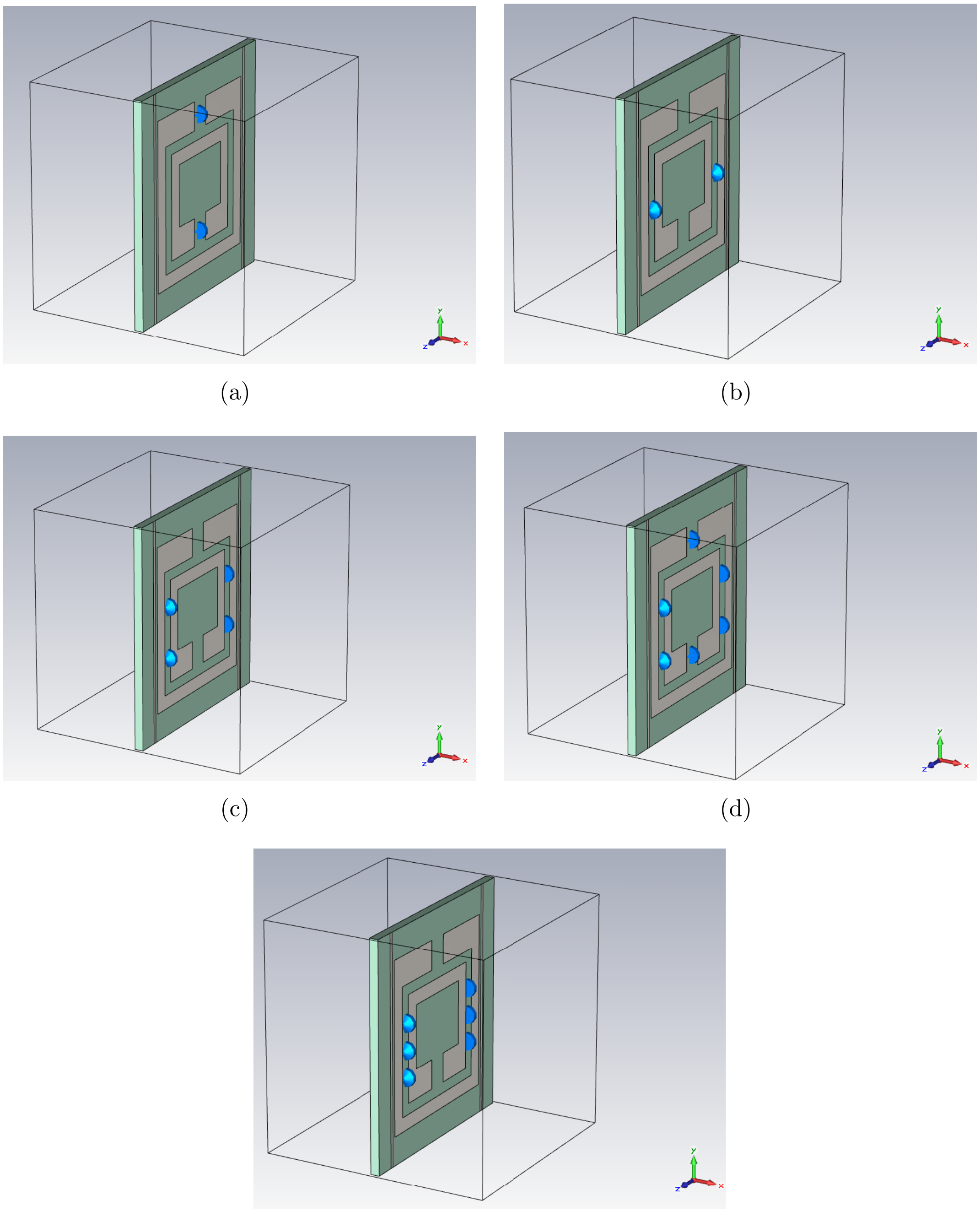

(a) (b)

(c) (d)

(e)

Figure 69. Larger AFIT metamaterial variants. (a) Layout A with cantilevers in the gaps of the split rings. (b) Layout B with one set of cantilevers between the inner and outer split ring per side of the cell. (c) Layout C with two sets of cantilevers between the inner and outer split ring per side. (d) Layout D with sets of cantilevers in the split ring gaps and two sets per side of the cell. (e) Layout E with three sets of intra-ring cantilevers per side of the cell.

the smaller structures. The thinner traces for the larger samples are oriented along the propagation axis and do not interact strongly with the fields. Also, the metal structures are modeled as PEC.

For the examination of the variants of the larger samples, the empty stripline model is first examined, followed by the model refinement progression for each of the variants. The model is refined from a unit cell model to a single cell model, followed by a 4-cell strip in the waveguide as the samples are measured. The mesh statistics for all models of the larger AFIT metamaterial design can be found in Table 16 and solve times for the simulations can be found in Table 15. Both tables are in Appendix A.

3.3.1 4 GHz Stripline.

The larger AFIT adaptive metamaterial structures are designed to be tested using a stripline waveguide designed for operation up to 4 GHz. To verify the operation of the stripline and to gain some insight into its frequency modes, a cross-sectional model of the stripline is constructed using CST MWS®. The model is shown in Figure 70. The physical dimensions of the model match the actual dimensions of the waveguide. All metal pieces are modeled as PEC, and all boundaries are set to open. The length of the stripline is greater than three times the length of the longest sample to be measured in the physical stripline. The number of port modes simulated is set to four for all simulations of the larger AFIT adaptive metamaterial structures in the simulated waveguide. It is assumed that the physics of the structures is captured within these four modes and that higher order modes will have decayed before reaching the waveguide ports.

The results of the simulation are shown in Figure 71. Figures 71(a) and 71(b) show $\boldsymbol{E}$ and $\boldsymbol{H}$ at the longitudinal center of the waveguide. As expected, $\boldsymbol{E}$ radiates

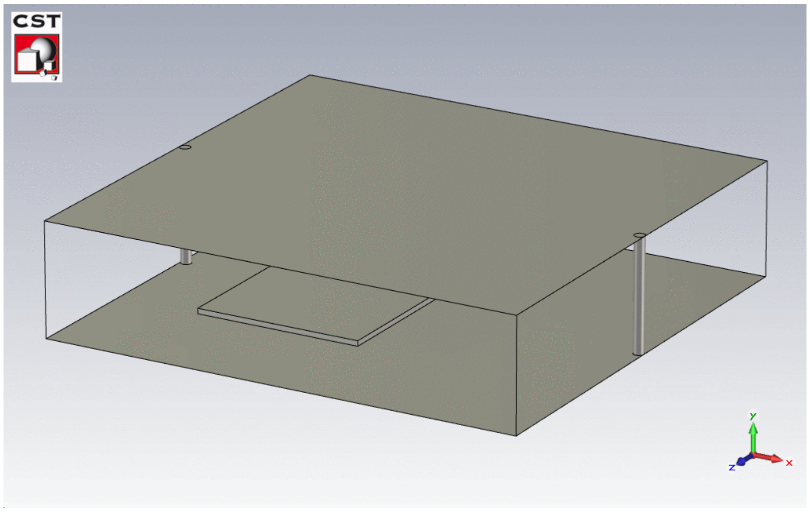

Figure 70. Model of the empty 4 GHz stripline. The cross sectional dimensions of the stripline structure match the physical dimensions of the actual stripline.

in and out of the center conductor of the stripline while $\boldsymbol{H}$ circles around the center conductor. The magnitudes of the reflection and transmission from the simulation are shown in Figure 71(e). Ideally, S_{11} would be close to zero and S_{21} should be close to one for frequencies below the cutoff of the second propagating mode. The simulation results match the expected behavior.

Additionally, the simulation provides insight into the second mode of the stripline. The cutoff frequency of the second mode is about 4.06 GHz. Figures71(c) and 71(d) show the electric and magnetic fields respectively at the longitudinal center of the waveguide above the cutoff frequency of the second mode. The results show lateral variation along the center conductor of the stripline. This confirms that results above 4 GHz should be disregarded for both simulation and measurement. The five variants of the larger AFIT metamaterial structure are examined next.

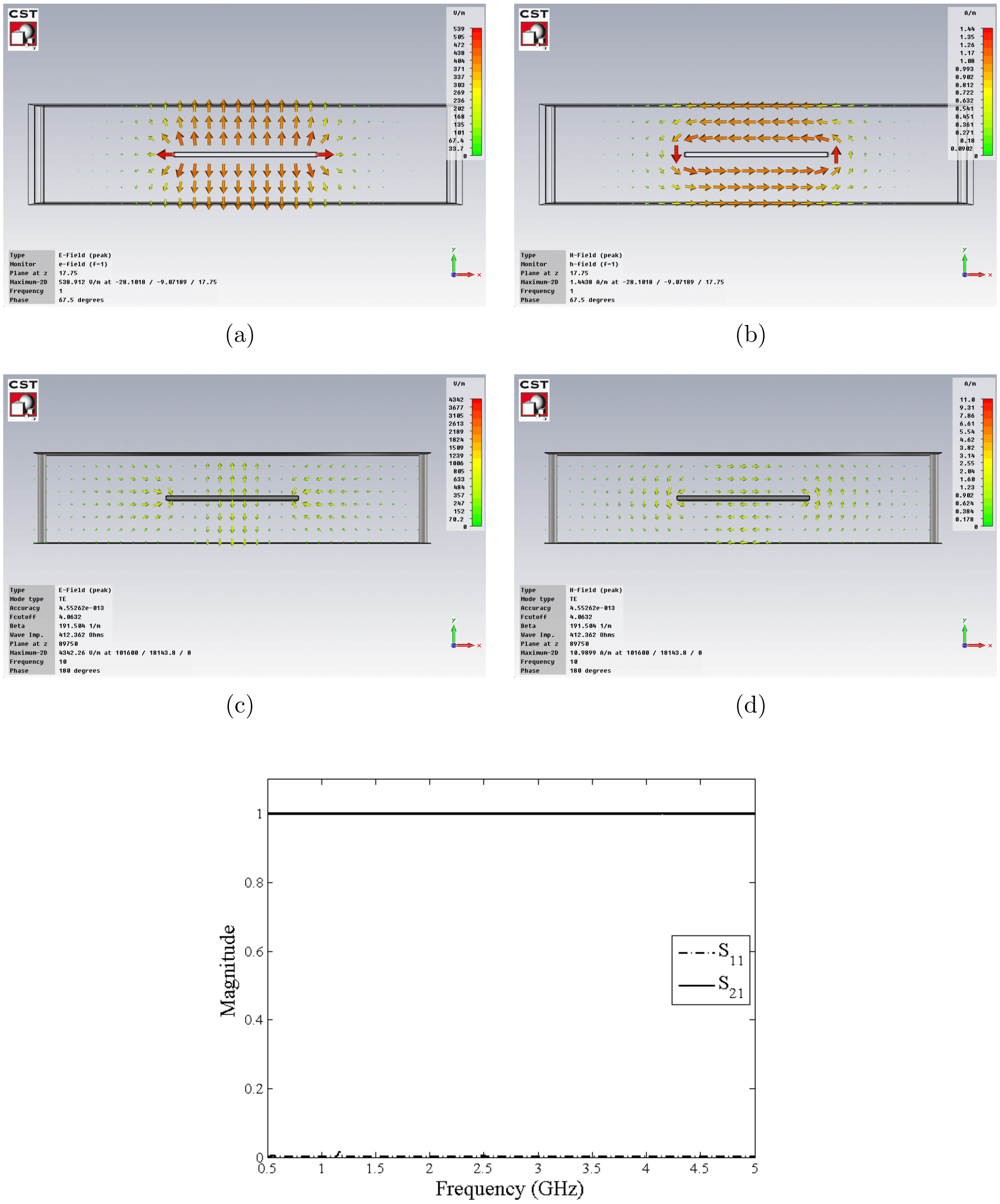

Type	E-Field (peak)
Monitor	e-field (f=1)
Plane at z	17.75
Maximum-2D	538.912 V/m at -28.1018 / -9.07189 / 17.75
Frequency	1
Phase	67.5 degrees

(a)

Type	H-Field (peak)
Monitor	h-field (f=1)
Plane at z	17.75
Maximum-2D	1.4438 A/m at -28.1018 / -9.07189 / 17.75
Frequency	1
Phase	67.5 degrees

(b)

Type	E-Field (peak)
Mode type	TE
Accuracy	4.55262e-013
Fcutoff	4.0632
Beta	191.504 1/m
Wave Imp.	412.362 Ohms
Plane at z	89750
Maximum-2D	4342.26 V/m at 101600 / 18143.8 / 0
Frequency	10
Phase	180 degrees

(c)

Type	H-Field (peak)
Mode type	TE
Accuracy	4.55262e-013
Fcutoff	4.0632
Beta	191.504 1/m
Wave Imp.	412.362 Ohms
Plane at z	89750
Maximum-2D	10.9899 A/m at 101600 / 18143.8 / 0
Frequency	10
Phase	180 degrees

(d)

(e)

Figure 71. Results from the empty 4 GHz stripline simulation. (a) *E* at the center of the stripline radiates in and out of the center conductor as expected. (b) *H* at the center of the stripline circulates around the center conductor as expected. (c)*E* and (d) *H* at the center of the stripline at frequencies above the cutoff for the second mode show lateral variation along the center conductor. (e) Simulated transmission and reflection are one and zero respectively, as expected from an ideal empty waveguide.

3.3.2 Capacitor Layout A.

For all five capacitor layouts, results are presented from three simulations:

1. a unit cell model, one unit cell deep along the axis of propagation, extending infinitely in the two non-propagation directions, stimulated by a TEM mode,
2. a single cell model stimulated by a TEM mode with the electric field oriented along the vertical wire traces, and
3. a 4-cell column simulated in the model of the physical waveguide.

With each step, the model is refined to be closer to actual measurements. The first simulation provides information about locations of resonance areas in the frequency domain, while extremely limiting the length of time required for simulation. The second simulation is stimulated by a TEM mode as the samples would be in the measurement setup. The final simulation provides results for comparison to measurements without modeling the physical dimensions of the sets of cantilevers thereby balancing the need for simulations that accurately model the physics of the samples with the requirement for timely simulation data.

The simulation results for the three types of simulations of the structure with capacitor layout A are shown in Figure 72. Figure 72(a) shows the results from the unit cell simulation. Despite the slight magnitude changes, there appears to be an area of resonance above 2 GHz for C0, that shifts to 1 GHz for the remainder of the capacitance values. Figure 72(b) depicts the results from the single cell simulation. The results show a similar location for the resonance frequency at 2 GHz for C0 that shifts to below 0.5 GHz for C4 and C5. Figure 72(c) again, shows similar dispersive transmission results for the 4-cell column in the waveguide. The single resonance frequency shifts from an initial location of 2 GHz to below 0.5 GHz by C3.

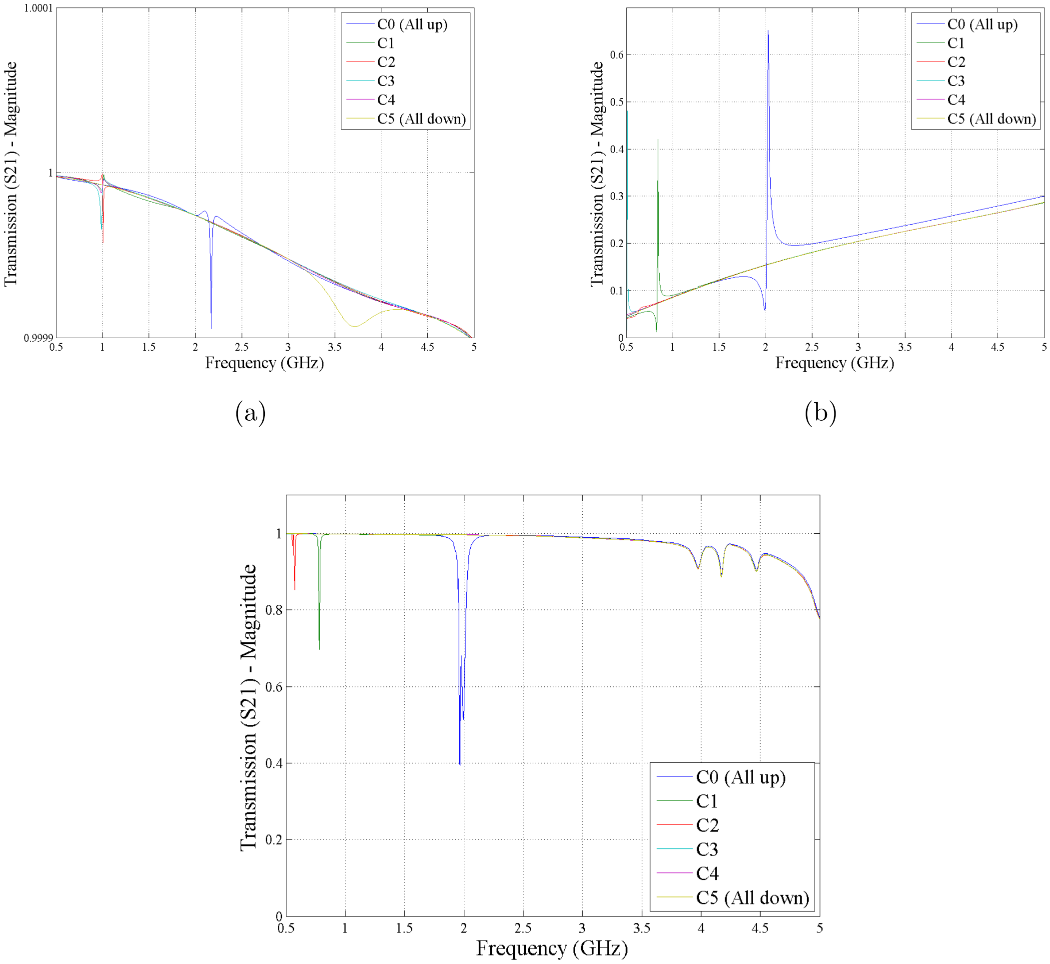

(a)

(b)

(c)

Figure 72. Simulation results from the larger AFIT metamaterial structure with capacitor layout A. Results from (a) unit cell, (b), single cell, and (c) a 4-cell column in the waveguide simulations show a single resonance region shifting with increased capacitances.

3.3.3 Capacitor Layout B.

Results from simulations of the AFIT metamaterial structure with capacitor layout B are presented next. Simulations were not completed for the sample in the waveguide, as no samples were created for testing. Figures 73(a) and 73(b) show simulation results from the unit cell and single cell simulations of the structure with capacitor layout B. The unit cell results show very high transmission with a resonance area around 2.5 GHz for C0, that is not seen other than a smaller area of resonance around 1 GHz for C1. The single cell results show a region of resonance at 2.5 GHz for C0 that shifts to just above 0.5 GHz for C5. There is also an area of resonance around 4 GHz for C1 through C5 that is not observed for C0.

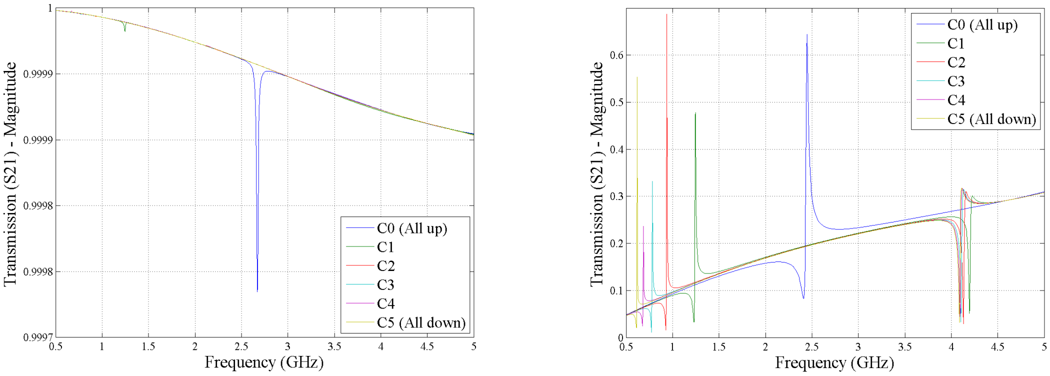

(a)

(b)

Figure 73. Simulation results from the larger AFIT metamaterial structure with capacitor layout B. Results from (a) unit cell, (b), single cell, and (c) a 4-cell column in the waveguide simulations show a shifting resonance region around 2.5 GHz, shifting with increased capacitances. There is an additional resonance region seen at 4 GHz.

3.3.4 Capacitor Layout C.

Simulated transmission results for the AFIT metamaterial structure with cantilever layout C are depicted in Figure 74. Figure 74(a) shows the results from the unit cell simulation. Minimal resonance is seen with the unit cell structure. The simulated results from the single cell model are shown in Figure 74(b). The transmission data is clouded by multiple resonance areas. There appears to be a shifting resonance area at 2.25 GHz that shifts downward with increasing capacitance. There is also a resonance region at 4.5 GHz. There is a resonance for C1 seen below 3 GHz that appears to shift for C2 through C5. Figure 74(c) shows a similar set of multiple resonance regions for the 4-cell simulations. At C0, the single region is seen around 2.25 GHz. For C1 and C2, two shifting regions are seen. For C3 through C5, the resonances appear to have shifted below 0.5 GHz.

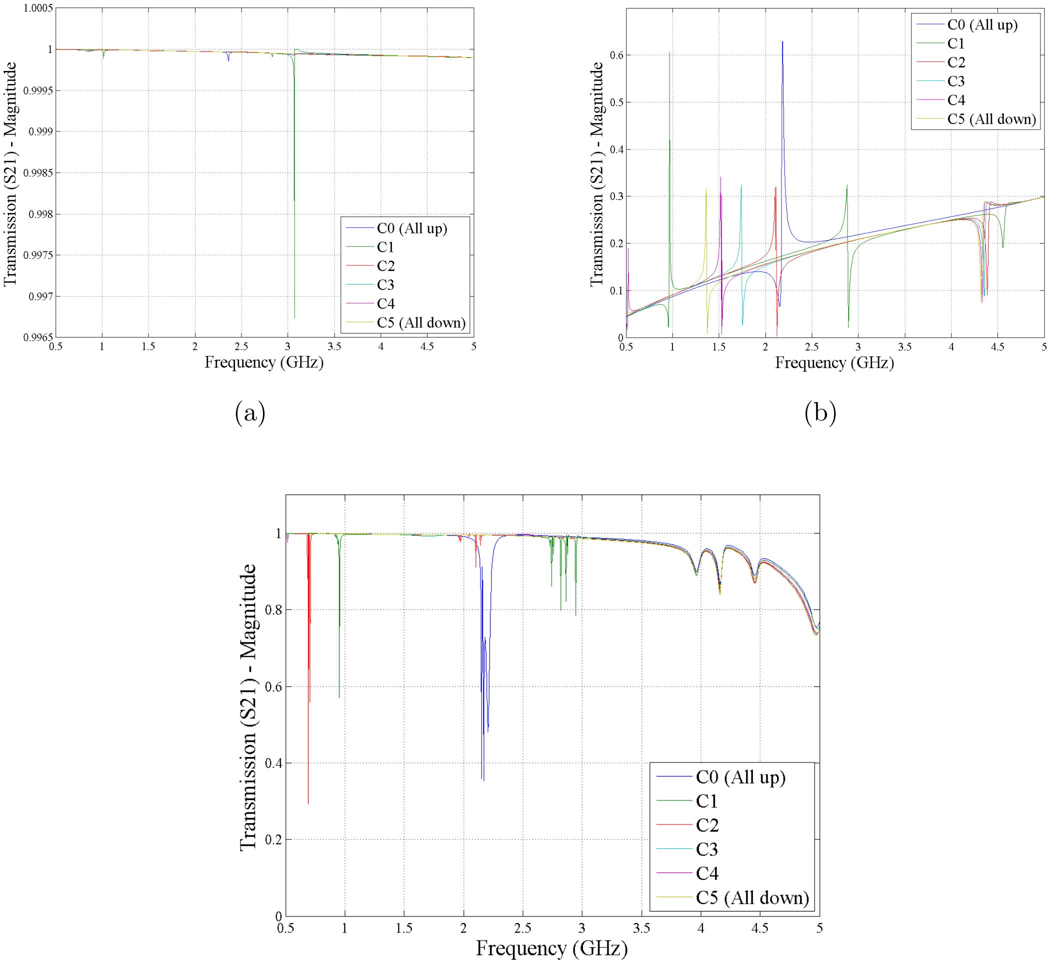

(a) (b)

(c)

Figure 74. Simulation results from the larger AFIT metamaterial structure with capacitor layout C. Results from (a) unit cell, (b), single cell, and (c) a 4-cell column in the waveguide simulations show multiple resonance regions shifting with increased capacitances.

3.3.5 Capacitor Layout D.

Simulated transmission results for the AFIT metamaterial structure with cantilever layout D are shown in Figure 75. Figure 75(a) shows the results from the unit cell simulation. Multiple resonance regions are seen for all capacitor values. Figure

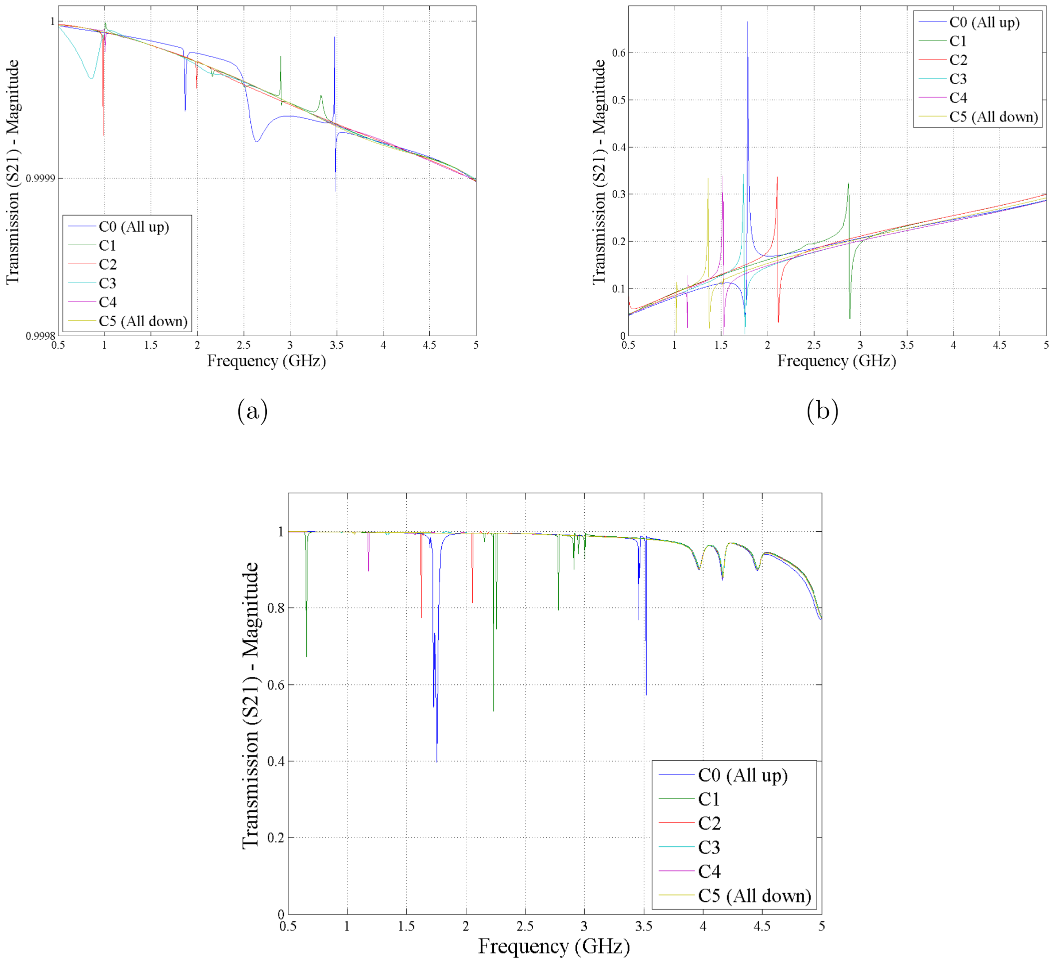

(a) (b)

(c)

Figure 75. Simulation results from the larger AFIT metamaterial structure with capacitor layout D. Results from (a) unit cell, (b), single cell, and (c) a 4-cell column in the waveguide simulations show multiple resonance regions shifting with increased capacitances.

75(b) depicts the transmission data from the single cell simulations. The greater number of cantilever sets, as represented by lumped element capacitors, pushes the initial resonance frequency at C0 to 1.75 GHz. At C1, a resonance appears at 2.75 GHz, that shifts downwards for C2 through C5. This resonance may be above 5 GHz at C0, and shifts into range for the remaining capacitance values, while the resonance for C0 shifts below the frequency range for the remaining frequencies. Figure 75(c) shows the simulated transmission results from the 4-cell structure in the waveguide. The C0 results show two resonance regions at 1.75 GHz and 3.5 GHz, that shift to 0.75 GHz and 2.25 GHz for C1, respectively. There is also a third resonance region for C1 at 2.75 GHz. The resonance regions shift out of the frequency range as the capacitance values increase. The increased number of capacitors adds to the complexity of the transmission data.

3.3.6 Capacitor Layout E.

Simulated transmission results for the AFIT metamaterial structure with capacitor layout E are shown in Figure 76. Figure 76(a) shows the clouded results for the unit cell model. Figure 76(b) shows the transmission data from the single cell simulations. Similar to capacitor layout C, multiple resonance areas are seen. There is an area of resonance at 2 GHz for C0 that appears to shift below the frequency range for greater capacitance values. There is also a resonance region around 2.75 GHz for C1 that shifts to around 1.25 GHz for C5. Furthermore, there is a constant area of resonance around 4.5 GHz. Figure 76(c) shows the transmission data from the 4-cell structure in the waveguide, revealing a similar set of resonance areas.

3.3.7 Larger AFIT Model Recommendations.

Having reviewed simulated results from all five variants of the larger AFIT metamaterial structure, recommendations can be made for design improvements. While there are clear resonance shifts observed for the structures simulated with additional intra-ring capacitance, the multiple resonance areas complicate analysis. Also, cell to cell variance of additional capacitance in the physical devices can limit the strength of the resonances. The single resonance frequency provided by layout A provides transmission results that are easily evaluated for resonance frequency shifts. The ca-

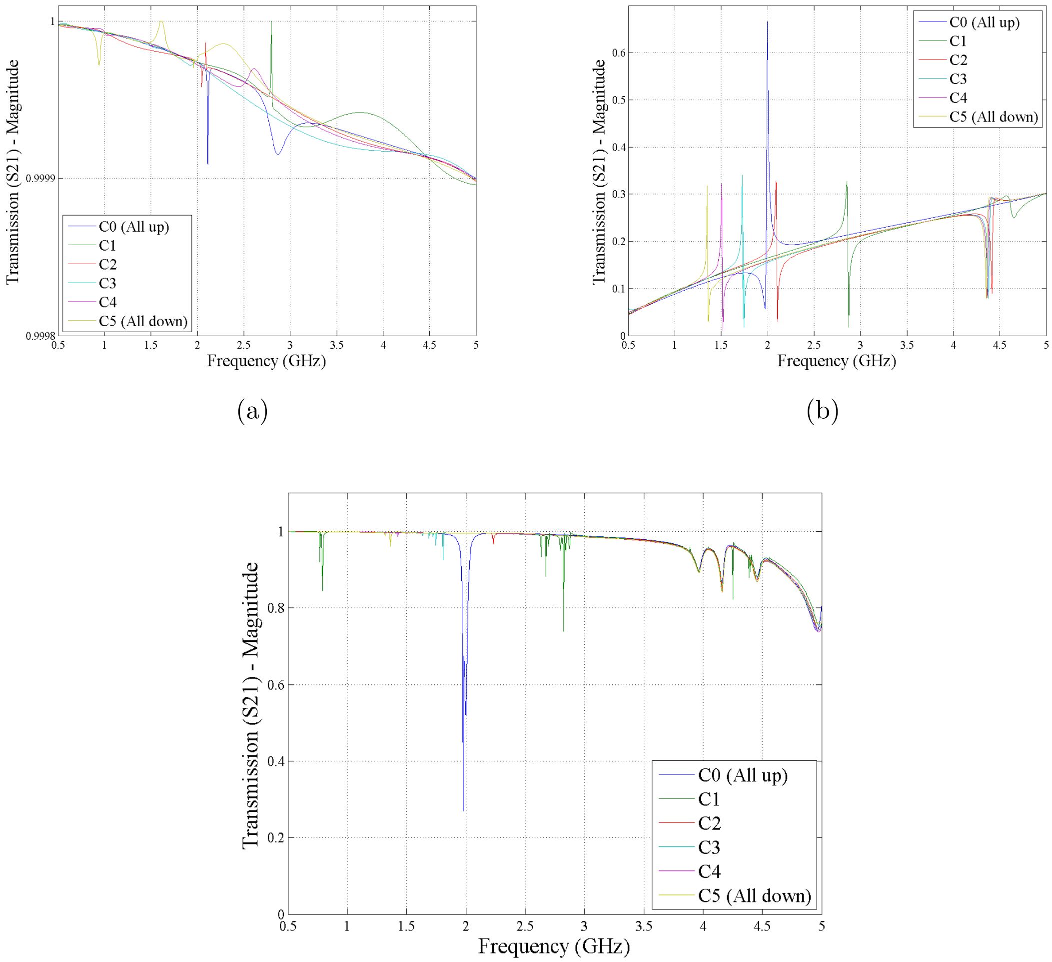

(a)

(b)

(c)

Figure 76. Simulation results from the larger AFIT metamaterial structure with capacitor layout E. Results from (a) unit cell, (b), single cell, and (c) a 4-cell column in the waveguide simulations show multiple resonance regions shifting with increased capacitances.

pacitance change required to achieve a shift within the frequency range of the stripline is examined. Various capacitance values are simulated and the resonance frequencies are calculated. The resultant resonance frequencies are shown in Figure 77(a).

Based on the simulated resonance frequencies for layout A, a non-linear increase in capacitance values is recommended. To achieve a shift from 2.3 GHz to 1.0 GHz, a change of capacitance from 0.1 pF to 1.5 pF needs to occur. The recommended cantilever states are summarized in Table 9. The simulated transmission using the recommended capacitance values shows a linear shift in resonance frequency, as seen in Figure 77(b).

Table 9. Recommended additional capacitance values for MEMS cantilevers

State	Activated Beams	Capacitance (pF)
C0	None	0.1
C1	1	0.2
C2	2	0.4
C3	3	0.7
C4	4	1.5

The other layouts are not recommended for further design improvements. As the number of capacitors is increased, the strength of resonant mode coupling is decreased, as seen in measurements of the samples, presented in Section 4.4.

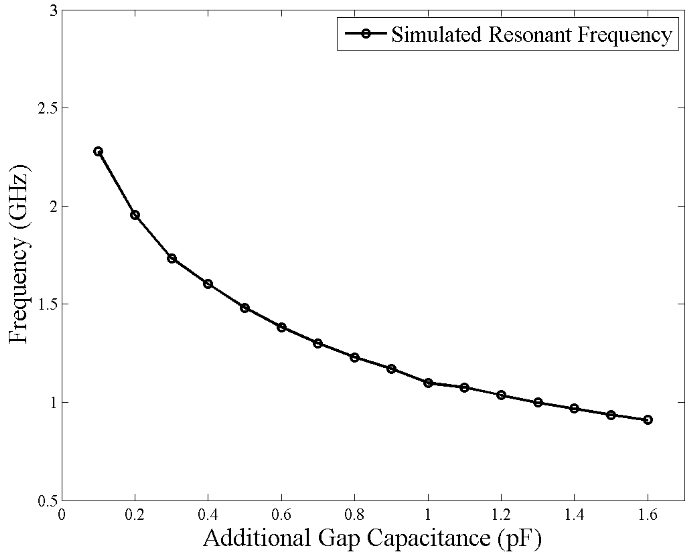

(a)

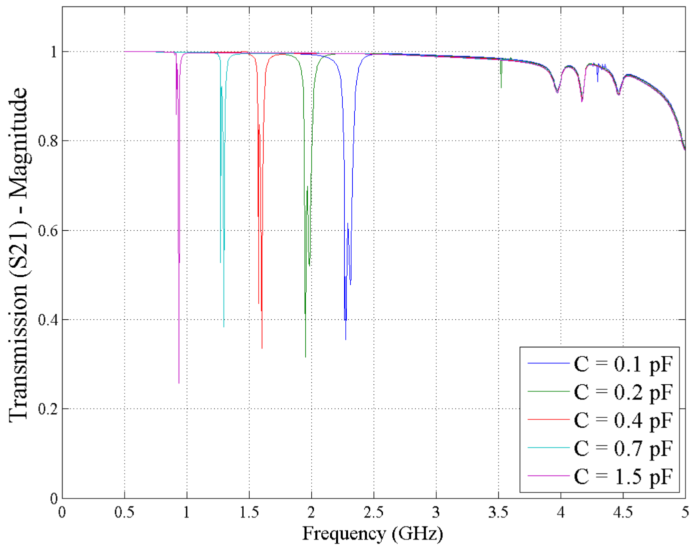

(b)

Figure 77. Simulation results from the larger AFIT metamaterial structure with capacitor layout A capacitance investigation. (a) Simulated resonance frequency results for larger AFIT metamaterial structure with capacitor layout A. As expected, a linear increase in frequency does not provide a linear shift in frequency. (b) Transmission results for recommended capacitance values leads to a linear shift in resonance frequencies.

3.4 2D-Focus Beam Measurement System

An alternate method for making transmission and reflection measurements of metamaterial samples is also investigated. The stripline measurement method is limited to a small set of incident angles as the field is only constant in the area between the broad sides of the inner and outer conductors as seen in Sections 3.2.3.1 and 3.3.1. The alternate measurement methodology examined attempts to create a technique viable for examining responses for fields of off-normal incidence. The measurement system examined is a two dimensional radio frequency (RF) focusing system fed by a simulated monopole. The system allows for rotation of a sample. The system is shown in Figure 78. The system is sized to fit into the AFIT broadband antenna near-field test and measurement (BANTAM) range. The design would have a bottom plate the size of the entire enclosure and a smaller top plate that would allow for scanning the measurement area with a field probe located at the center of the top plate. The focusing lenses are a scaled version of the profile of the Georgia Tech Research Institute (GTRI) three dimensional focus beam system. The lenses are scaled to fit the system in the BANTAM range.

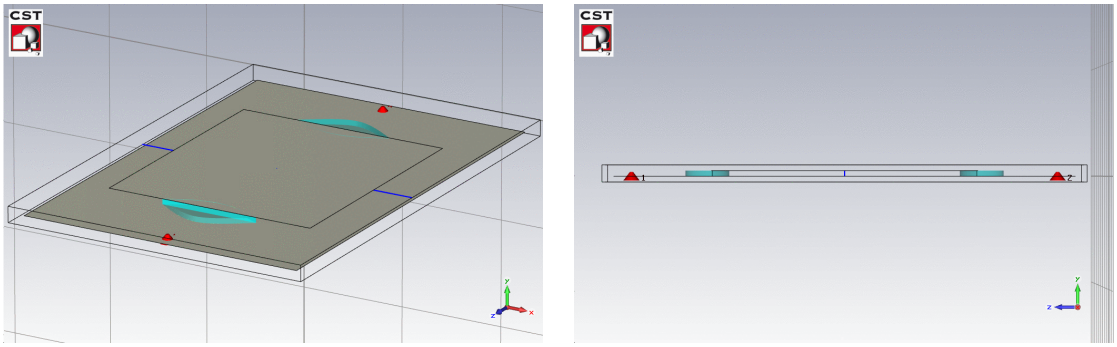

(a)

(b)

Figure 78. (a) Perspective and (b) side view of the 2D-focus beam measurement system model with 1 inch tall lenses.

For the system to be effective at simulating an incident plane wave, there must be an area of constant amplitude and phase at the focal plan that is larger than the samples to be tested. To determine the size of the quiet zone, the field strength and phase at the focal plane is examined. The quiet zone encompasses the area where the field is within 1 dB and 22.5° of the field at the center of the focal plane[18]. The system is also limited to operation below the cutoff frequency of the second mode of a parallel plate waveguide determined the height of the lenses. To illustrate this, two lens heights are simulated, 1 and 2 inches.

Both models are simulated using the CST MWS® time domain solver. The height of the simulated monopole is half of the lens height. The lenses are simulated as a dielectric with $\epsilon_r = 2.54$. The boundary conditions and additional space for the simulations are summarized in Table 10. To determine the quiet zone, the field is evaluated on a horizontal line across the center of the focal plane and on a vertical line down the center of the focal plane. The mesh statistics and solve times for both models of the 2D focus beam system can be found in Table 17 in Appendix A.

Table 10. 2D-Focus Beam Measurement System boundary conditions and spacing.

	Condition		Spacing from Edge (inches)	
Boundary Normal	Minimum	Maximum	Minimum	Maximum
x	Open	Open	2	2
y	PEC	Open (add space)	1	1
z	Open	Open	2	2

The normalized field magnitude and phase values for the 2D-focus beam measurement system with 1 inch lenses are shown in Figure 79. The frequencies of the field evaluations were selected to determine frequency regions with multiple propagating modes. For the field amplitude horizontal cut at 3 GHz, there is a non-gaussian shaped beam that is very wide. At the remaining frequencies, the main beam is gaussian shaped. Away from the main beam, there is additional ripple caused by diffraction. For the phase, there is a wide area of constant phase at 3 GHz, with smaller regions for the higher frequencies. For the vertical amplitude cut, there is a constant amplitude at 3, 5.9 and 6 GHz. Higher order modes are seen in the 6.5 and 11 GHz data. For the vertical phase cut, there is also higher order modes seen in the 6.5 and 11 GHz data, while there is constant phase in the 3, 5.9 and 6 GHz data. The size of the quiet zone is summarized in Table 11 for the system with 1 inch tall lenses.

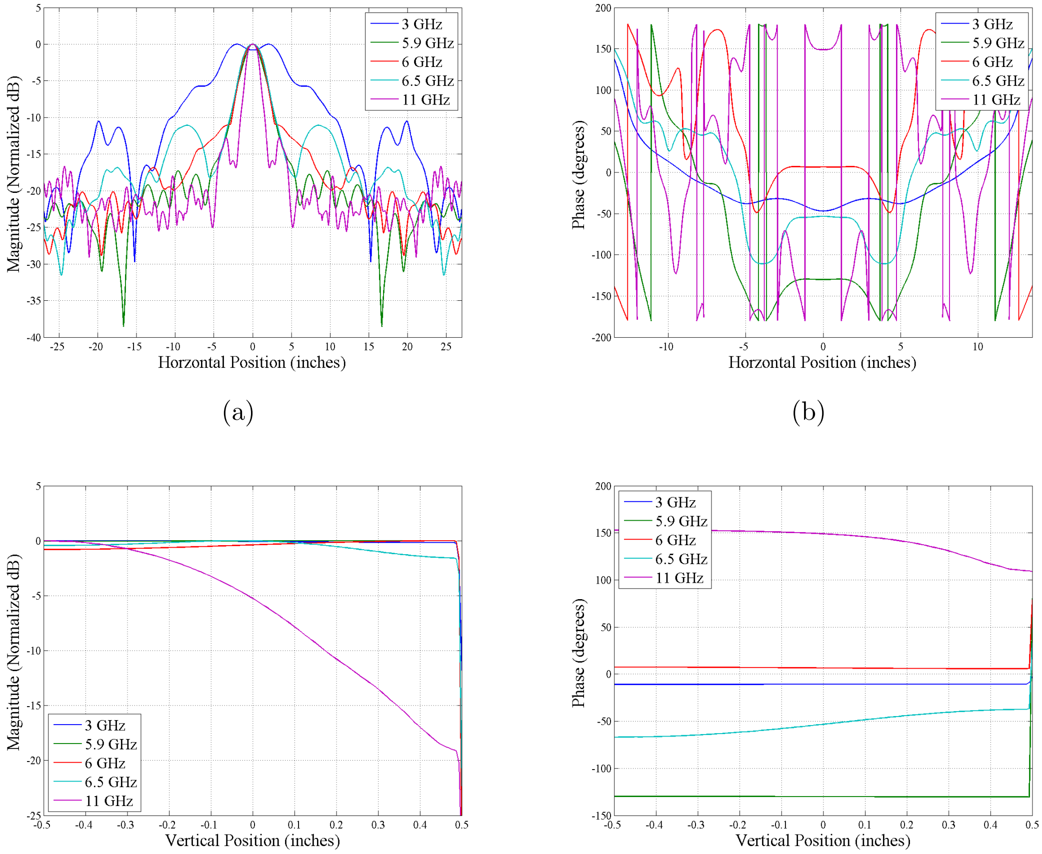

(a)

(b)

(c)

(d)

Figure 79. Simulated field results for the 2D-Focus Beam Measurement System with 1 inch tall lenses. Field (a) normalized magnitude and (b) phase for the horizontal cut shows a larger quiet zone for lower frequencies. Field (c) normalized magnitude and (d) phase for the vertical cut shows a full vertical quiet zone except at 11 GHz.

The normalized field magnitude and phase values for the 2D-focus beam measurement system with 2 inch lenses are shown in Figure 80. The same frequencies

Table 11. 2D-Focus Beam Measurement System quiet zone size with 1 inch tall lenses.

	Horizontal Cut		Vertical Cut	
Frequency (GHz)	Amplitude (in)	Phase (in)	Amplitude (in)	Phase (in)
3.0	7.3304	13.5477	1.0	1.0
5.9	1.4029	5.7497	1.0	1.0
6.0	1.6926	6.7245	1.0	1.0
6.5	1.9297	5.0779	1.0	1.0
11.0	1.1789	2.1537	0.0987	0.8421

examined for the 1 inch lenses are examined for the 2 inch lenses. The horizontal amplitude cut shows a wide non-gaussian main lobe. At the remaining frequencies, the main lobe appears gaussian. There is a large amount of ripple in the side lobes for frequencies other than 3 GHz caused by diffraction and the presence of multiple modes. For the phase, there is a wide area of constant phase at 3 GHz, with smaller regions at higher frequencies. For the vertical amplitude cut, there is constant amplitude for only the 3 GHz data, in contrast to the model with 1 inch lens height. Higher order modes are evident in the remaining frequencies. There is also constant phase in the 3 GHz cut, while the remaining frequencies show deviation. The size of the quiet zone is summarized in Table 12 for the system with 2 inch tall lenses.

Table 12. 2D-Focus Beam Measurement System quiet zone size with 2 inch tall lenses.

	Horizontal Cut		Vertical Cut	
Frequency (GHz)	Amplitude (in)	Phase (in)	Amplitude (in)	Phase (in)
3.0	3.2997	8.6345	2.0	2.0
5.9	1.3502	6.0395	0.4934	2.0
6.0	1.5873	5.9210	0.4408	2.0
6.5	1.3765	5.3282	1.4603	1.1513
11.0	1.0340	2.3776	0.7303	0.8289

The two dimensional focus beam system provides an alternate measurement approach to examine metamaterial samples. The system provides a vertically polarized TEM plane wave within the confines of the quiet zone. The linearly polarized TEM mode is needed to ensure the samples are stimulated appropriately to achieve their

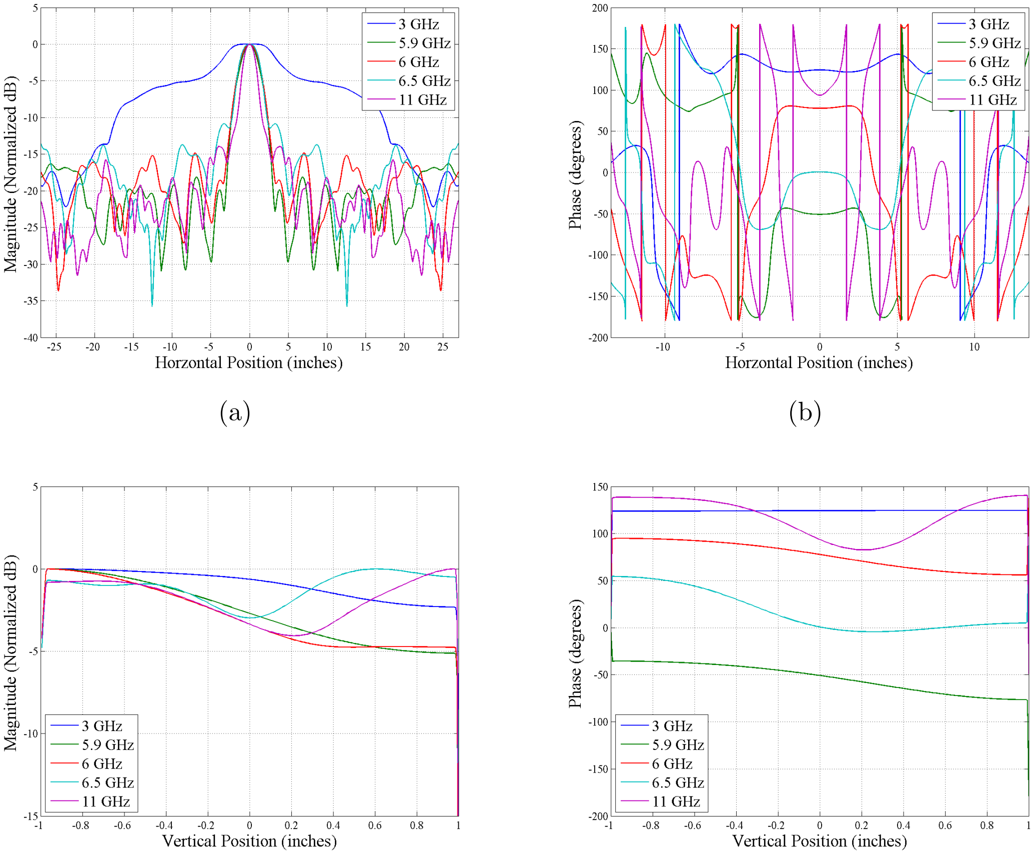

(a) (b)

(c) (d)

Figure 80. Simulated field results for the 2D-Focus Beam Measurement System with 2 inch tall lenses. Field (a) normalized magnitude and (b) phase for the horizontal cut shows a larger quiet zone for lower frequencies. Field (c) normalized magnitude and (d) phase for the vertical cut shows a full vertical quiet zone except at 11 GHz.

unique properties. A quiet zone is achievable for the two different lens heights. A balance must be made between vertical and horizontal sample size to ensure the quiet zone size is taken into account. Care must be taken to ensure that samples fit inside the quiet zone for the entire frequency range measured.

3.5 Simulation Summary

The previously presented model refinement process of the smaller AFIT designed metamaterial devices develops models to be used with a prediction aided measurement technique intended for exploring the complex field interactions involved with metamaterial devices. The model refinement process leads to simulated structures that produce far field results reasonably matching measured results and provide simulated field results representative of physical fields in measurements that cannot be directly quantified. Also, previously discussed simulations of the larger AFIT designed metamaterial devices allow for evaluation of current design options and lead to recommendations for future design iterations. Additionally, simulations of an alternate measurement method are presented previously, however the system is not fabricated, therefore no measurements are presented in the next chapter. In the next chapter, results from waveguide measurements of the metamaterial devices used in the prediction aided measurement process for the smaller devices are presented. Also, measurement results used to evaluate the larger devices are discussed.

IV. Experimental Results

4.1 Chapter Overview

The basic assumption of the prediction aided measurement technique developed in Chapter III is that the simulated field results from models of physical metamaterials will reflect the field interactions in the manufactured devices if the far field results match. In the previous chapter, representative models were created that result in S-parameters that reasonably match the measured behavior without capacitor values optimized for the simulated S-parameters to dispersively match the measured resonance regions. This chapter presents the far field data obtained through experimental waveguide measurements. Additionally, simulated far field results for optimized capacitance values are compared to measured data. The setup and measurement procedures are discussed first.

4.2 Stripline Measurement Procedures and Theory

While there are different methods accessible to measure S-parameters for a material sample, this thesis uses a network analyzer (NWA) to acquire the data. Here, the network analyzer connected to a stripline stimulates the sample with a stepped frequency sweep through a range of frequencies. The signal reflected from and transmitted through the sample are measured. Figure 81 shows the equipment used for this experiment. The network analyzer model is an Agilent E836B with a frequency range of 10 MHz to 20 GHz. The striplines used are the same striplines described in Sections 3.2.3.1 and 3.3.1, utilized depending on the expected resonance frequency and size of the samples tested.

The S-parameters of a network are the ratio of voltage waves and are defined in the frequency-domain. This research effort focuses on S_{11} and S_{21} because the

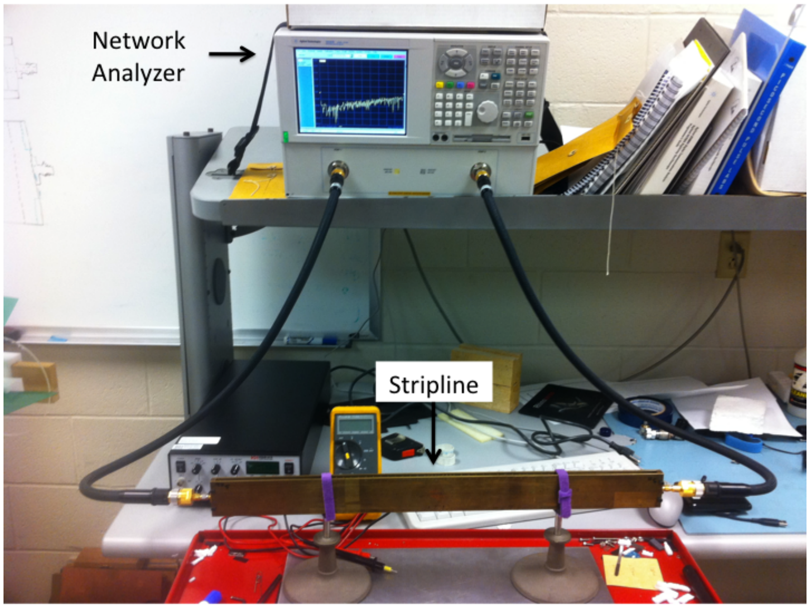

Figure 81. The network analyzer and 18 GHz stripline setup is common to all structures based on the 10 GHz design.

metamaterial samples produce the same results measured forward or backward in the stripline (i.e., $S_{22} = S_{11}$ and $S_{12} = S_{21}$). S_{11} and S_{21} are defined by the frequency-domain impulse voltage response received at port 1 (V_1^-), received at port 2 (V_2^-), and transmitted at port 1 (V_1^+) by [32]

$$S_{11}(f) = \frac{V_1^-(f)}{V_1^+(f)}, \tag{30a}$$

$$S_{21}(f) = \frac{V_2^-(f)}{V_1^+(f)}. \tag{30b}$$

Using a network analyzer in place of a Time Domain Reflectometer provides the S-parameters directly. The material parameters n, z, ϵ_r, and μ_r can be determined from the measured S-parameters, S_{11} and S_{21}. Preliminary stripline measurements used time domain gating alone to isolate the sample's response. Further measurements were calibrated using the 12-term error correction model detailed in [4]. The most accurate results were obtained using the 12-term error correction model as well as time domain gating. After the the error correction model is applied, the reflection and transmission of the sample, S_{11}^{sam} and S_{21}^{sam} are defined as [4]

$$S_{11}^{sam} = S_{11}^{nwa}, \tag{31a}$$

$$S_{21}^{sam} = S_{21}^{nwa} e^{jk_0 d_s}, \tag{31b}$$

where S_{11}^{nwa} and S_{21}^{nwa} are the reflection and transmission received by the network analyzer respectively, and d_s is the length of the material sample.

The basic procedure for taking stripline measurements for a material sample using the 12-term error correction model is:

1. calibrate the NWA with reflected and transmitted signal for the stripline in an empty configuration except for any sample holders,
2. calibrate the NWA with reflected and transmitted signal for an electrical short a known distance in front of the zero phase plane,
3. calibrate the NWA with reflected and transmitted signal for an electrical short at the zero phase plane,
4. calibrate the NWA with reflected and transmitted signal for an electrical short at the same known distance behind the zero phase plane,
5. measure reflected and transmitted signasl at the NWA for the stripline with the sample in place,
6. apply Equation (31) to calculate S_{11}^{sam} and S_{21}^{sam}.

4.3 AFIT Metamaterial Design Stripline Measurements

The measurements presented in this section are of the same adaptive metamaterial structure designed in [34] and modeled in Section 3.2.4. Without additional SRR gap capacitance, the device is designed to be resonant at 10 GHz. The physical structures are depicted in Figure 82. Figure 82(a) shows the unit cell structure while Figures 82(b) and 82(c) show the two types of physical cuts used to allow the cantilever structures to actuate. Structures to measure the capacitance of the cantilevers were not available for this set of devices.

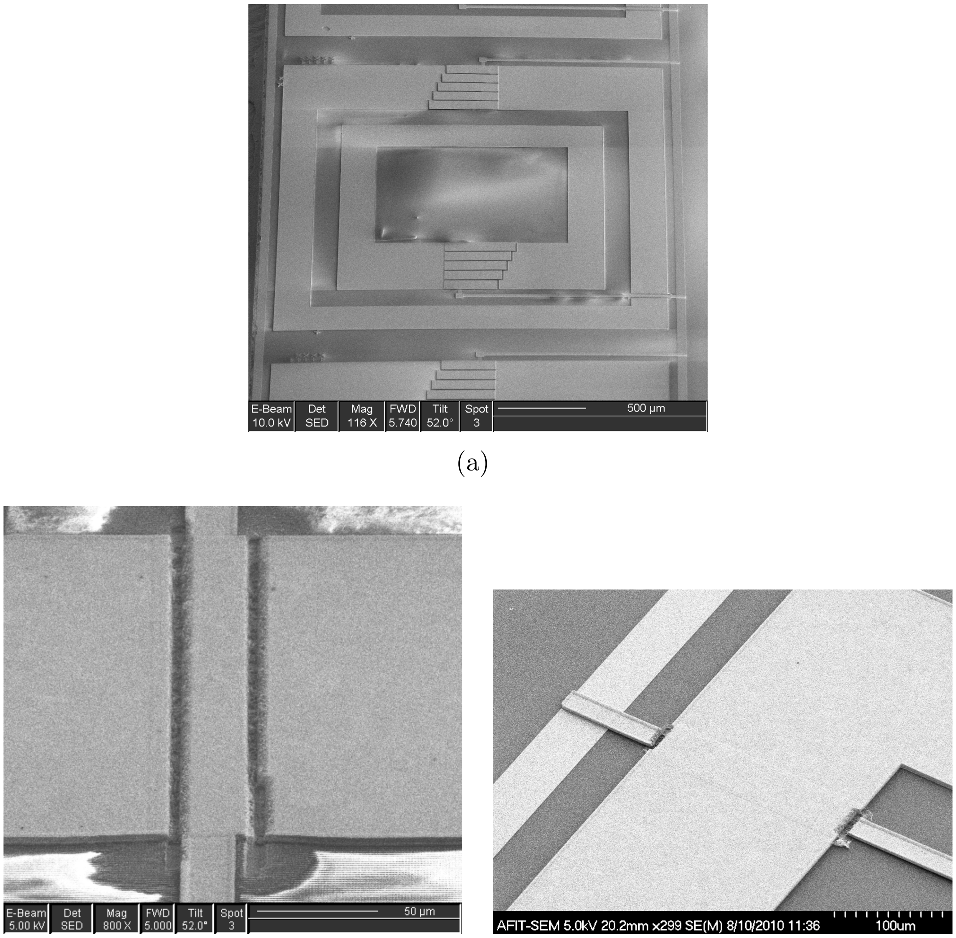

(a)

(b)

(c)

Figure 82. (a) The unit cell of the 10 GHz structures is shown with cuts across the outer SRR trace. (b) A close up view of the cuts across the outer SRR. (c) The other incision type cuts across the cantilever control trace.

4.3.1 Stripline Measurements of Passive Metamaterial.

To verify predictions of the baseline SRR structure, a structure of only concentric SRRs and wire traces on substrate material with expected resonance at 10 GHz was examined with stripline measurements. The sample is 17 unit cells long, the same length as the adaptive samples. Both measurement and simulation transmission results are shown in Figure 83. The measured resonance is seen at 10.32 GHz while the simulated resonance is seen at 10.19 GHz, a difference of only 0.13 GHz or 1.26%. With simulated resonance frequency locations validated with measurement results, adaptive metamaterial samples are next examined.

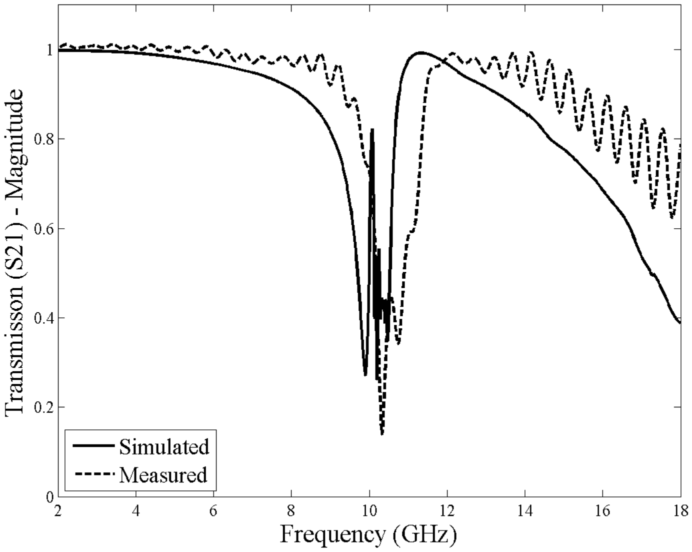

Figure 83. The simulated transmission for the 10 GHz baseline structure is shown with the solid line while the measured transmission is shown with the dashed line. The measured resonance is at 10.32 GHz while the simulated resonance is at 10.19 GHz, a difference of 0.13 GHz or 1.26% of the resonance frequency.

4.3.2 Preliminary Stripline Measurements of AFIT Adaptive Metamaterial.

Prior to taking measurements of the metamaterial sample, a time domain investigation is completed with an electrical short with a height of half that of the stripline at various locations of the stripline. Time domain gating is applied such that the S-parameter response is only from the region of the stripline containing the sample. The un-gated and gated time domain response for the half-short centered in the waveguide and at 70 mm from the center is shown in Figure 84. The structures are then placed in the stripline as shown in Figure 85 and excited with the network analyzer. As shown, there is a tilt in the measured sample. This tilt will perturb measurements, however it will not change the dispersive location of the resonance regions.

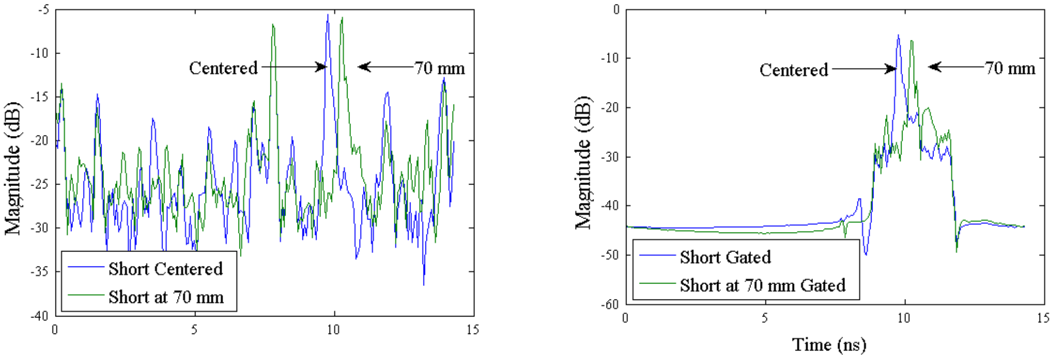

(a) (b)

Figure 84. The (a) un-gated and (b) gated time domain response of an electrical short with half the height of the waveguide. Time domain gating limits the response to the location where the sample will be placed in the waveguide.

As stated earlier, due to a fabrication issue, cuts need to be made in the samples to enable the cantilever beams to actuate. Two types of cuts are made. One type of incision cuts across the outer split ring, leaving the sets of cantilevers in the outer SRR gaps in the up position, while allowing the inner gap cantilevers to actuate. The

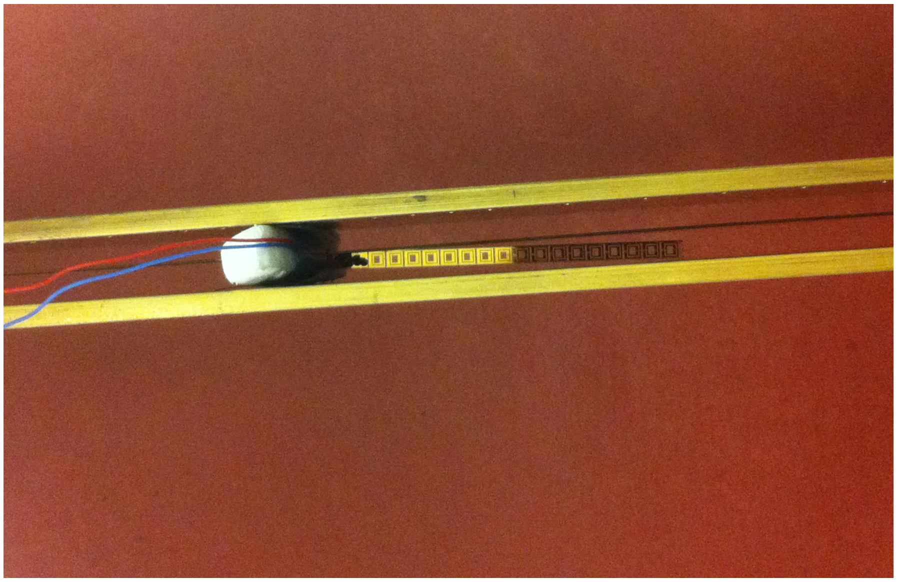

Figure 85. Experiment setup for stripline measurements of the 10 GHz AFIT metamaterial structures in the 18 GHz stripline.

other type cuts the inner cantilever control trace, leaving the sets of cantilevers in the inner SRR gaps in the up position, while allowing the outer gap cantilevers to actuate. At the time of the preliminary stripline measurements, only samples with cuts across the outer split ring were available for testing. Samples with both types of cuts are examined in following sections.

Figure 86 shows the S-parameter results from the measurements of the 17 cell long adaptive metamaterial strip as the applied voltage is increased from 0 to 40 volts, in 20 volt increments. At frequencies above 18 GHz there are multiple propagating modes in the waveguide, therefore results above 18 GHz should be discarded. With no applied voltage, the resonant frequency is 14.65 GHz. At 20 volts, the first cantilever pulls in and the resonant frequency is 14.3 GHz, a shift of 0.35 GHz. At 40 volts, two of the cantilevers have been actuated and the resonance shifts to 13.65 GHz for an overall shift of 1 GHz. While transitioning the applied voltage from 40 volts to 60 volts, the sample shorts out and is no longer usable for measurements.

An investigation into the repeatability of stripline S-parameter measurements is

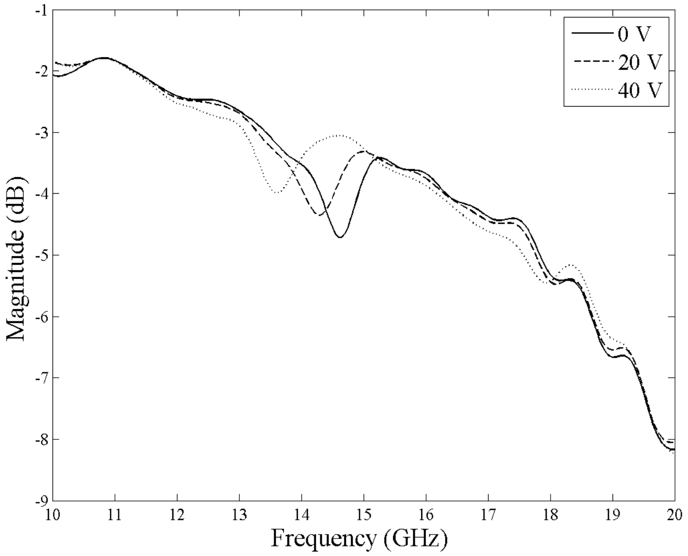

Figure 86. Measured transmission results for the AFIT adaptive metamaterial. With 0 volts applied, the resonant frequency is 14.65 GHz. At 20 and 40 volts applied, the resonant frequency is shifted by 0.35 GHz and 1 GHz respectively.

also carried out. The investigation takes place with a different sample because the previous sample examined is no longer an adaptive sample as the cantilevers are immobile. The voltage applied to the sample is varied from 0 volts to 60 volts. Measurements are taken for both increasing and decreasing voltage steps. The series of measurements is taken three times. Figure 87(a) shows the mean of the measurements for each applied voltage. Figure 87(b) shows the variance for each applied voltage. As seen, the variance is at least 10 dB lower than the average measurements.

4.3.3 Stripline Measurements of AFIT Adaptive Metamaterial using 12-Term Error Correction Model.

After stripline measurements of the adaptive metamaterial samples are taken using only time domain gating for error correction, the 12-term error correction model is applied to calibrate the measurement system. The measurement procedure outline in Section 4.2 is used to obtain the S-parameters of the sample. Figure 85 shows a

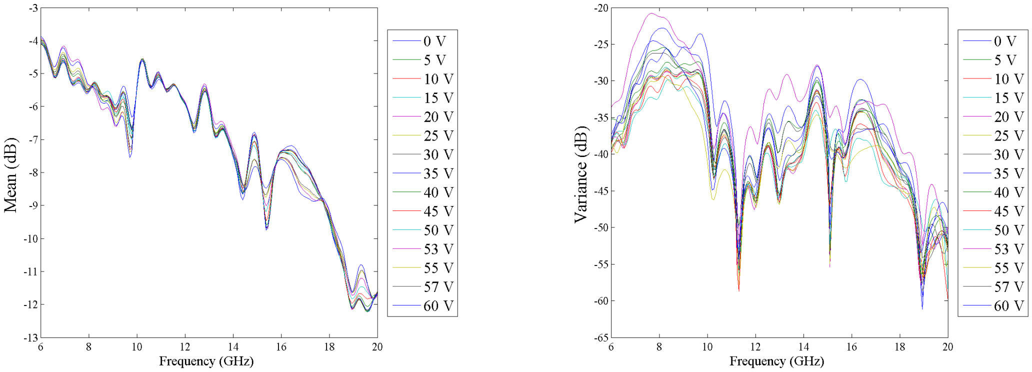

(a) (b)

Figure 87. The (a) mean and (b) variance of stripline transmission measurements of the AFIT adaptive metamaterial structure. The variance is at least 10 dB below the measured mean transmission.

metamaterial sample in the stripline. Samples with both types of cuts are examined.

4.3.3.1 Calibration.

After calibration of the NWA is performed, the calibration quality is examined by inspecting the transmission and reflection of the stripline containing only the sample holder. Figure 88 shows a quality calibration from 6 GHz to 18 GHz, with the transmission magnitude at 1 and the reflection magnitude at 0 as expected for an empty stripline.

4.3.3.2 Metamaterial Strips with Cuts Across Outer Split Ring.

Stripline measurements were taken at 0 volts applied and then taken at every 5 volts from 10 to 60 volts for the sample with cuts across the outer split ring. Figure 89 shows the measured transmission of the sample with cuts across the outer split ring, sampled at every 15 volts from 0 to 60 volts. Areas of resonance are seen around 8 and 14 GHz. The resonance frequency around 14 GHz is seen to shift as the applied voltage is increased, thereby increasing the split ring gap capacitance by pulling the

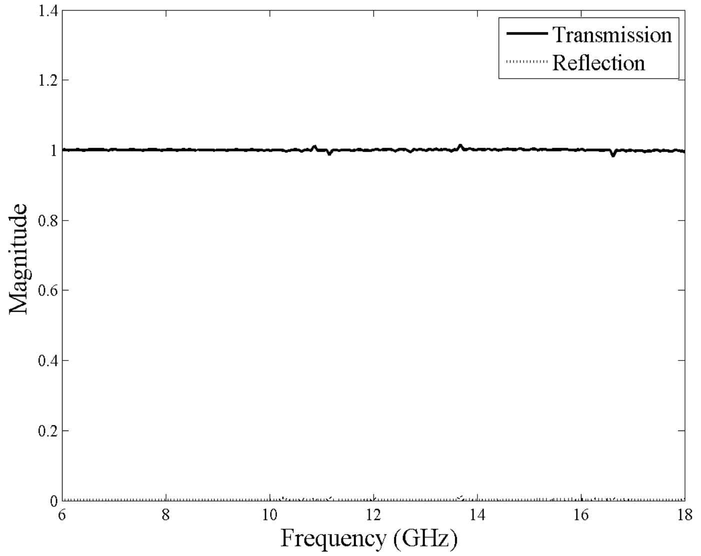

Figure 88. Measured transmission and reflection results for the empty calibrated 18 GHz stripline. As expected, the transmission magnitude is 1 while the reflection magnitude is 0.

cantilevers down. By 60 volts applied, all cantilevers are expected to be pulled down.

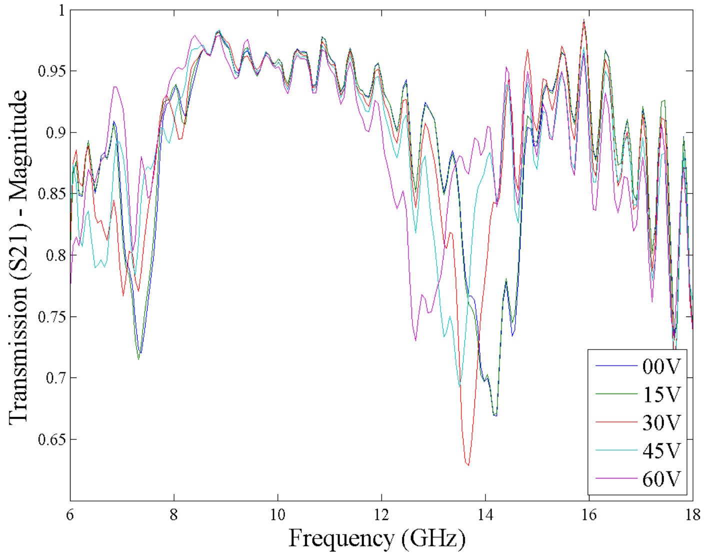

Figure 89. Measured transmission from AFIT metamaterial sample with cuts across the outer split ring sampled every 15 volts. Areas of resonance are seen around 8 and 14 GHz.

Figure 90(a) shows the resultant resonant frequency for each applied voltage and

Figure 90(b) shows the difference in resonance frequency from the 0 volts applied situation. The measured data shows the resonance frequency of the sample remaining constant until 20 volts are applied, then decreasing with increased voltage applied to the cantilever control lines. The difference in resonance frequency from the 60 volts applied situation to the original 0 volts applied case is 1.62 GHz or an 11.34% difference from the original resonance frequency.

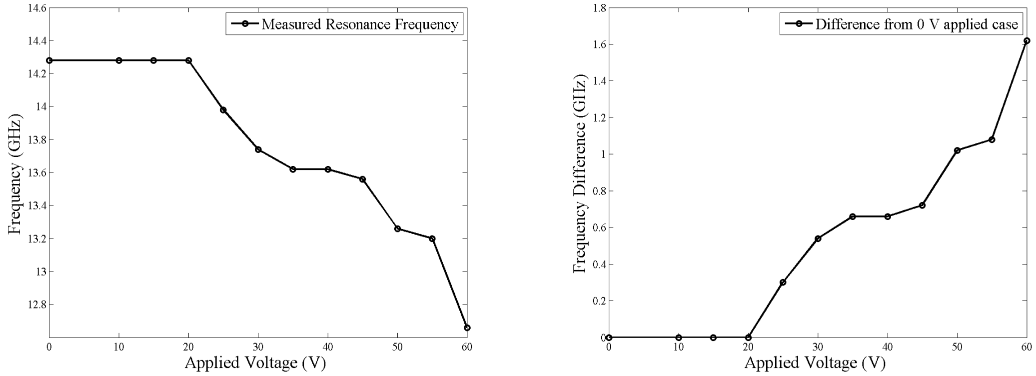

(a) (b)

Figure 90. Observed (a) resonance frequency and (b) difference from 0 volts applied case of the metamaterial strip with cuts across the outer split ring. As expected, the resonance frequency decreases with increase in applied control voltage.

The measured S-parameter data is compared to simulated S-parameter data in Figure 91. The simulation used the most realistic model created, having one 17 cell strip in the stripline with the metal particles, including the control line traces, modeled as gold instead of PEC. The simulations are described in Section 3.2.4.2. The capacitor values used in this model were based on the parallel plate model of the cantilever capacitors, calculated using Equation (29) and summarized in Table 4. The outer gap capacitors are modeled as a constant, C0, the value for all cantilevers in the up position. The inner capacitor is varied through all calculated capacitance values for the cantilevers actuating. As seen in Figure 91, C0 is too large of a capacitance value for the 0 volts applied case, while C1 is in the correct frequency area for the 60 volts applied case.

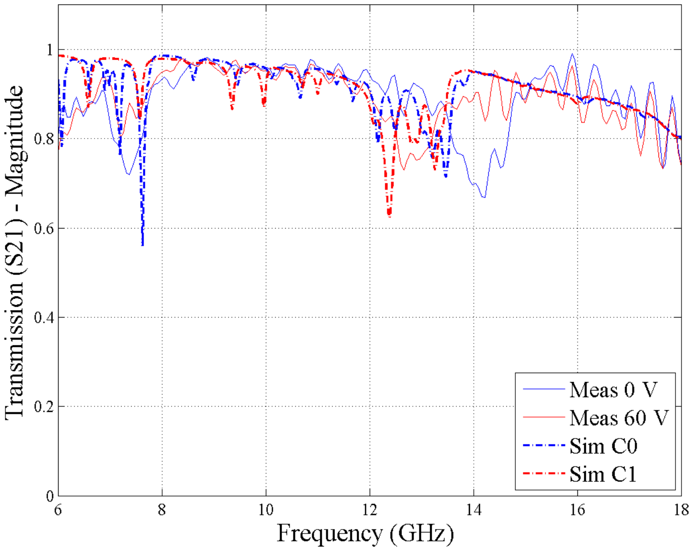

Figure 91. Measured stripline transmission compared to simulated stripline transmission of a 17 cell metamaterial strip with cuts across the outer split ring. Using calculated capacitance values for inner and outer capacitors leads to disagreement between measurement and simulation results.

With the simulations involving the calculated capacitor values leading to disagreement between measurements and simulations, the appropriate capacitance values are next determined. Optimizations were completed on the model described in Section 3.2.4.2. The model is fully refined from a single unit cell to the full length 17-cell column inside a simulated version of the physical stripline, with the metal structures modeled as gold in place of PEC. Based on optimizations that held both inner and outer capacitors to the same value, 0.1375 pF is chosen as the value for the non-actuating outer capacitors. This capacitance is consistent with cantilever beams curling up slightly. From there, the value of the inner capacitor is optimized to match the two resonance areas of the results.

The best optimization results for the transmission measurement and simulation comparison for the structure with the outer capacitor not able to actuate are shown in Figure 92. Figure 92(a) shows the comparison for the measurement with 0 volts applied while Figure 92(b) shows the comparison for the measurement with 60 volts applied. The 0 volts applied case is best matched with the value of the inner capacitor set to 0.2125 pF. The measured transmission null around 8 GHz is matched in the simulation by a set of nulls while the wide transmission null at 14 GHz is matched in the simulation by a wide transmission null. The 60 volts applied case is best matched with the value of the inner capacitor set to 3.3125 pF. The measured resonance around 13 GHz is matched by a set of two resonances, however the deepest simulated null is at a higher frequency than the measured data. The resonance areas seen in the measurements below 8 GHz are matched by shallower nulls at slightly greater frequencies. The 60 volts applied case may appear to be better matched in Figure 91, however the optimized simulations for the 0 volts applied case sets the value of the unchanging outer capacitor to 0.1375 pF. With the outer capacitor value set, the optimized capacitor is found to be slightly greater than the calculated C1 value.

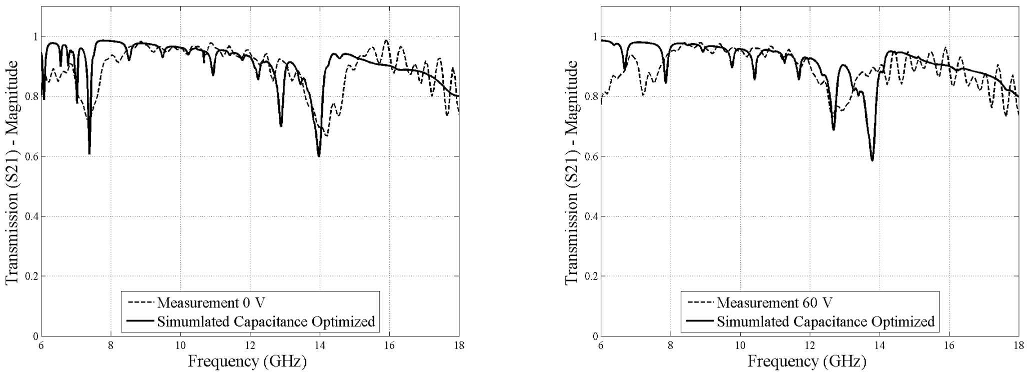

(a) (b)

Figure 92. Measurement and simulation comparison of samples with cuts across outer split ring, modeling optimized capacitance values. (a) The 0 volts applied case is best matched with the value of the inner capacitor set to 0.2125 pF. (b) The 60 volts applied case is best matched with the value of the outer capacitor set to 3.3125 pF. The inner capacitor is set to 0.1375 pF.

4.3.3.3 Metamaterial Strips with Cuts Across Control Trace.

A similar set of data was obtained for the sample with cuts across the cantilever control trace, however the applied voltage reached a maximum of 70 volts. Originally, data was obtained only over the frequency range of 6 to 18 GHz. Initial simulations not presented in this thesis using the calculated additional gap capacitance provided by the cantilevers did not show resonance outside of the 6 to 18 GHz frequency range. In an effort to maximize the number of meaningful data points, the smaller frequency range was used.

The measured transmission data from the 17 cell long metamaterial strip on the frequency range 6 to 18 GHz sampled every 15 volts applied is shown in Figure 93. The measured transmission does not show discernible resonance frequencies over the frequency range.

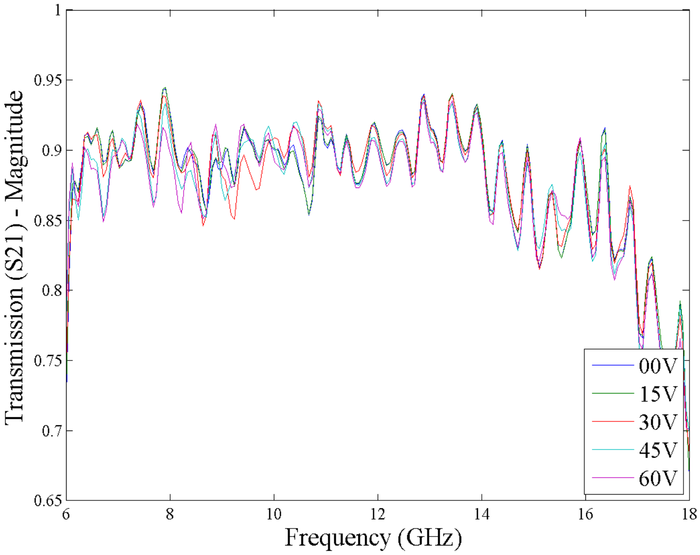

Figure 93. Measured stripline transmission of a 17 cell metamaterial strip with cuts across the cantilever control trace. There is no discernible resonance frequency seen over the frequency range. Also, there is very little difference between measured transmission for the different applied voltage measured.

The measurement data is also clouded by a ripple in the transmission data. The ripple is caused by constructive and destructive interference of at least two signals. The ripple can be mitigated by applying time domain gating to the measured S-parameter data. Stripline measurements using the 12-term error correction model and time domain gating are presented next.

4.3.4 Stripline Measurement of AFIT Adaptive Metamaterial using 12-Term Error Correction Model and Time Domain Gating.

In an effort to clarify the S-parameter data, stripline measurements of various samples were taken using the 12-term error correction model as well as time domain gating. Gating was applied at 2.5 ns on both sides of the zero phase plane, mitigating the frequency ripple seen in previous measurements while allowing for signals directly from the sample and signals from multiple interactions within the sample to be recorded by the NNA. Before measurements were obtained, the calibration of the measurement system was examined.

4.3.4.1 Calibration.

The stripline measurement system is calibrated using the calibration procedure outlined in Section 4.2. The calibration quality is evaluated by examining S-parameter data for a known standard. S-parameter data is taken for the stripline containing only the sample holder. The calibrated but non-gated reflection and transmission data is shown in Figure 94(a). The calibration is as expected for the majority of the frequency range with transmission at 1 and reflection at 0, however the calibration is not as accurate at lower frequencies. The calibration is improved by time domain gating, as seen in Figure 94(b). Based on the calibrated and gated empty stripline transmission and reflection data, the highest quality data is collected from 3 to 13 GHz. Over that frequency range, the average transmission and reflection for the un-gated empty stripline data are -0.0012 dB and -37.0477 dB respectively, and the average transmission and reflection for the gated data are -0.0002 dB and -37.3886 dB respectively. There is an improvement of 0.001 dB and 0.3409 dB in the transmission and reflection data respectively with the time domain gating applied.

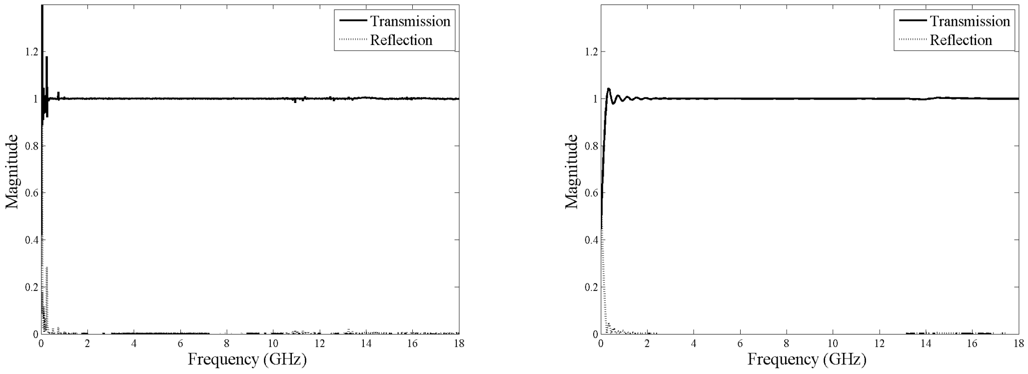

(a)

(b)

Figure 94. Reflection and transmission data for the empty 18 GHz stripline (a) calibrated without time domain gating and (b) calibrated with time domain gating. The calibration is improved with time domain gating, especially in the lower frequency range. The highest quality data is collected from 3 to 13 GHz.

4.3.4.2 Metamaterial Strips with Cuts Across Control Traces.

S-parameter data was obtained for a 17 cell metamaterial strip in the 18 GHz stripline measurement system. Data was taken for various applied voltages: 0 to 20 volts in increments of 5 volts and 22 to 34 volts in increments of 2 volts. Figure 95 shows the measured transmission data of the sample with cuts across the cantilever control traces. The consistent ripple in the data is suspected to stem from the edges of the time domain gate used. However, when examined, the ripple corresponds to objects separated in the time domain by 2.97 ns, which is smaller than the 5 ns width of the gate. The transmission data reveals two areas of shifting resonance around 5 and 8 GHz.

Figure 96(a) shows the measured transmission data magnified around the 5 GHz

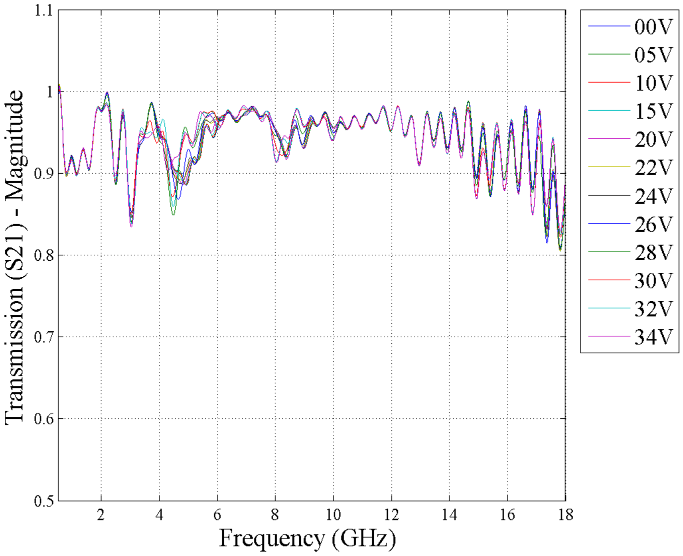

Figure 95. Measured transmission from AFIT metamaterial sample with cuts across the cantilever control traces. Areas of shifting resonance are seen around 5 and 8 GHz.

resonance. Figure 96(b) shows the computed resonance frequency for the 5 GHz area of resonance. As seen, the resonance frequency decreases only slightly from the location at 0 volts when applied voltage is increased to 15 volts. From 20 to 28 volts, the resonance frequency decreases more rapidly, reflecting the physics of the cantilevers puling down, thereby increasing the gap capacitance. The resonance frequency at 30 and 32 volts applied, do not follow the same trend, slightly increasing, rather than continuing to decrease. This deviation actually reflects the physics of the cantilevers. The pull down pad for the cantilevers is in the center of the cantilevers. As the cantilever center pulls down and touches on the dielectric, the voltage applied can pull the center of the beam further than the tip, allowing the tip to curl upward, decreasing the additional capacitance until enough voltage is applied to pull down the next cantilever. The maximum resonance frequency shift observed is 618 MHz or a 12.5% difference from the original 0 volts applied resonance frequency.

Figure 97(a) shows the measured transmission magnified around the 8 GHz res-

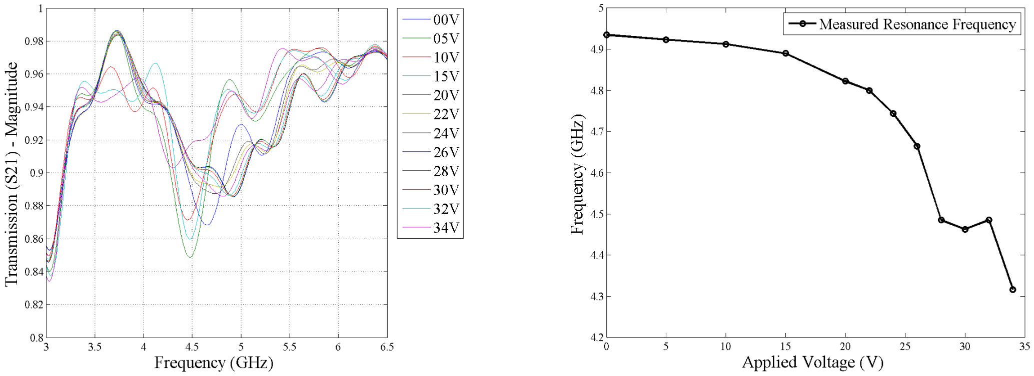

(a) (b)

Figure 96. (a)Magnified view of measured transmission around the 5 GHz resonance of the metamaterial sample with cuts across the cantilever control traces and (b) the computed resonance frequencies for each applied voltage. The resonance frequencies follow the physics of the cantilevers, rapidly decreasing from 15 to 28 volts, then slowing and increasing slightly, before decreasing again.

onance of the metamaterial sample with cuts across the cantilever control traces. Figure 97(b) shows the computed resonance frequency for the 8 GHz area of resonance. Similar to the 5 GHz region results, the resonance frequency changes only slightly from 0 to 15 volts applied, although above 15 volts, the resonance frequency only decreases slightly before it increases from 24 to 26 volts. From 28 to 32 volts, the resonance frequency decreases rapidly as another cantilever pulls down, before curling up at 34 volts, decreasing the additional gap capacitance slightly thereby increasing the resonance frequency slightly.

The difference between the voltage trends of the 5 and 8 GHz resonance frequencies highlight the non-uniformity of cantilever actuation across the 17 cells. Different cells in the strip can impact differently for the two resonance areas. If all cantilevers actuated uniformly, the resonance frequency trends would match for both resonance regions. For the 5 GHz region, enough cantilevers bend up to cause the resonance frequency to increase around 30 volts, while for the 8 GHz region, enough cantilevers bend up to cause the resonance frequency to increase around 24 volts. This non-uniformity emphasizes fabrication difficulties with MEMS devices.

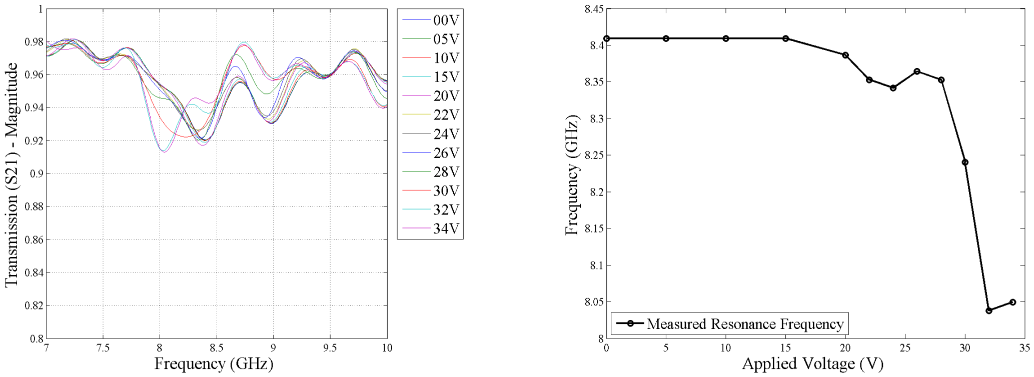

(a) (b)

Figure 97. (a)Magnified view of measured transmission around the 8 GHz resonance of the metamaterial sample with cuts across the cantilever control traces and (b) the computed resonance frequencies for each applied voltage. The resonance frequencies measured follows the physics of the cantilevers.

The measured S-parameter data is compared to simulated S-parameter data in Figure 98. The simulation used the most realistic model created, having one 17 cell strip in the stripline with metal particles, including the control line traces modeled as gold instead of PEC. The simulation is described in Section 3.2.4.1. The capacitance values used in this model were based on the parallel plate model of the cantilever capacitor, calculated using Equation (29) and summarized in Table 4. The inner gap capacitors are modeled as a constant, C0, the value for all cantilevers in the up position. The outer capacitor is varied through all calculated capacitance values for the cantilevers actuating. As seen in Figure 98, the C0 simulation is close for the 8 GHz resonance and had multiple transmission nulls in the region of the 5 GHz resonance band for the 0 volts applied case. The C1 simulation appears too large for the 8 GHz resonance of the 28 volt case. The C1 simulation does not show deep areas of resonance around 5 GHz. Additionally, above 14 GHz, there is too much ripple to make a meaningful comparison.

With the simulations involving the calculated capacitor values leading to disagree-

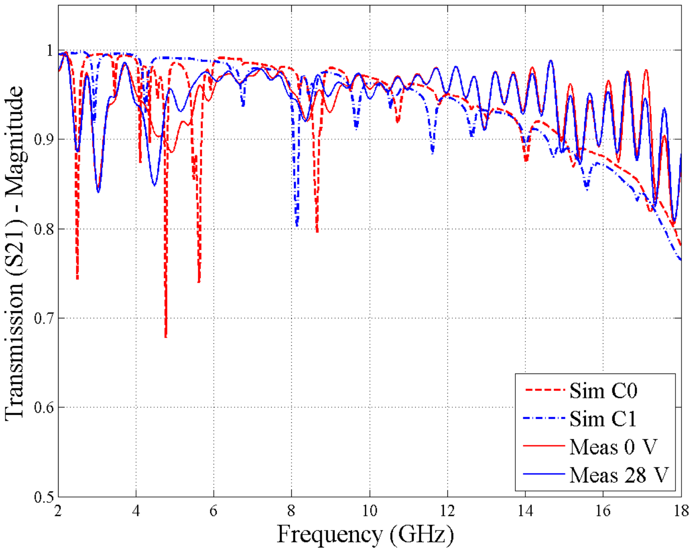

Figure 98. Measured stripline transmission compared to simulated stripline transmission of a 17 cell metamaterial strip with cuts across the cantilever control trace. Using calculated capacitance values for inner and outer capacitors leads to disagreement between measurement and simulation results.

ment between measurements and simulations, the appropriate capacitance values are next determined. Optimizations were completed on the model described in Section 3.2.4.1. The model is fully refined from a single unit cell to the full length 17-cell column inside a simulated version of the physical stripline, with metal structures modeled as gold in place of PEC. Based on the comparisons of simulated results to measured results, the value of the inner capacitor is chosen to be the calculated value for all the cantilevers in the un-actuated position, C0. From that starting point, the value of the outer capacitor is optimized to match the two resonance areas of the results.

The best optimization results for the transmission measurement and simulation comparison for the structure with the inner capacitor not able to actuate are shown in Figure 99. Figure 99(a) shows the comparison for the measurement with 0 volts applied while Figure 99(b) shows the comparison for the measurement with 28 volts applied. The 0 volts applied case is best matched with the value of the outer capacitor set to 0.195456 pF or the calculated value for the all the cantilevers in the un-actuated position. The wide transmission null around 5 GHz in the measurement is matched in the simulation by a set of transmission nulls. The set of two shallower transmission nulls at 9 GHz in the measurements is matched in the simulation by a single deeper transmission null. The 28 volts applied case is best matched with the value of the outer capacitor set to 1.5 pF. The deep null at 5 GHz seen in the measurement is matched with a shorter null in simulations. The null around 8 GHz observed in the measurements is matched with a deep null in the simulation results.

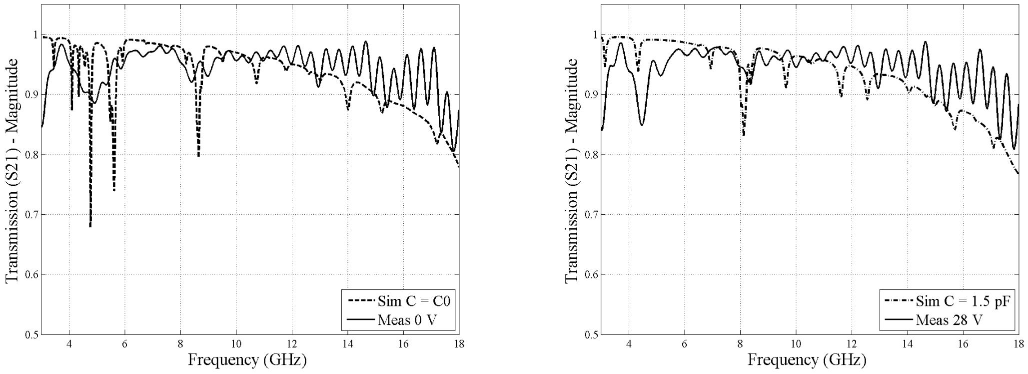

(a) (b)

Figure 99. Measurement and simulation comparison of samples with cuts across control traces, modeling optimized capacitors. (a) The 0 volts applied case is best matched with the value of the outer capacitor set to 0.195456 pF or the calculated value for the all the cantilevers in the un-actuated position. (b) The 28 volts applied case is best matched with the value of the outer capacitor set to 1.5 pF. The inner capacitor is set to C0.

4.3.5 AFIT Metamaterial Design Stripline Measurements Conclusions.

Despite optimization efforts, the simulation results do not exactly match the measurement results. The simulations do not take into account the actual geometry of the cantilever structures, using lumped element capacitors in their place. The cantilever structures of the physical devices are not simulated in the models. The accurate models of the cantilevers lead to extreme simulation durations. Models of a single set of cantilevers take multiple days to simulate. Fabrication issues with the MEMS devices also lead to simulation difficulties. The cantilever structures do not actuate uniformly, leading to different values for each capacitor modeled. Performing optimization for all 34 capacitors would not be feasible in a timely manner. The variance of the capacitor values can also lead to widening of transmission nulls, while decreasing the null depth. Modeling the samples as fabricated, rotated and with cuts, leads to more complicated results. The simulation results are more in agreement with measurements, however the inability to optimize all capacitor values limits the accuracy of the optimization. With the difficulties of simulating the actual physical structures, the optimized best fit capacitance values are actually average effective capacitor values, not exact values.

For the 17-Cell structure with cuts across the inner cantilever control traces, the optimization procedure produced an average effective capacitance value of 0.195456 pF for the inner capacitors at all voltage levels and average effect capacitance values for the outer capacitors of 0.195456 pF and 1.5 pF for the 0 volts and 28 volts applied cases respectively. The measured resonance frequency shifts 618 MHz or a 12.5% difference from the original resonance frequency.

For the 17-Cell structure with cuts across the outer split ring, the optimization procedure produced an average effective capacitance value of 0.1375 pF for the outer capacitors at all voltage levels and average effective capacitance values for the inner capacitors of 0.2125 pF and 3.3125 pF for the 0 volts and 60 volts applied cases respectively. The measured resonance frequency changes 1.62 GHz or an 11.34% difference from the original resonance frequency.

4.4 Larger AFIT Metamaterial Design Stripline Measurements

The measurements present in this section are of the same adaptive metamaterial structure modeled in 3.3. Without additional SRR gap capacitance, the device is designed to be resonant around 3 GHz.

4.4.1 Stripline Measurement of Larger AFIT Adaptive Metamaterial using 12-Term Error Correction Model.

Stripline measurements of the adaptive metamaterial samples were taken using the 12-term error correction model to calibrate the measurement system. The measurement procedure outlined in Section 4.2 is used to obtain the S-parameters of the sample. Figure 100 shows a metamaterial sample in the stripline.

Figure 100. Experiment setup for stripline measurements of the 3 GHz AFIT metamaterial structures in the 4 GHz stripline.

4.4.1.1 Calibration.

After calibration of the NWA is performed, the calibration quality is examined by inspecting the transmission and reflection of the stripline containing only the sample holder. As expected, the transmission data was at 0 dB, with the reflection data at least 40 dB below the transmission data, a near zero reflection. The calibration was deemed sufficient and measurements of adaptive metamaterial samples were obtained.

4.4.1.2 Stripline Measurements of Larger Passive Metamaterial.

To verify predictions of the baseline SRR structure, a structure of only concentric SRRs and wire traces on substrate material with expected resonance at 3 GHz was examined with stripline measurements. The sample is 4 unit cells long, the same length of the adaptive samples. Both measurements and simulation transmission results are shown in Figure 101. The measured resonance is seen at 2.88 GHz while the simulated resonance is seen at 2.82 GHz, a difference of only 0.06 GHz or 2.1%. With simulated resonance frequency locations validated with measurement results, adaptive metamaterial samples are next examined.

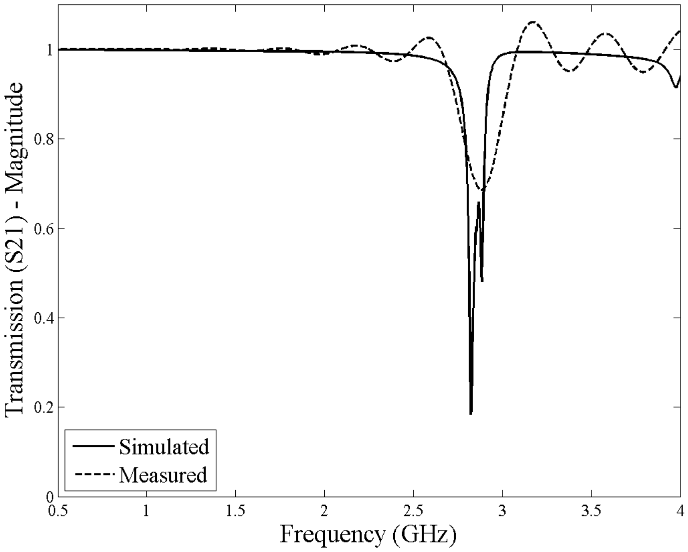

Figure 101. The simulated transmission for the 3 GHz baseline structure is shown with the solid line while the measured transmission is shown with the dashed line. The measured resonance is at 2.88 GHz while the simulated resonance is at 2.82 GHz, a difference of 0.06 GHz or 2.1% of the resonance frequency.

4.4.1.3 Capacitor Layout A.

The first of the 3 GHz adaptive metamaterial structures is fabricated similarly to the 10 GHz structure, with sets of cantilevers in the gaps of both inner and outer split rings, as modeled in Section 3.3.2. This layout is referred to as capacitor layout A. The design issue from the 10 GHz design that required cuts across either the outer split ring or the control line traces to allow the cantilevers to actuate has been resolved in the 3 GHz structures, therefore all sets of cantilevers are free to actuate with applied voltage.

The stripline measurements were taken at 0 volts applied then at every 5 volts from 10 to 25 volts, where the sample shorted out. The measured transmission data from the 3 GHz sample with capacitor layout A is shown in Figure 102(a). Figure 102(b) shows the measured transmission magnified about the resonance frequency. Above 2 GHz, the measured transmission is unphysical, with results above 1. For this measurement the data above 2 GHz should be disregarded. The resonance is seen to shift from 1.20 GHz at 0 volts applied to 0.93 GHz at 25 volts applied, a difference of only 0.27 GHz. The small shift is due to the small range of voltages applied. The sample shorted just as the first cantilever would be touching down.

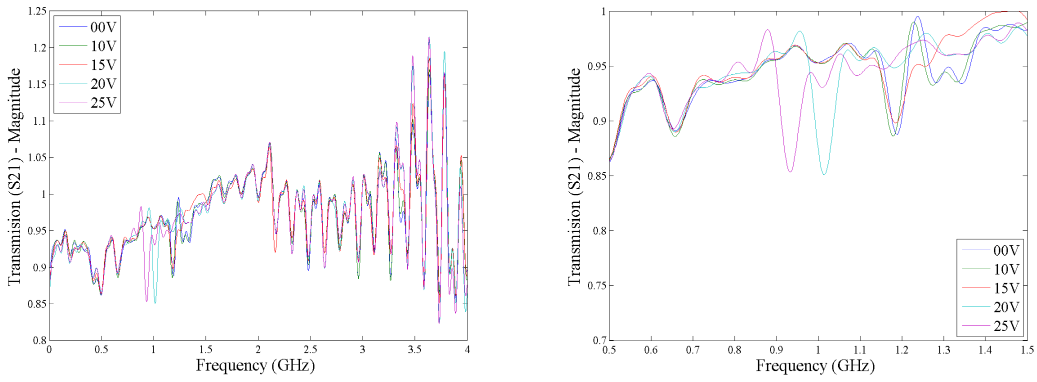

(a) (b)

Figure 102. (a)Measured transmission from larger AFIT metamaterial sample with capacitor layout A (split ring gap capacitors) over the entire frequency range measured. (b)Measured transmission magnified around resonance frequency. An area of shifting resonance is seen around 1 GHz.

Figure 103 shows the measured transmission compared to the simulated transmission for capacitance values calculated based on the cantilever geometry. The comparison shows that simulating C0 for the 0 volts case is too small, while simulating C2 for the 25 volt case is too large.

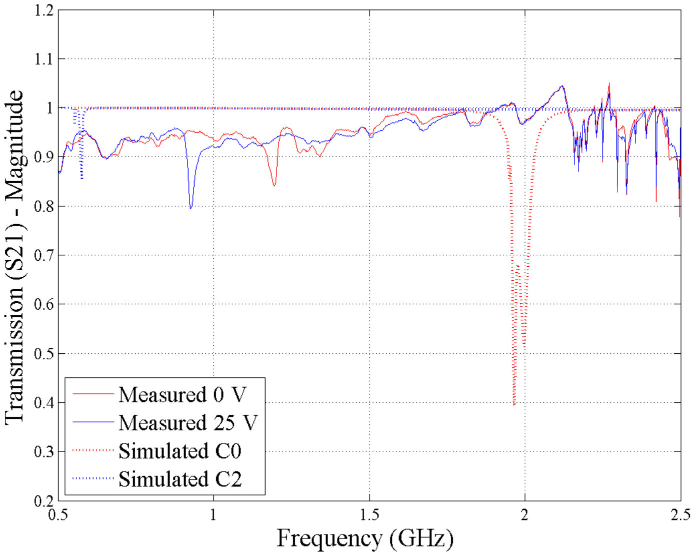

Figure 103. The simulated transmission for the 3 GHz structure with capacitor layout A is shown with the dotted line while the measured transmission is shown with the dashed line. Simulating C0 for the 0 volts case is too small, while simulating C2 for the 25 volt case is too large.

With the simulations involving the calculated capacitor values leading to disagreement between measurements and simulations, the appropriate capacitance values are next determined. Figure 104 shows the measured transmission compared to the simulated transmission for capacitance values selected to achieve the measured resonance frequencies. Simulations and measurements show agreement with capacitors equal to 0.85 pF for the 0 volt case and 1.5 pF for the 25 volt case, with a difference of 0.0070 GHz and 0.0088 GHz from the measured resonance frequency respectively. The capacitance value simulated for the 0 volt situation implied that the cantilevers are slightly closer than expected. The capacitance value simulated for the 25 volt case implies that only one cantilever is close to touching down completely.

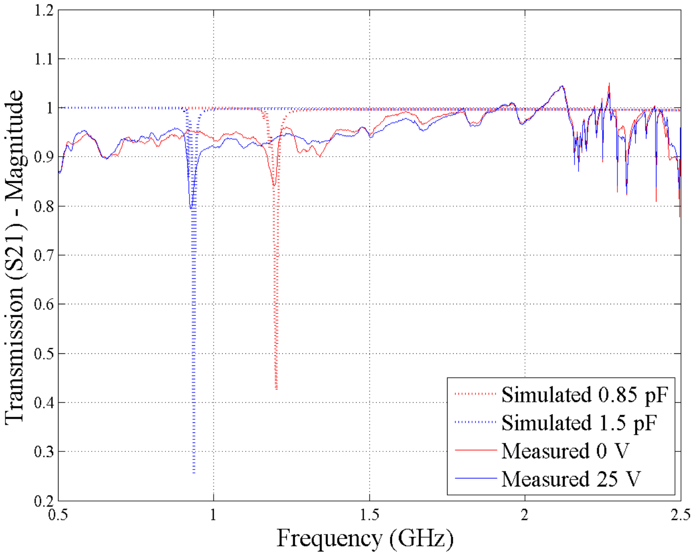

Figure 104. The simulated transmission for the 3 GHz structure with capacitor layout A is shown with the dotted line while the measured transmission is shown with the dashed line. Capacitance values were selected to achieve the measured resonance frequencies. Simulations and measurements show agreement with capacitors equal to 0.85 pF for the 0 volt case and 1.5 pF for the 25 volt case.

4.4.1.4 Capacitor Layout C.

The second variant of the 3 GHz structure to be examined has two sets of cantilevers on each side of the cell between the inner and outer split rings, providing additional intra-ring capacitance but not additional gap capacitance, as modeled in Section 3.3.4. The sample is 4 cells long. This layout is referred to as capacitor layout C.

The stripline measurements were taken at 0 volts applied then at every 5 volts from 10 to 35 volts, where the sample shorted out. The measured transmission data from the 3 GHz sample with capacitor layout C is shown in Figure 105(a). The frequency range above 2 GHz shows some type of measurement contamination evident in large oscillations in the measured transmission. For this measurement, the data above the 2 GHz area should be disregarded. Transmission nulls are seen around 1 and 2 GHz, however no shifting is seen.

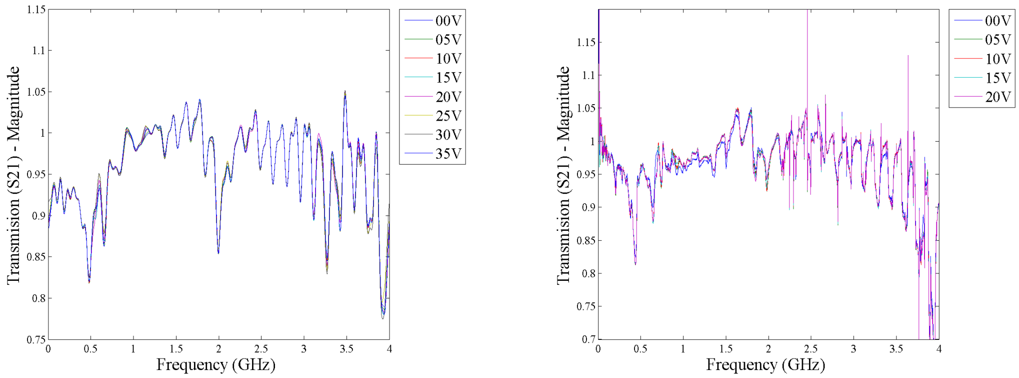

(a) (b)

Figure 105. Measured transmission from two larger AFIT metamaterial samples with capacitor layout C (two intra-ring cantilever sets per side). (a) Transmission nulls are seen around 1 and 2 GHz however no shifting is observed. (b) Slight changes are seen around 1 GHz, however no appreciable shift is seen.

A second set of transmission measurements was taken on a different sample with capacitor layout C. Measurements were taken in increments of 5 volts applied from 0 to 20 volts, where the sample shorted. The measurements are shown in Figure 105(b). Above 2 GHz the measurements are again clouded by large oscillations and should be disregarded. Despite no resonance shift being seen, these measurements highlight the need to include time domain gating in the stripline measurements to ensure only responses from the sample are recorded which will also eliminate the large oscilations above 2 GHz.

4.4.1.5 Capacitor Layout D.

The next variant of the 3 GHz structure to be examined has a set of cantilevers in each of the split ring gaps as well as two sets of cantilevers on each side of the cell between the inner and outer split rings, as modeled in Section 3.3.5. The layout combines capacitor layouts A and C. This combination layout will be referred to as capacitor layout D. The sample is 4 unit cells in length.

The stripline measurements were taken at 0 volts applied then at every 5 volts from 10 to 40 volts, where the sample shorted out. The measured transmission data from the 3 GHz sample with capacitor layout D is shown in Figure 106(a). A large oscillation is present in the transmission data above 2 GHz, therefore data above 2 GHz should be disregarded. Transmission nulls are seen around 0.5 GHz and just below 2 GHz. The transmission data does not change with applied voltage at the 0.5 GHz transmission null, however there are changes at the 2 GHz transmission data. As seen in Figure 106(b), even with the changes at the 2 GHz transmission data, no appreciable null shift is seen, only a slight decrease in the transmission amplitude. In this region, the calibration appears poor, with transmission measurements above 1, a non-physical result. The need to include time domain gating in the measurement procedures is again highlighted.

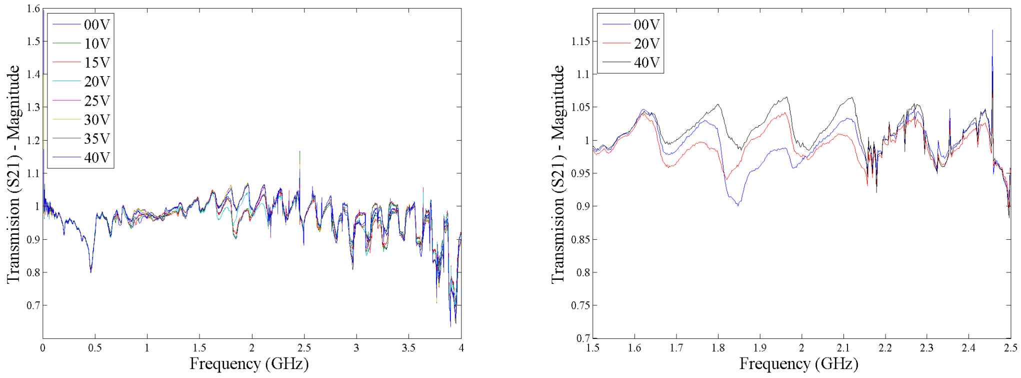

(a) (b)

Figure 106. Measured transmission from a larger AFIT metamaterial sample with capacitor layout D (a) over the entire frequency range and voltage set measured and (b) magnified around the 2 GHz resonance region for voltages of 0, 20 and 40 volts. The 0.5 GHz transmission null does not change with applied voltage, however the 2 GHz transmission data does change with applied voltage. Even with the changes, there is no appreciable null shift seen, only a slight decrease in amplitude.

4.4.1.6 Capacitor Layout E.

The final variant of the 3 GHz structure to be examined without time domain gating has three sets of cantilevers on each side of the cell between the inner and outer split rings, as modeled in Section 3.3.6. The sample is a 4 cell column.

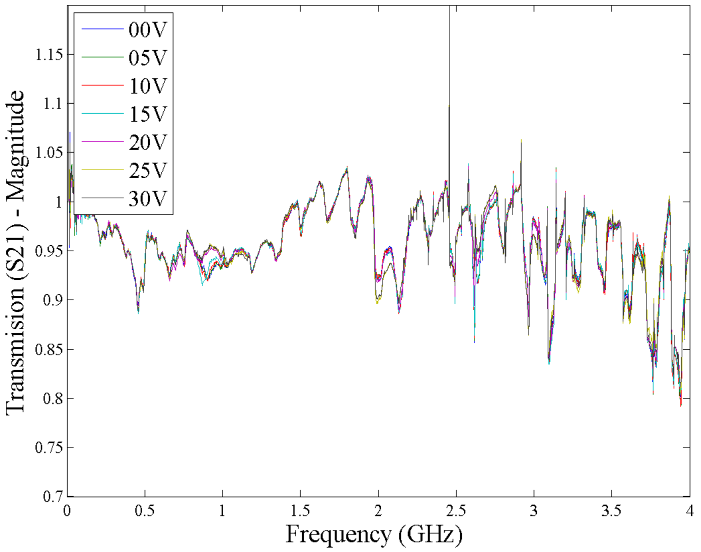

Figure 107. Measured transmission from a larger AFIT metamaterial sample with capacitor layout E. While changes with applied voltage are evident around 1 and 2 GHz, the clouded transmission data does not allow for conclusions.

The stripline measurements were taken at 5 volt increments from 0 to 30 volts. The measured transmission data from the 3 GHz sample with capacitor layout E is shown in Figure 107. A large oscillation is present in the transmission data above 2 GHz leading to that data being disregarded. Changes with applied voltage are seen around 1 and 2 GHz. While changes are seen, no conclusions are to be made with the clouded data.

The transmission data collected using only the 12-term error correction model for calibration does not allow conclusions to be made for capacitor layouts C, D, and E. To improve calibration of the system, for the remaining measurements the 12-term error correction model and time domain gating is applied to the S-parameter measurements.

4.4.2 Stripline Measurement of Larger AFIT Adaptive Metamaterial using 12-Term Error Correction Model and Time Domain Gating.

In an effort to clarify the S-parameter data, stripline measurements of various samples were taken using the 12-term error correction model as well as time domain gating. Additionally, the results presented here are from different samples because the previous structures shorted out during the testing process. Gating was applied at 2.5 ns on both sides of the zero phase plane, mitigating the frequency ripple seen in previous measurements while allowing for signals directly from the sample and signals from multiple interactions within the sample to be recorded by the PNA. Before measurements were obtained, the calibration of the measurement system is examined.

4.4.2.1 Calibration.

The stripline measurement system is calibrated using the calibration procedure outlined in Section 4.2. The calibration quality is evaluated by examing S-parameter data for a known standard. S-parameter data is taken for the stripline containing only the sample holder and for the stripline containing a short at the zero phase plane. The calibrated but non-gated reflection and transmission data is shown in Figure 108(a) for the stripline containing only the sample holder. The calibration is as expected for the majority of the frequency range with transmission at 1 and reflection at 0, however the magnitude is larger than expected at lower frequencies. There are also spurious results above 2.5 GHz for both transmission and reflection. As seen in Figure 108(b), these erroneous results are correct by applying time domain gating.

The calibration quality for a second known standard is also examined by taking

S-parameter measurements with an electrical short placed at the zero phase plane of the system. The calibrated by non-gated reflection and transmission data is shown in Figure 108(c) for the stripline containing only an electrical short at the zero phase plane of the measurement system. The results are as expected for the majority of the frequency range with transmission at 0 and reflection at 1, however at frequencies above 2 GHz there are spurious results for both reflection and transmission. The calibration is improved by applying time domain gating, as seen in Figure 108(d). Based on the calibrated and gated S-parameter data for the empty and short standards, the highest quality data is collected from 0.5 to 4 GHz. Over that frequency range, the average transmission and reflection for the un-gated empty data are -0.00063 dB and -41.6706 dB respectively, and the average transmission and reflection for the gated empty data are -0.000171 dB and -42.0452 dB respectively. For the empty data, there is an improvement of 0.000459 dB and 0.3746 dB for the transmission and reflection data with the time domain gating applied. Also, the average transmission and reflection for the un-gated short data are -26.4732 dB and 0.0040 dB, and the average transmission and reflection for the gated short data are -27.5807 dB and -0.0016 dB respectively. For the short data, there is an improvement of 1.1075 dB and 0.0024 dB for the transmission and reflection respectively.

4.4.2.2 Capacitor Layout A.

The first 3 GHz variant to be examined using the 12-error correction model and time domain gating for calibration is fabricated with capacitor layout A, as simulated in Section 3.3.2 and previously examined using only the 12-term error correction model for calibration.

The stripline measurements were taken at 0 volts applied and then at every volt from 5 to 21 volts. The measured transmission data from the 3 GHz sample with

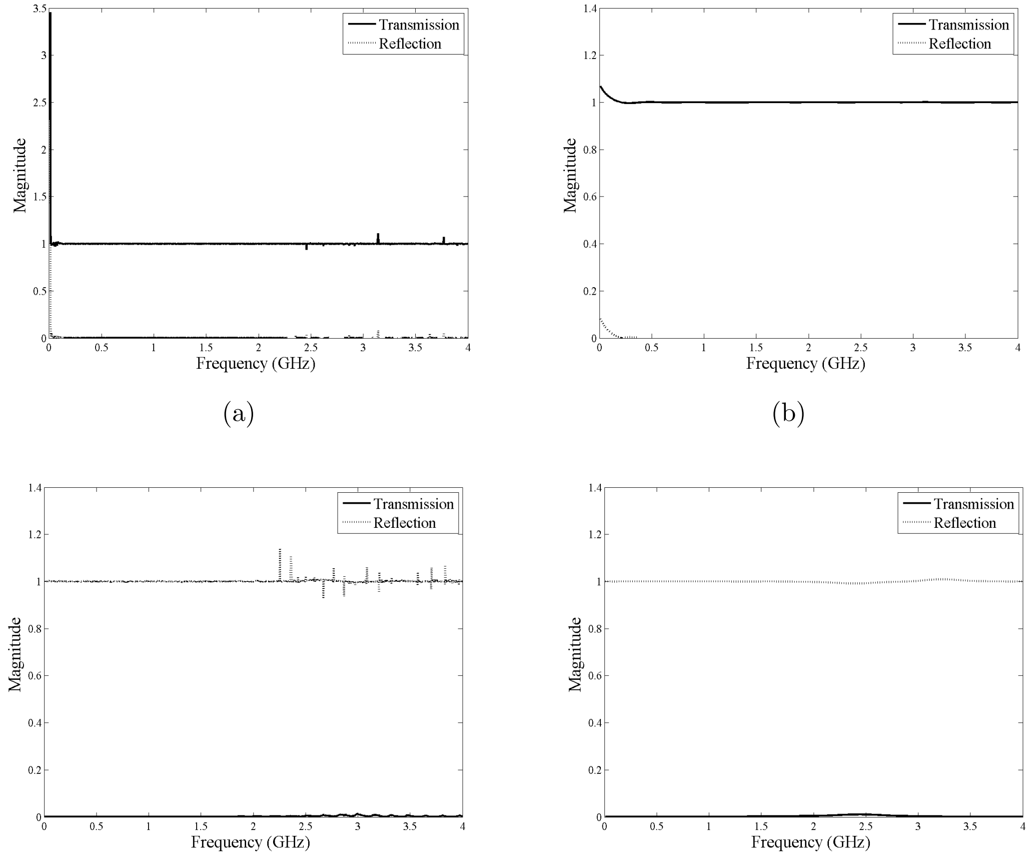

(a) (b)

(c) (d)

Figure 108. Reflection and transmission data for the empty 4 GHz stripline (a) calibrated without time domain gating and (b) calibrated with time domain gating for the stripline containing only the sample holder and (c) calibrated without time domain gating and (d) calibrated with time domain gating for the stripline containing only an electrical short at the zero phase plane. The calibration is improved with time domain gating, especially in the frequency range from 2 to 4 GHz. The highest quality data is collected from 0.5 to 4 GHz.

capacitor layout A is shown in Figure 109(a). A region of shifting resonance is seen around 2 GHz. Figure 109(b) shows the measured transmission magnified around the 2 GHz area. The resonance is seen to shift from 1.98 GHz at 0 volts applied to 1.89 GHz at 21 volts applied, a difference of only 0.11 GHz or 5.5% of the original resonance frequency. The small shift is due to the small range of voltages applied. In the interest of sample preservation, the range of applied voltages was limited to under 22 volts, as previous samples with capacitor layout A shorted at 25 volts.

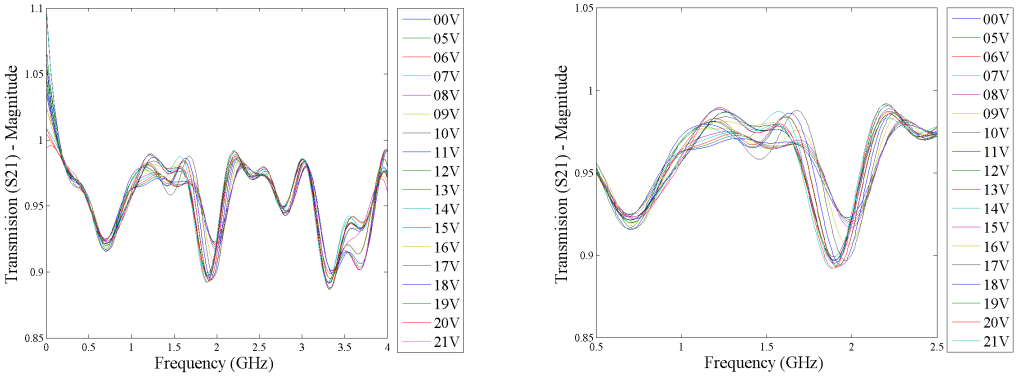

(a) (b)

Figure 109. (a) Measured transmission calibrated including time domain gating from larger AFIT metamaterial sample with capacitor layout A (split ring gap capacitors) over the entire frequency range measured. (b)Measured transmission magnified around resonance frequency. An area of shifting resonance is seen around 1 GHz.

The measured resonance frequency follows the physics of the cantilevers pulling into position, as seen in Figure 110. The measured resonance frequency reflects one cantilever already down at 0 volts and curling up as the voltage is increased until 8 volts when the next cantilever is pulled down far enough to add appreciable capacitance, thereby causing the resonance frequency to shift rapidly down until 15 volts where the second beam appears to curl up. The resonance frequency remains around 1.9 GHz until 20 volts where the resonance frequency begins trending downwards.

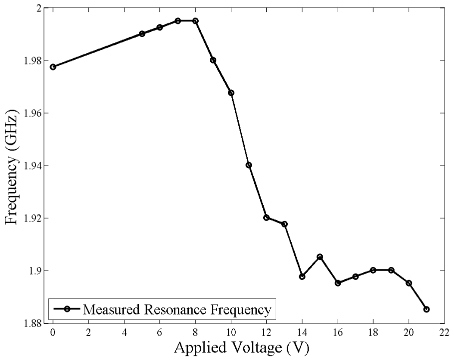

Figure 110. Observed resonance frequency of 3 GHz metamaterial sample with capacitor layout A. As expected, the resonance frequency decreases with increase in applied control voltage.

The resonance frequency results show how thickness of the cantilevers plays a large role in the uniformity of additional capacitance. The thin cantilevers used in samples up to this point lead to non-uniform distance between the cantilever and the dielectric, even at 0 volts applied, leading to unexpected resonance frequency behavior, such as increasing for increased applied voltage in this situation. For future sample sets, thicker cantilevers will be used to provide more uniform cantilever actuation.

4.4.2.3 Capacitor Layout C.

The next variant of the 3 GHz structure to be examined with stripline measurements calibrated using the 12-term error correction model and time domain gating has two sets of cantilevers on each side of the cell between the inner and outer split rings, providing additional intra-ring capacitance, as modeled in Section 3.3.6. This sample is also 4 unit cells long.

The stripline measurements were taken at 0 volts, 5 volts, and every two volts from 10 volts to 30 volts. The measured transmission data is shown in Figure 111(a). Transmission data magnified around the 2 and 3 GHz transmission nulls are shown in Figures 111(b) and 111(c) respectively. With increased voltage, the transmission nulls are seen to shift slightly, only 0.052 GHz and 0.050 GHz for the 2 and 3 GHz resonance regions respectively.

4.4.2.4 Capacitor Layout E.

The next variant of the 3 GHz structure to be examined with stripline measurements calibrated using the 12-term error correction model and time domain gating has three sets of cantilevers on each side of the cell between the inner and outer split rings, providing additional intra-ring capacitance, as modeled in Section 3.3.6. The sample is 4 cells in length.

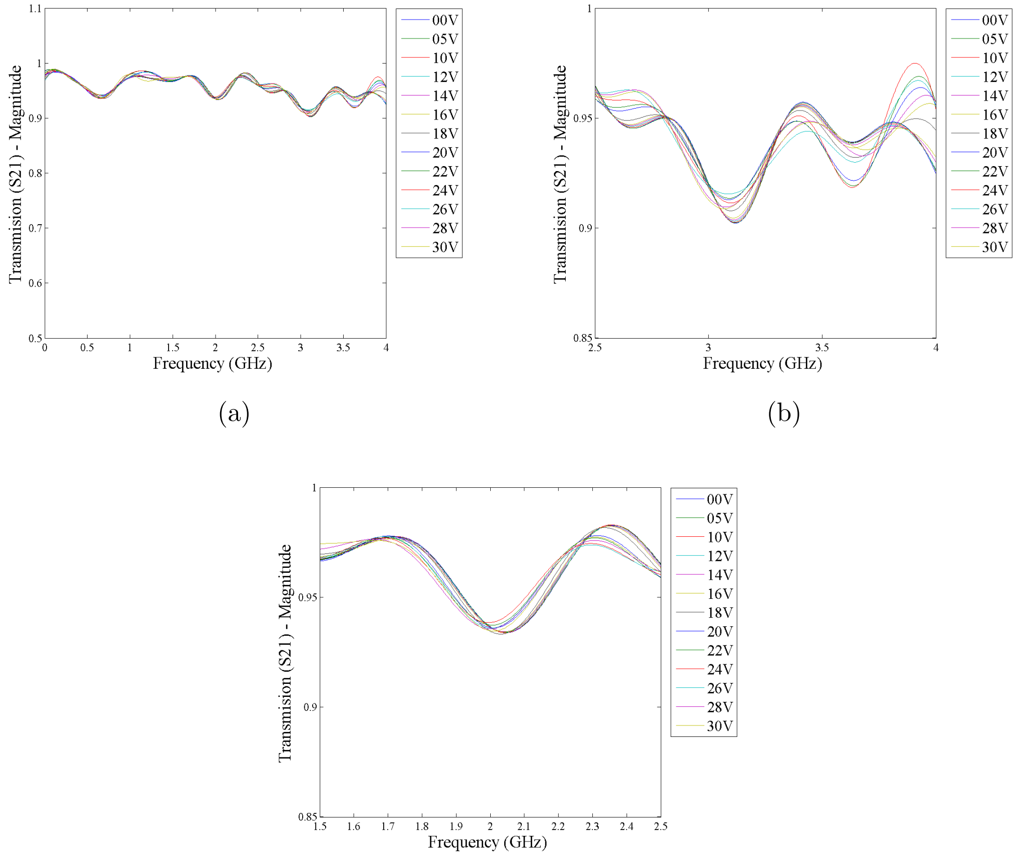

(a)

(b)

(c)

Figure 111. (a) Measured transmission calibrated including time domain gating from larger AFIT metamaterial sample with capacitor Layout C(two intra-ring capacitors) over the entire frequency range measured. Measured transmission magnified around (b) 2 GHz and (c) 3 GHz transmission nulls. The transmission nulls are seen to shift slightly with increased voltage.

The stripline measurements were taken at 0 volts and at every volt from 5 to 15 volts. The measured transmission data from the 3 GHz sample with capacitor layout E is shown in Figure 112. Transmission nulls are seen around 1 and 2 GHz, however there is no shifting seen as voltage is increased.

4.4.3 Capacitance Test Structure Measurements.

For the larger adaptive metamaterial structures, capacitance test structures were created to measure and quantify the additional capacitance provided by the cantilever

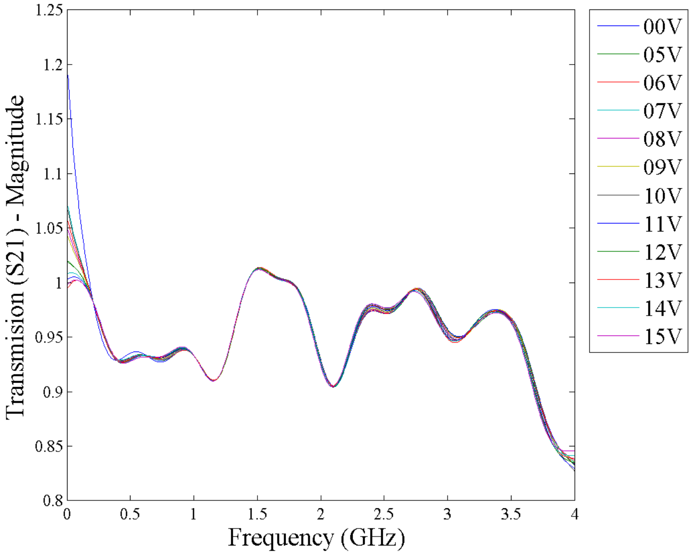

Figure 112. Measured transmission calibrated including time domain gating from a larger AFIT metamaterial sample with capacitor layout E. While transmission nulls are observed around 1 and 2 GHz, changes are seen with increased applied voltage.

structures. The structures allowed for capacitance values to be extracted from S-parameter measurements of the structure using [2]

$$Z_{Total} = Z_o \frac{1 + S_{11}}{1 - S_{11}} \tag{32}$$

where Z_o is the reference impedance, to determine the total impedance of the structure (Z_{Total}). From the impedance, the total capacitance (C_{Total}) can be computed using

$$C_{Total} = \frac{-1}{2\pi f \Im\{Z_{Total}\}}. \tag{33}$$

The measurement system was calibrated using the short open load through (SOLT) method discussed in [37] using a CS-5 calibration substrate. Due to ambiguity in the time domain response of the cantilever test structure, time domain gating was not performed on the S-parameter measurements. The ambiguity comes from the size of the test structures and time domain resolution of the NWA. Calibration of the system places the calibration plane at the RF probe tips, not a the test device. S-parameters are measured for an electrical short test structure for the cantilever test structures, allowing the calibration plane to be moved to the appropriate location in post processing.

Measurements were taken with different voltages applied to the test structure. The voltages were taken from 0 to 30 volts in increments of 5 volts. The frequency range is restricted to the operating range of the stripline, 0 to 4 GHz. Two samples of the cantilever test structure with five cantilevers are examined. The extracted capacitance values for the first sample are shown in Figure 113(a). The signal is clearly noisy below 1.5 GHz. Between 1.5 GHz and 4 GHz, the capacitance data is as expected, a fairly constant value, except for a peak around 3.2 GHz. Changes are seen as the applied voltage is increased. At 0 volts applied, the capacitance is about 2 pF. When the voltage is increased to 5 volts, the capacitance is about 1 pF a decrease from the 0 volt case. This shows that there is at least one cantilever starting in the down position that becomes bent as the voltage is initially increased. From 5 to 15 volts, the capacitance increases to through 1.5 pF at 10 volts back to 2 pF at 15 volts, showing a second cantilever pulling into the down position. For 20 to 30 volts, the capacitance reaches the maximum value of about 4 pF.

The extracted capacitance values for the second samples are shown in Figure 113(b). Again, the measurement is noisy below 1.5 GHz. Above 1.5 GHz, the data is smooth, however there is no appreciable changes in capacitance with applied voltage increases. The capacitance remains between 4 and 6 pF for most of the frequency range between 1.5 and 4 GHz except around 3.2 GHz where the capacitance peaks

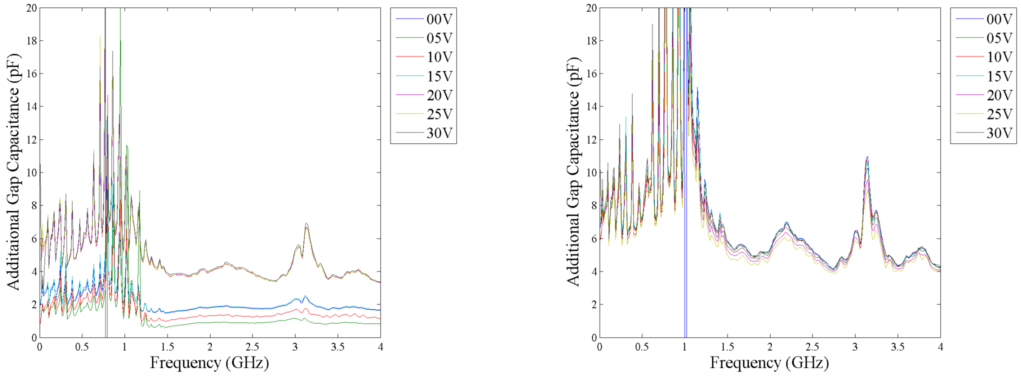

(a)

(b)

Figure 113. Measured additional gap capacitance provided by cantilever structures. (a) The first sample shows changes with increased voltage applied that match cantilever physics, while (b) the second sample does not show discernible changes.

around 11 pF. Without consistent measurements of the additional gap capacitance provided by the cantilever test structures, recommendations cannot be made to improve simulation validity. The additional capacitance values found empirically using CST MWS® remain the best estimates for the additional gap capacitance values. Altered cantilever test devices are recommended.

4.4.4 Larger AFIT Metamaterial Design Stripline Measurements Conclusions.

Four different capacitor layouts of the larger AFIT metamaterial design are examined with stripline measurements. Samples with capacitor layout A show the most promise for shifting the resonance frequency. A maximum shift of 5.5% from the resonance frequency without voltage applied is observed. This resonance shift corresponds to simulated average effective capacitance values of 0.85 pF and 1.5 pF for the 0 and 25 volts applied cases respectively. These additional gap capacitance values are obtained empirically with CST MWS® because cantilever test structures do not produce repeatable measurements as designed. Improvements to the cantilever test structures are recommended. There is minimal resonance shift observed for the other three capacitor layouts measured.

Fabrication issues present in the smaller devices were eliminated, allowing the devices to be oriented properly in the waveguide. All sets of cantilevers are also operable. Despite clearing these fabrication hurdles, issues with cantilever thickness leads to non-uniform cantilever actuation. The non-uniform actuation leads to smaller resonance frequency shifts and less intense resonance behavior. Samples with thicker cantilevers would lead to higher pull down voltages of the cantilevers with a more finite set of cantilever states. The simulated capacitance values shown in Table 9 are also recommended for a linear decrease in resonance frequency.

4.5 Measurement Summary

The stripline measurement results presented for the smaller AFIT designed metamaterial devices provide a far field basis for the prediction aided measurement (PAM) field examination presented in Chapter III. The physical devices show frequency adaptability of greater than 10% of the initial resonance frequency for both of the smaller structures analyzed. Measurement results of the four capacitor layouts of the larger AFIT designed metamaterial structures show the most promising frequency adaptability from the capacitor layout with additional gap capacitance only. A maximum shift of 5.5% from the initial resonance frequency is seen for this structure while minimal shift is seen with the other three layouts. Repeatability of the stripline measurements is discussed in Section 4.3.2. The measurements of a single structure are repeatable if the voltage applied to to the device is kept within the operating range of the device. However, measurement repeatability for a single sample can degrade as the number of cantilever actuation cycles increases due to increased wear on the mechanical components of the cantilever structures. Measurements are not repeatable from device to device as all sets of cantilevers are not initially in the same position, i.e. some are in the up position while some are in the down. This leads to non-uniform cantilever actuation from sample to sample, leading to different dispersive resonance regions and resonance depth for different samples. Despite these complications, the simulation tool proves effective at modeling the physical devices in both the far and near field.

V. Conclusions and Recommendations

5.1 Smaller Scale AFIT Adaptive Metamaterial Research Summary

Full wave electromagnetic simulations are combined with stripline measurements of metamaterial samples in this thesis to characterize electromagnetic field behavior in the presence of these devices. A basic single cell model of the smaller scale AFIT adaptive metamaterial is refined to a model representative of stripline measurements. The final model is a 17-cell column modeled as fabricated: with additional cuts to allow the cantilevers to actuate, rotated off of the ideal orientation, with cantilever control traces included and with metal particles modeled as gold instead of PEC. The far field data from the simulated structures, the S-parameters, match reasonably well with measured data while balancing computational requirements.

The lumped element capacitor values are optimized to determine the average effective capacitance values required for simulated devices to respond as the physically measured samples. For the 17-Cell structure with cuts across the inner cantilever control traces, the optimization procedure produced an average effective capacitance value of 0.195456 pF for the inner capacitors at all voltage levels and average effect capacitance values for the outer capacitors of 0.195456 pF and 1.5 pF for the 0 volts and 28 volts applied cases respectively. The measured resonance frequency shifts 618 MHz or a 12.5% difference from the original resonance frequency. For the 17-Cell structure with cuts across the outer split ring, the optimization procedure produced an average effective capacitance value of 0.1375 pF for the outer capacitors at all voltage levels and average effective capacitance values for the inner capacitors of 0.2125 pF and 3.3125 pF for the 0 volts and 60 volts applied cases respectively. The measured resonance frequency changes 1.62 GHz or an 11.34% difference from the original resonance frequency. The simulations predict and the measurements verify that the resonant frequency can be influenced by the AFIT MEMS capacitor design.

The combination of measurements with full wave electromagnetic solutions allow the field behavior within the computational domain to be examined. Field investigations into 4-cell structures show different resonance modes at different resonance regions. The inclusion of the cantilever control traces and lossy metal in the model lead to decreased resonance behavior in the transmission null regions. The resonance modes seen in the 4-cell PEC models are not seen strongly in the models that take most of the physics of the sample into account. The transmission loss appears to come from scattering from the sample within the resonance regions. Outside the resonance regions, there is little scattering by the structure, while inside the resonance areas, the fields do not maintain their strength, scattering from the structure. Additionally, there is a distinct roll off of the transmission at higher frequencies caused by more scattering as the wavelength decreases. Despite the size of the metallic inclusions and separation distances compared to the wavelength of incident energy meeting size requirements, there is still non-negligible scattering, and therefore transmission loss at the higher frequencies.

As modeled and measured, the interactions within a single column of the structures do not create enough scattering to produce the desired effects. Enhanced effects would be seen if multiple columns are used as samples, however fabrication difficulties lead to limited sample availability.

Overall, this research effort shows that using full-wave electromagnetic solvers to model metamaterials including as much of the physics of the device as possible provides the most accurate solution when compared with measurements. Because models that include more of the physics of the devices are more complex, there is a limit on the number of parameters that can be optimized to match measured results. The capacitance values that are obtained empirically from the optimizations are average effective capacitance values for the sets of inner and outer cantilevers and do not take into account the cell to cell non-uniformity of the cantilever sets. This limit on the optimization can be eased as the required computation time decreases.

5.2 Larger Scale AFIT Adaptive Metamaterial Research Summary

Full wave electromagnetic simulations and measurements of larger scale AFIT metamaterials are also combined in this thesis to determine the most promising structure for changing the resonance frequency. For the four capacitor layout variants created, a single cell model is refined to represent the structures as measured, 4-cell long columns in a stripline. The single resonance frequency provided by capacitor layout A provides transmission results that are most easily evaluated for resonance frequency shifts. To achieve a resonance frequency shift from 2.3 GHz to 1.0 GHz, a change of additional gap capacitance of 0.1 pF to 1.5 pF needs to occur. To achieve a linear step decrease in the resonance frequency, thicker cantilever beams with geometries that will provide the additional capacitance values in Table 9 are recommended. The thicker beams would provide a more discrete change in additional capacitance and therefore a more discrete change in resonance frequency.

The remaining layouts are not recommended for further design improvements. As the number non-uniformly actuating capacitors is increased, the strength of resonant mode coupling as decreased, as seen in measurements of the samples . Stronger resonance regions would be achieved if the MEMS structures actuated uniformly across the cells.

5.3 Recommendations for Future Research

The proposals for expansion of this research involve design improvements to the current adaptive metamaterial models and the suggestion of an alternate measurement system.

5.3.1 2D-Focus Beam Measurement System Recommendations.

An alternate method for making transmission and reflection measurements involving a two dimensional RF focusing system is proposed for fabrication and evaluation. The proposed system would allow for examining responses for fields of off-normal incidence. The proposed system would fit inside the current AFIT BANTAM range. Initial simulations presented in this thesis show that the required TEM mode can be stimulated inside the measurement system, as well as an area of constant amplitude and phase generated at the focal plane of the system. The proposed system would have interchangeable lenses of varying heights depending on the frequency range to be examined for a particular sample. The system will allow another option for bulk metamaterial samples to be measure. The smaller top plate of the structure also allows for a field probe to be used to measure field values in the near-field of the metamaterial structure. The BANTAM structure allows for two dimensional scanning to take place. The models of the 2D-Focus Beam system should also be refined to include the field probe in simulations.

5.3.2 Adaptive Metamaterial Recommendations.

Stripline measurements of the adaptive metamaterial structures confirm the validity of the modeling approach used in this thesis. As shown in this thesis, the capacitance values of the larger AFIT metamaterial structure with capacitor layout A should be adjusted to match capacitor values in Table 9.

Capacitance measurements should also be made of the MEMS cantilever structures at higher frequencies. The current cantilever test structures intended for this use are not long enough for time domain gating to be applied accurately using the

NWA. The length of the transmission line from the high-frequency probe pads to the cantilever structure should be extended such that the test structure length runs across the entire wafer used in fabrication. Measurements should be performed over the operating range of the system in which the samples will be measured in.

Investigation should also take place into adjusting the inductance of the unit cell. Changes in inductance would have the same effect as changes in capacitances. The outer split ring could include additional lengths of metal that run out from the sides of the cell, while keeping the general split ring structure mostly intact. The additional traces would not add additional breaks in the outer split ring, but provide additional wire length.

For the metamaterial structures including MEMS devices to be useful, the reliability of the devices needs to be improved. The fabrication process does not produce cantilever beams that are in uniform initial positions, leading to non-uniform beam actuation across the cells in a sample. Also, the devices continued to short out throughout testing, therefore not allowing for repeat measurements. Improvements to the actuation mechanism need be made to ensure that once a beam is pulled down, it does not pull through the dielectric, causing a short.

Additionally, the models created to match the measured transmission data were created with fore knowledge of the physical structure creating the responses. Methods should be investigated to solve the problem in reverse and determine structures that can create the measured far field data.

Appendix A. Simulation Statistics

Solve times and mesh statistics for various models are presented.

Table 13. **Solution time for smaller AFIT metamaterial models**

Model	Time[1]		
	Hours	Minutes	Seconds
Smaller AFIT metamaterial unit cell	0	8	54
Smaller AFIT metamaterial single cell	0	9	42
Empty 18 GHz waveguide	0	35	40
Smaller AFIT metamaterial 4-cell column in waveguide, cuts across control traces	1	15	36
Smaller AFIT metamaterial 4-cell column in waveguide, cuts across outer SRR	1	4	36
Smaller AFIT metamaterial 17-cell column in waveguide, cuts across control traces	16	15	54
Smaller AFIT metamaterial 17-cell column in waveguide, cuts across outer SRR	16	35	45
Smaller AFIT metamaterial 17-cell column in waveguide, cuts across control traces with thinner control traces	53	28	12
Smaller AFIT metamaterial 17-cell column in waveguide, cuts across outer SRR with thinner control traces	69	54	12
Smaller AFIT metamaterial 17-cell column in waveguide (gold), cuts across control traces with thinner control traces	16	52	42
Smaller AFIT metamaterial 17-cell column in waveguide (gold), cuts across outer SRR with thinner control traces	18	12	48

[1] Total includes simulations at the six different calculated capacitor values except for empty waveguide where only one simulation is needed.

Table 14. Smaller AFIT metamaterial design frequency-solver mesh statistics

Model	Tetrahedrons	Edge Length (mm)		Quality		
		Min	Max	Min	Max	Average
AFIT metamaterial unit cell[1]	1,596	0.040	1.50329	0.0339014	0.991026	0.652214
AFIT metamaterial single cell[1]	2,972	0.026892	1.37655	0.002616	0.993009	0.675283
Empty 18 GHz waveguide	71,604	0.45	4.85705	0.209568	0.99823	0.805127
AFIT metamaterial 4-cell column in waveguide, cuts across control traces[1]	35,565	0.0045779	4.57426	0.00284107	0.998401	0.604527
AFIT metamaterial 4-cell column in waveguide, cuts across outer SRR[1]	30,473	0.00157541	4.57426	0.000368086	0.997779	0.610912
AFIT metamaterial 17-cell column in waveguide, cuts across control traces[1]	119,624	0.00826101	4.57984	0.00255643	0.997775	0.605737
AFIT metamaterial 17-cell column in waveguide, cuts across outer SRR[1]	120,873	0.0083954	4.57885	0.00456643	0.9967835	0.615467
AFIT metamaterial 17-cell column in waveguide, cuts across control traces with thinner control traces[1]	136,329	0.00294037	4.57779	0.000285457	0.99717	0.590036
AFIT metamaterial 17-cell column in waveguide (gold), cuts across control traces with thinner control traces [1]	61,875	0.00249857	4.57874	0.000126682	0.998532	0.640505
AFIT metamaterial 17-cell column in waveguide (gold), cuts across outer SRR with thinner control traces [1]	62,560	0.00152854	4.57117	0.00017286	0.997127	0.652625

[1] Statistics are for C5 lumped element capacitance. Other lumped capacitance values produce similar meshes.

Table 15. Solution time for larger AFIT metamaterial models

Model		Time[1]		
		Hours	Minutes	Seconds
Layout A	Unit Cell	0	17	18
	Single Cell	0	0	34
	4-cell Column in Waveguide	10	59	42
Layout B	Unit Cell	0	19	30
	Single Cell	0	16	06
	4-cell Column in Waveguide[2]	-	-	-
Layout C	Unit Cell	0	20	48
	Single Cell	0	7	54
	4-cell Column in Waveguide	0	51	36
Layout D	Unit Cell	0	25	06
	Single Cell	0	15	00
	4-cell Column in Waveguide	1	12	00
Layout E	Unit Cell	0	29	48
	Single Cell	0	9	18
	4-cell Column in Waveguide	0	55	24
Empty 4 GHz stripline		0	3	42

[1] Total includes simulations at the six different calculated capacitor values except for empty waveguide where only one simulation is needed.

[2] Not completed

Table 16. Largre AFIT metamaterial design frequency-solver mesh statistics

Model		Tetrahedrons	Edge Length (mm)		Quality		
			Min	Max	Min	Max	Average
Layout A[1]	Unit Cell	21,923	0.0220511	2.74315	0.0271006	0.996466	0.623932
	Single Cell	9,109	0.0721185	2.6131	0.0149845	0.99804	0.708445
	4-cell Column in Waveguide	148,304	0.0192538	8.23723	0.0134536	0.99577	0.675801
Layout B[1]	Unit Cell	22,823	0.0172879	2.74315	0.0223806	0.996466	0.620918
	Single Cell	24,872	0.0186468	2.74408	0.00791466	0.99804	0.621694
	4-cell Column in Waveguide[2]	-	-	-	-	-	-
Layout C[1]	Unit Cell	22,810	0.0231353	2.74315	0.00591502	0.996562	0.62609
	Single Cell	11,834	0.0317194	2.52888	0.0122487	0.99804	0.664849
	4-cell Column in Waveguide	43,268	0.0101879	16.2081	0.00168306	0.998366	0.578413
Layout D[1]	Unit Cell	22,294	0.0208572	2.74315	0.0154051	0.997526	0.616907
	Single Cell	12,924	0.0326011	2.79146	0.020467	0.99804	0.65805
	4-cell Column in Waveguide	40,014	0.0130969	16.2666	0.00125046	0.998366	0.570199
Layout E[1]	Unit Cell	22,612	0.0237758	2.74315	0.010358	0.996466	0.622168
	Single Cell	12,845	0.0375653	2.79146	0.0204859	0.99804	0.656495
	4-cell Column in Waveguide	42,446	0.014346	16.4434	0.000427209	0.998366	0.582235
Empty 4 GHz stripline		71,651	0.30509	8.24132	0.0758678	0.998214	0.771708

[1] Statistics are for C5 lumped element capacitance. Other lumped capacitance values produce similar meshes.

[2] Not completed

Table 17. 2D Focus Beam System model mesh summary

Model	Mesh Step		Number Mesh Lines			Time			Number of Mesh Cells
	Min	Max	x-axis	y-axis	z-axis	Hours	Minutes	Seconds	
2D Focus Beam System, 1 inch lenses	0.0131733	0.111389	615	38	918	5	17	48	20,832,406
2D Focus Beam System, 2 inch lenses	0.0131733	0.111389	615	53	918	7	50	13	29,277,976

Bibliography

[1] "The Simulation Method". CST Microwave Studio® help file, 2010.

[2] Balanis, Constantine A. *Advanced Engineering Electromagnetics*. Wiley, New York, 1989.

[3] Bérenger, J. P. "Perfectly matched layer for the FDTD solution of wave-structure interaction problems". *IEEE Trans.Antennas Propag.*, 44(1):110–117, 1996.

[4] Chen, L. F. *Microwave Electronics : Measurement and Materials Characterisation*. Wiley, 2004. ISBN 0470844922.

[5] Chen, Xudong, Tomasz M. Grzegorczyk, Bae-Ian Wu, Joe Pacheco, and Jin Au Kong. "Robust method to retrieve the constitutive effective parameters of metamaterials". *Phys.Rev.E: Stat.Nonlinear Soft Matter Phys.*, 70(1):016608, July 2004.

[6] Clemens, M., E. Gjonaj, P. Pinder, and T. Weiland. "Numerical Simulation of Coupled Transient Thermal and Electromagnetic Fields with the Finite Integration Method". *IEEE Trans.Magn.*, 36(4):1448, Jul. 2000.

[7] Engheta, N. and Richard W. Ziolkowski. *Metamaterials: Physics and Engineering Explorations*. Wiley, Hoboken, N.J., 2006.

[8] Garcia, N. and M. Nieto-Vesperinas. "Is there an experimental verification of a negative index of refraction yet?" *Opt.Lett.*, 27(11):885–887, 2002.

[9] Gil, I., J. García-García, J. Bonache, F. Martín, M. Sorolla, and R. Marqués. "Varactor-loaded split ring resonators for tunable notch filters at microwave frequencies". *Electron.Lett.*, 40(21):1–2, Oct. 2004.

[10] Gollub, Jonah N., David R. Smith, and Juan D. Baena. "Hybrid resonant phenomenon in a metamaterial structure with integrated resonant magnetic material". *Opt.Express*, 17(4):2122–2131, 2008.

[11] Hambling, David. "Metamaterial miracles". *Popular Mechanics*, 186(9):18–18, Sept. 2009.

[12] Han, Jiaguang, Akhlesh Lakhtakia, and Cheng-Wei Qiu. "Terahertz metamaterials with semiconductor split-ring resonators for magnetostatic tunability". *Opt.Express*, 16(19):14390–14396, 2008.

[13] Hand, T. and S. Cummer. "Characterization of tunable metamaterial elements using MEMS switches". *IEEE Antennas Wireless Propag.Lett.*, 6:401–404, Jan. 2007.

[14] Hayt, William Hart and Jack E. Kemmerly. *Engineering Circuit Analysis.* McGraw-Hill, New York, 1993.

[15] Hecht, Eugene. *Optics.* Addison-Wesley, Reading, Mass., 2002.

[16] Hirtenfelder, F. and G. Lubkowski. "3D field simulations using FI time domain technique of wedge- and parabolic-shaped left handed materials (LHM)". *2007 3rd International Workshop on Antenna Technology: Small and Smart Antennas MetaMaterials and Applications.* IEEE, Jan. 2007. (IEEE Cat No. 07EX1729).

[17] Huang, Da, Ekaterina Poutrina, and David R. Smith. "Analysis of the power dependent tuning of a varactor-loaded metamaterial at microwave frequencies". *Applied Physics Letters*, 96(10):104104–104104–3, 2010. ID: 1.

[18] Knott, Eugene F., John F. Shaeffer, and Michael T. Tuley. *Radar Cross Section.* Artech House, Boston, 1993.

[19] Langely, D. "MEMS integrated metamaterial structure having variable resonance for RF applications". *Proceedings of the SEM Annual Conference.* 2010.

[20] Lapine, M. and S. Tretyakov. "Contemporary notes on metamaterials". *IET Microwaves Antennas Propag.*, 1(1):3–11, Feb. 2007.

[21] Leonhardt, Ulf. "Optical conformal mapping". *Science*, 312(5781):1777–1780, June 2006.

[22] Lui, Chang. *Foundation of MEMS.* Pearson Prentice Hall, Upper Saddle River, New Jersey: Pearson Prentice Hall, 2006.

[23] Lundell, Christopher A. *Characterization and measurement of passive and active metamaterial devices.* 2010.

[24] Lunet, G., V. Vigneras, H. Kassem, and L. Oyhenart. "Meta-material with tunable thin film material for the conception of active radome". *Microwave Conference, 2009. EuMC 2009. European*, 602–605. 2009. ID: 1.

[25] Munk, Ben A. *Frequency Selective Surfaces: Theory and Design.* John Wiley, New York, 2000.

[26] Munk, Ben A. *Metamaterials: Critique and Alternatives.* John Wiley, Hoboken, N.J., 2009.

[27] Munk, Ben A., Dan S. Janning, Jonothan B. Pryor, and Ronald J. Marhefka. "Scattering from surface waves on finite FSS". *IEEE Trans.Antennas Propag.*, 49(12):1782–1793, 2001.

[28] Nicholson, K. J. and K. Ghorbani. "Design, manufacture and measurement of a metamaterial with tunable negative-refractive index region". *Microwave Conference, 2009. APMC 2009. Asia Pacific*, 1231–1233. 2009. ID: 1.

[29] Pendry, J. B., A. J. Holden, D. J. Robbins, and W. J. Stewart. "Magnetism from conductors and enhanced nonlinear phenomena". *IEEE Trans.Microw.Theory Tech.*, 47(11):2075–2084, Nov. 1999.

[30] Pendry, J. B., A. J. Holden, W. J. Stewart, and I. Youngs. "Extremely low frequency plasmons in metallic mesostructures". *Phys.Rev.Lett.*, 76(25):4773–4776, June 1996.

[31] Pendry, J. B., D. Schurig, and D. R. Smith. "Controlling electromagnetic fields". *Science*, 312(5781):1780–1781, June 2006.

[32] Pozar, David M. *Microwave Engineering*. Addison-Wesley, Reading, Mass., 1990.

[33] Ran, L., J. Huangfu, H. Chen, X. Zhang, K. Cheng, T. M. Grzegorczyk, and J. A. Kong. "Experimental study on several left-handed metamaterials". *Progress in Electromagnetics Research*, PIER 51:249–279, 2005.

[34] Rederus, Luke. "A MEMS Multi-Cantilever Variable Capacitor on Metamaterial", 2009. (ADA497157).

[35] Sanz, M., A. C. Papageorgopoulos, W. F. Egelhoff, M. Nieto-Vesperinas, and N. García. "Transmission measurements in wedge-shaped absorbing samples: an experiment for observing negative refraction". *Phys.Rev.E: Stat.Nonlinear Soft Matter Phys.*, 67(6):067601, June 2003.

[36] Schuhmann, R. and T. Weiland. "Efficient calculation of effective material parameters in metamaterials using FDTD and a modal approach". *Microwave Symposium Digest, 2002 IEEE MTT-S International*, volume 3, 2037–2040. 2002.

[37] Scott, A and R Frobenius. *RF Measurements for Cellular Phones and Wireless Data Systems*. Wiley-IEEE Press, 2008.

[38] Shadrivov, Ilya V., Alexander B. Kozyrev, Daniel W. van der Weide, and Yuri S. Kivshar. "Tunable transmission and harmonic generation in nonlinear metamaterials". *Appl.Phys.Lett.*, 93:161903, 2008.

[39] Shadrivov, Ilya V., Steven K. Morrison, and Yuri S. Kivshar. "Tunable split-ring resonators for nonlinear negative-index metamaterials". *Opt.Express*, 14:9344, 2006.

[40] Shelby, R. A., D. R. Smith, and S. Schultz. "Experimental Verification of a Negative Index of Refraction". *Science*, 292(5514):77, Apr. 2001.

[41] Simovski, Constantin R., Pavel A. Belov, and Sailing He. "Backward wave region and negative material parameters of a structure formed by lattices of wires and split-ring resonators". *IEEE Trans.Antennas Propag.*, 51(10):2582–2591, 2003.

[42] Smith, D. R., W. J. Padilla, D. C. Vier, S. Nemat-Nasser, and S. Schultz. "Composite medium with simultaneously negative permeability and permittivity". *Phys.Rev.Lett.*, 84(18):4184–4187, May 2000.

[43] Smith, D. R., D. C. Vier, Th Koschny, and C. M. Soukoulis. "Electromagnetic parameter retrieval from inhomogeneous metamaterials". *Phys.Rev.E: Stat.Nonlinear Soft Matter Phys.*, 71(3):036617/1–036617/11, 2005.

[44] Sui, Qiang and Fang Li. "Experimental study of composite medium with simultaneously negative permeability and permittivity". *Sci.China, Ser.G*, 47(1):64–78, 2004.

[45] Tretyakov, Sergei. "On geometrical scaling of split-ring and double-bar resonators at optical frequencies". *Metamaterials*, 1(1):40–43, Mar. 2007.

[46] Veselago, V. G. "The electrodynamics of substances with simultaneously negative values of ϵ and μ". *Phys.Usp.*, 10(4):509–514, Jan. 1968.

[47] Veselago, V. G. "Electrodynamics of materials with negative index of refraction". *Phys.Usp.*, 46(7):764–768, July 2003.

[48] Ward, A. J. and J. B. Pendry. "Refraction and geometry in Maxwell's Equations". *J. Mod. Opt.*, 43(4):773–793, 1996.

[49] Weiland, T., R. Schuhmann, R. B. Greegor, C. G. Parazzoli, A. M. Vetter, D. R. Smith, D. C. Vier, and S. Schultz. "Ab initio numerical simulation of left-handed metamaterials: comparison of calculations and experiments". *J.Appl.Phys.*, 90(10):5419–5419, 2001.

[50] Weiland, T., M. Timm, and I. Munteanu. "A practical guide to 3-D simulation". *IEEE Microwave Mag.*, 9(6):62–75, Dec. 2008.

REPORT DOCUMENTATION PAGE	*Form Approved* *OMB No. 0704–0188*

1. REPORT DATE *(DD–MM–YYYY)* 24–03–2011	**2. REPORT TYPE** Master's Thesis	**3. DATES COVERED** *(From — To)* Aug 2009 — Mar 2011

4. TITLE AND SUBTITLE Electromagnetic Modeling and Measurement of Adaptive Metamaterial Structural Elements	**5a. CONTRACT NUMBER** **5b. GRANT NUMBER** **5c. PROGRAM ELEMENT NUMBER**
6. AUTHOR(S) Jussaume, Matthew E., Capt, USAF	**5d. PROJECT NUMBER** ENG 10-142 **5e. TASK NUMBER** **5f. WORK UNIT NUMBER**

7. PERFORMING ORGANIZATION NAME(S) AND ADDRESS(ES) Air Force Institute of Technology Graduate School of Engineering and Management (AFIT/EN) 2950 Hobson Way Wright-Patterson AFB, OH 45433-7765	**8. PERFORMING ORGANIZATION REPORT NUMBER** AFIT/GE/ENG/11-20
9. SPONSORING / MONITORING AGENCY NAME(S) AND ADDRESS(ES) Air Force Research Lab, Materials and Manufacturing Directorate Attn: Katie Thorp 2941 Hobson Way Wright-Patterson AFB, OH 45433-7750 (937) 255-9145, katie.thorp@wpafb.af.mil	**10. SPONSOR/MONITOR'S ACRONYM(S)** AFRL/RX **11. SPONSOR/MONITOR'S REPORT NUMBER(S)**

12. DISTRIBUTION / AVAILABILITY STATEMENT

APPROVED FOR PUBLIC RELEASE; DISTRIBUTION UNLIMITED. This material is declared a work of the U.S. Government and is not subject to copyright protection in the United States.

13. SUPPLEMENTARY NOTES

14. ABSTRACT

This document addresses two major obstacles facing metamaterial development: uncertainty in the characterization of electromagnetic field behavior in metamaterial structures and the relatively small operational bandwidth of metamaterial structures. To address the first obstacle, a method of prediction aided measurement is developed and exploited to examine the field interactions within metamaterial devices. The fusion of simulation and measurement techniques enhances the understanding of the physical interactions of fields in the presence of metamaterials. To address the second obstacle, this document characterizes the effectiveness of an adaptive metamaterial design that incorporates a microelectromechanical systems (MEMS) variable capacitor. Applying voltages to the MEMS device changes the resonant frequency of the metamaterial. In this research, various capacitor layouts are examined with computational models and stripline measurements, leading to recommendations for design improvements.

15. SUBJECT TERMS

Metamaterials, Prediction Aided Measurement, Computational Electromagnetics, MEMS Devices, Frequency Adaptive Metamaterials, Stripline Measurements

16. SECURITY CLASSIFICATION OF:			**17. LIMITATION OF ABSTRACT**	**18. NUMBER OF PAGES**	**19a. NAME OF RESPONSIBLE PERSON**
a. REPORT	**b. ABSTRACT**	**c. THIS PAGE**			Dr. Peter J. Collins, ENG
U	U	U	UU	202	**19b. TELEPHONE NUMBER** *(include area code)* (937) 255-3636, x7256; peter.collins@afit.edu